

POLITECNICO DI MILANO  
FACOLTÀ DI INGEGNERIA INDUSTRIALE E DELL'INFORMAZIONE  
**CORSO DI LAUREA IN NUCLEAR ENGINEERING**



**POLITECNICO**  
MILANO 1863

**GILARDONI SPA X-RAY BAGGAGE  
SCANNING SYSTEM:  
REVIEW, MCNP MODELLING AND  
IMPROVEMENT PROPOSAL**

Relatore: Prof. Marco Caresana

Correlatori: Dott. Gabriele Zorloni  
Ing. Ludovico Aiello

Tesi di Laurea di:

**ANDREA ROCCHI**

Matr. 900071

Anno Accademico 2018/2019



*To my mom, for your love and unconditional support*





**POLITECNICO**  
**MILANO 1863**



*This thesis work was carried out during the internship at  
Gilardoni Spa in September 2019 - March 2020*



# Contents

<b>List of Figures</b> .....	<b>xi</b>
<b>List of Tables</b> .....	<b>xiii</b>
<b>Acknowledgements</b> .....	<b>xv</b>
<b>Abstract (English)</b> .....	<b>xvii</b>
<b>Abstract (Italiano)</b> .....	<b>xix</b>
<b>Estratto</b> .....	<b>xxi</b>
<b>Bibliografia</b> .....	<b>xxxii</b>
<b>1 Context analysis</b> .....	<b>1</b>
1.1 Baggage check .....	1
1.2 X-Ray radiographic principles .....	4
1.3 Gilardoni X-Ray industry .....	7
<b>2 X-Ray scanning systems</b> .....	<b>9</b>
2.1 X-Ray source .....	9
2.1.1 X-Ray tube: photon generation principle.....	9
2.1.2 Energy spectrum generated by the X-Ray tube .....	10
2.1.3 Structure of an X-Ray tube .....	12
2.1.4 AION monoblock: Gilardoni's X-Ray generator .....	13
2.2 X-Ray scanning system detector.....	14
2.2.1 General working principle .....	15
2.2.2 Scintillators .....	17
2.2.3 Photodiode .....	19
2.2.4 Detector efficiency optimization.....	20
2.3 Image acquisition system.....	21
2.3.1 Single energy systems and double energy systems.....	22
<b>3 Scintillators review</b> .....	<b>27</b>
3.1 Historical development .....	27
3.2 Scintillators production.....	28

---

3.2.1	Activator species .....	29
3.3	Scintillator properties .....	31
3.3.1	Light yield .....	31
3.3.2	Transparency and light transport.....	32
3.3.3	X-Ray stopping power .....	32
3.3.4	Primary decay time and afterglow .....	33
3.3.5	Chemical stability and radiation hardness.....	35
3.3.6	Other properties.....	36
3.4	Scintillators: market and research .....	37
3.4.1	CsI(Tl) .....	38
3.4.2	NaI(Tl).....	39
3.4.3	CdWO <sub>4</sub> .....	39
3.4.4	BGO .....	40
3.4.5	PbWO <sub>4</sub> .....	40
3.4.6	Rare-earth oxyorthosilicates LSO-LYSO-GSO .....	40
3.4.7	Aluminium perovskite compounds YAP-LuAP-LuYAP.....	41
3.4.8	Lanthanum halides LaCl <sub>3</sub> -LaBr <sub>3</sub> .....	42
3.4.9	Garnet scintillators YAG-LuAG-GYAG-GAGG .....	42
3.4.10	Ceramic scintillators GOS.....	43
3.4.11	New Eu-doped rare-earth iodides scintillators .....	44
3.5	Candidate scintillator .....	44
<b>4</b>	<b>Efficiency evaluation.....</b>	<b>49</b>
4.1	Monte Carlo models .....	50
4.1.1	Monte Carlo methods .....	51
4.1.2	MCNP photon source modelling.....	54
4.1.3	Simulated data validation .....	57
4.1.4	Energy deposition evaluation code: MCNP tally f8.....	65
4.2	MATLAB code for matching evaluation .....	67
4.2.1	GrabIt tool: from graphic to raw data.....	67
4.2.2	MATLAB matching code.....	68
4.3	CsI(Tl), GAGG(Ce) comparison result.....	69
<b>5</b>	<b>Conclusion.....</b>	<b>71</b>

<b>1</b>	<b>Appendix.....</b>	<b>73</b>
	<i>Gilardoni Spa dual energy system .....</i>	<i>73</i>
<b>2</b>	<b>Appendix.....</b>	<b>77</b>
	<i>Energy deposition in different scintillators thickness .....</i>	<i>77</i>
	<b>Bibliography .....</b>	<b>81</b>



# List of Figures

<i>Figura 1.1: Immagine realizzata con sistema a doppia energia di una chiara minaccia e di un bagaglio contenente molti oggetti [2].....</i>	<i>xxii</i>
<i>Figura 1.2: Meccanismo di scintillazione degli scintillatori inorganici [7].....</i>	<i>xxiv</i>
<i>Figura 1.3: Sistema a scansione a raggi X installato su macchinari FEP .....</i>	<i>xxv</i>
<i>Figura 1.4: Monoblocco AION foto e modello .....</i>	<i>xxviii</i>
<i>Figura 1.5: Monoblocco AION simulazioni e dati sperimentali .....</i>	<i>xxix</i>
<i>Figura 1.6: Monoblocco AION misura e simulazione a 85kV .....</i>	<i>xxix</i>
<i>Figura 1.7: Geometria della simulazione MCNP utilizzata per confrontare gli scintillatori GAGG(Ce) e CsI(Tl) .....</i>	<i>xxx</i>
<i>Figura 1.8: Spettri di emissione di CsI(Tl) e GAGG(Ce), QE del PIN.....</i>	<i>xxx</i>
<i>Figure 1.1: Dual energy image of a pistol in a bag (left) and a lot of clutter in a baggage (right) [2].....</i>	<i>2</i>
<i>Figure 1.2: Associated distribution with respect to detection signal strength, example of threshold shift [1] .....</i>	<i>3</i>
<i>Figure 1.3: Schematic view of a baggage inspection system .....</i>	<i>4</i>
<i>Figure 1.4: Example of good geometries (left) and bad geometry (right) configuration. .</i>	<i>5</i>
<i>Figure 1.5: Pb attenuation coefficient for the photon interaction mechanisms .....</i>	<i>6</i>
<i>Figure 1.6: Gilardoni Spa company [4] .....</i>	<i>7</i>
<i>Figure 1.7: FEP ME 536 device [4] .....</i>	<i>8</i>
<i>Figure 2.1: Radiative losses process, energy referred to Tungsten atom [9] .....</i>	<i>10</i>
<i>Figure 2.2: X-Ray spectrum scheme of X-Ray tube with Tungsten target [9].....</i>	<i>11</i>
<i>Figure 2.3: Energy Exchange within an X-Ray Tube [9].....</i>	<i>12</i>
<i>Figure 2.4: Coolidge X-Ray tube at Gilardoni museum .....</i>	<i>13</i>
<i>Figure 2.5: Gilardoni Spa AION monoblock [4] .....</i>	<i>14</i>
<i>Figure 2.6: Three main step occurring inside the X-Ray detector [2].....</i>	<i>15</i>
<i>Figure 2.7: Operation principle of reflector material [18].....</i>	<i>16</i>
<i>Figure 2.8: Principle of scintillator mechanism in inorganic scintillators [15].....</i>	<i>17</i>
<i>Figure 2.9: PIN photodiode, principle of operation .....</i>	<i>19</i>
<i>Figure 2.10: Quantum efficiency of PMT photocathode compared to Si-PD [10] .....</i>	<i>20</i>
<i>Figure 2.11: A schematic view of the X-Ray scanning system installed in FEP machine</i>	<i>22</i>
<i>Figure 2.12: Schematic view of Philips dual layer detector .....</i>	<i>23</i>
<i>Figure 2.13: Energy deposition spectra in each scintillators, dual energy system [13]..</i>	<i>23</i>
<i>Figure 2.14: Conventional and dual-energy computed tomography images: the solid and dashed arrows point to stones and stents [14].....</i>	<i>24</i>

<i>Figure 2.15: Gilardoni's FEP ME 640 AMX baggage pictures, from below and from lateral side. Colors and B/W [4]</i> .....	25
<i>Figure 3.1: Scintillator evolution [6]</i> .....	28
<i>Figure 3.2: Czochralski single crystal production method [17]</i> .....	29
<i>Figure 3.3: Scintillation spectra of CsI with different activator element and quantum efficiency of amorphous Silicon Photodiode [19]</i> .....	30
<i>Figure 3.4: SEM micrograph of a microcolumnar film of CsI:Tl,Sm [23] and structured scintillator segmented by reflector (white strips) [13]</i> .....	32
<i>Figure 3.5: Afterglow data comparing CsI (Tl) and CsI (Tl,Sm) measured at different temperature [25]</i> .....	34
<i>Figure 3.6: Afterglow of different scintillator [10]</i> .....	35
<i>Figure 3.7: Decrease in gain of a detector based on undoped CsI [8]</i> .....	36
<i>Figure 3.8: Field of application and required parameter importance [22]</i> .....	37
<i>Figure 3.9: Schematic view of spatial resolution improvement due to columnar CsI(Tl)(right) on GOS(Tb) (left) [31]</i> .....	38
<i>Figure 3.10: Emission spectrum of common scintillators [42]</i> .....	47
<i>Figure 3.11: Decay time measurements of CsI(Tl) and GAGG(Ce) [45]</i> .....	48
<i>Figure 4.1: Acquisition system steps with each relevant quantity</i> .....	49
<i>Figure 4.2 Monte Carlo particle simulation scheme</i> .....	51
<i>Figure 4.3: MCNP.txt example</i> .....	53
<i>Figure 4.4: AION monoblock modelling picture</i> .....	54
<i>Figure 4.5: Simulated spectrum of Gilardoni AION monoblock photon source</i> .....	56
<i>Figure 4.6: Experimental setup for spectroscopy analysis</i> .....	57
<i>Figure 4.7: AION monoblock measured energy spectrum with X-123 CdTe spectrometer, normalized unit vs keV</i> .....	58
<i>Figure 4.8: AMPTEK X-123CdTe efficiency [49]</i> .....	59
<i>Figure 4.9: AION monoblock, experimental and simulated spectrum considering spectrometer efficiency</i> .....	60
<i>Figure 4.10: 80kV(a) and 100kV(b) model spectra with different thickness of Aluminium filtration [50]</i> .....	60
<i>Figure 4.11: AION monoblock, simulated spectrum with different Al filtration. Experimental data has been reported as reference</i> .....	61
<i>Figure 4.12: Dead layer simulation geometry, Xming software</i> .....	61
<i>Figure 4.13: Energy spectrum with different dead layer</i> .....	62
<i>Figure 4.14: AION monoblock energy spectrum, different measures</i> .....	62
<i>Figure 4.15: Simulated and experimental spectrums at 85kV and 150kV, with and without filtration</i> .....	64
<i>Figure 4.16: Geometry of the scintillator energy deposition simulations</i> .....	65
<i>Figure 4.17: MCNP-tally f8 (pulse high spectrum) in GAGG(Ce) and CsI(Tl)</i> .....	66

<i>Figure 4.18: Attenuation coefficient trend of CsI(Tl) [51]</i> .....	66
<i>Figure 4.19: GrabIt interface</i> .....	68
<i>Figure 4.20: Emission spectrum of CsI(Tl) and GAGG(Ce). QE of PIN</i> .....	68
<i>Figure 4.21: Interp1 operation example [49]</i> .....	69
<i>Figure A1.1: Geometry of dual energy simulation</i> .....	73
<i>Figure A1.2: Simulated energy spectrum in LES and HES</i> .....	74
<i>Figure A1.3: Emission spectrum of the analyzed scintillator and PIN QE</i> .....	75
<i>Figure A2.1: Simulated energy deposition spectrum for different thickness of GAGG(Ce) scintillator</i> .....	77
<i>Figure A2.2: Simulated energy deposition spectrum for different thickness of CsI(Tl) scintillator</i> .....	78
<i>Figure A2.3: Deposited energy plotted against different value of thickness</i> .....	78
<i>Figure A2.4: MATLAB fits</i> .....	79

## List of Tables

<i>Tabella 1 Risultati finali</i> .....	xxxi
<i>Table 1.1 Possible outcomes of a detection system</i> .....	2
<i>Table 1.2 Photon interaction dependencies upon energy and atomic number [1,3]</i> .....	6
<i>Table 3.1 Survey of selected scintillators [3, 8, 10, 17, 18, 26, 28, 34, 39, 40, 41, 42, ...]</i> .....	45
<i>Table 4.1 AION monoblock filter composition</i> .....	55
<i>Table 4.2 Mass fraction evaluation of Boron trioxide, B<sub>2</sub>O<sub>3</sub></i> .....	55
<i>Table 4.3 Total elemental mass fraction evaluation</i> .....	56
<i>Table 4.4 Fluence ratio evaluation</i> .....	63
<i>Table 4.5 Simulation parameters</i> .....	65
<i>Table 4.6 Efficiency results summary</i> .....	69
<i>Table A1.1 Geometry specification</i> .....	73
<i>Table A1.2 Outcomes of the simulation</i> .....	74
<i>Table A1.3 Matching factor results</i> .....	75



# Acknowledgements

My sincere thanks go to my Advisor Prof. Marco Caresana for believing in my enterprise providing me support, knowledge, and advices.

My special thanks go to my Co-advisor Dott. Gabriele Zorloni for the MCNP teachings and the careful suggestion provided. I am extremely grateful for your assistance throughout my thesis.

I wish to thank Eng. Ludovico Aiello for the time dedicated to my work, I am very grateful for the opportunity he gave me to conclude my university experience getting myself in a real work surrounding.

I want also thank Filippo Fracas for answering to my very first e-mail from which all it started and for the special attention he paid on my project.

I would like to express my appreciation to all the Gilardoni Spa R&D staff who collaborated for the accomplishment of my thesis finding some time during their working days: Matteo Gerosa, Vincenzo Vendemia, Fabio Salvetti, Davide Perego, Luca Ghislanzoni.

I also want to thank all my colleagues of the Nuclear Engineering course, with a special mention to the MateNuc club: Marco, Silvia, Rino, Andrea, Davide, Rafael.

I give my thanks to my friends, who always accepted me for who I am and with whom I have rejoiced a lot of the light-heartedness moments which I will cherish forever. My sincere thanks go to Francesco, Luca, Marco, Filippo, Laura P., Laura G., Stefano M., Massimo, Stefano C.

My deepest gratitude goes to my parents, Federica and Giovanni, and my brother, Saverio, who always supported me in every choice I make.

Last but not least, I want to thank my girlfriend Laura with whom I am able to run away from the complex moment of my life and with whom... I am fine.



# Abstract (English)

Control of luggage and shipped goods are frequently carried out to avoid terrorist attacks and the shipping of potentially illegal and dangerous materials. In this framework, X-Ray technology is widely used to see and to check the baggage contents. An important manufacturer of X-Ray scanning inspection systems, recognized all over the world, is the Gilardoni Spa located in Mandello del Lario. The devices dedicated to the security check are the one belonging to the FEP production line. The aim of this thesis work was a concrete proposal of a FEP performance improvement focusing on the heart of the acquisition system, the scintillator. To reach that goal, we carried out a careful bibliographic analysis with the aim of evaluating the presence in the global market of a suitable, high performing scintillator which meets the needs of the Gilardoni's FEP production line. Our objective was to find a better performing substitute of the CsI(Tl), which is the one actually operating. The research was successfully concluded identifying a candidate scintillator. The chosen one is the recently discovered GAGG(Ce) scintillator. To evaluate the performances of the contender scintillator in the FEP acquisition system we developed a reliable method taking into account every acquisition steps efficiency. The X-Rays energy deposition into the scintillator material was evaluated with a Monte Carlo simulation creating a model of the Gilardoni's photon source, the AION monoblock. The simulations were carried out with MCNP code considering all its components and subsequently they were validated against experimental data. The goodness of scintillator photodiode matching was assessed with a dedicated MATLAB code. The results were promising and auspicious, the advantage in performance were estimated to be up to 16%. Conclusively we wanted to point out that the GAGG(Ce) is theoretically more performant in correspondence with the CsI(Tl). However, for the final application, other features must be evaluated with a preliminary sample test.

In the field of radiation detector, we provided a rigorous procedure to evaluate the theoretical goodness of scintillator in a specific application. We were able to create a valuable instrument that allowed the Gilardoni Spa to believe that there are possible and different solutions that can give them advantages in the developments of their products.



# Abstract (Italiano)

Il controllo dei bagagli e delle merci è da sempre considerato un metodo efficace per evitare attacchi terroristici e controllare il commercio illegale di materiali e sostanze potenzialmente pericolose. La tecnologia a raggi X è ampiamente utilizzata per visualizzare e controllare il contenuto dei bagagli. Un importante produttore di scanner a raggi X, riconosciuto in tutto il mondo, è la Gilardoni Spa di Mandello del Lario. I dispositivi dedicati al controllo di sicurezza sono quelli appartenenti alla linea di produzione FEP. L'obiettivo di questo lavoro di tesi è stato quello di creare una proposta concreta che portasse a un miglioramento delle prestazioni FEP. Per fare ciò ci siamo concentrati sul sistema di acquisizione ed in particolare sullo scintillatore, effettuando un'attenta analisi bibliografica con lo scopo di valutare la presenza di nuovi scintillatori sul mercato adatti alle esigenze dell'azienda. La ricerca è stata conclusa con successo identificando lo scintillatore GAGG(Ce) come possibile sostituto all'attuale CsI(Tl). Per valutare le prestazioni del rilevatore con il nuovo scintillatore proposto abbiamo sviluppato un metodo rigoroso che tenesse conto dell'efficienza di ogni step del processo di acquisizione. La deposizione di energia dei raggi X all'interno del materiale scintillante è stata stimata con una simulazione Monte Carlo, creando un modello della sorgente di fotoni utilizzata dalla Gilardoni: il monoblocco AION. Le simulazioni sono state eseguite con il software MCNP e successivamente validate sulla base di dati sperimentali. Il matching tra fotodiode e scintillatore è stato valutato con un codice MATLAB sviluppato appositamente. I risultati sono stati promettenti: il vantaggio in termini di prestazioni è stato stimato pari al 16%. Dalle nostre valutazioni è emerso che lo scintillatore GAGG(Ce) è più performante rispetto all'attuale CsI(Tl) nel sistema di acquisizione FEP. Tuttavia, per un'applicazione pratica, ulteriori proprietà dello scintillatore devono essere prese in considerazione e possibilmente valutate tramite un test sperimentale su un campione di materiale.

Con il nostro lavoro, siamo stati in grado di fornire un valido metodo capace di stimare la bontà teorica di un nuovo scintillatore in una specifica applicazione. Questo strumento, unito al modello MCNP sviluppato, potrà aiutare la Gilardoni Spa nella valutazione di future soluzioni innovative per quanto riguarda lo sviluppo dei loro prodotti.



# Estratto

I controlli di sicurezza nel mondo dei trasporti hanno sempre ricoperto un ruolo fondamentale. Il mercato della sicurezza, specialmente quello dedicato alla sicurezza aeroportuale, richiede da sempre grandi sforzi per innovazione e sviluppo. Lo scopo principale è quello di evitare attacchi terroristici che, come l'attacco del 11/09 alle Torri Gemelle, possono portare a conseguenze devastanti. In questo ambito trovano spazio tecnologie avanzate come l'utilizzo dei sistemi a scansione a raggi X.

*“La Gilardoni Spa è un'azienda nata nel 1947 da una coraggiosa iniziativa del Dott. Ing. Arturo Gilardoni che l'ha voluta basata sulla ricerca, fondata sulla qualità e dedicata all'innovazione”.*

Ad oggi l'azienda è tra i principali produttori di apparecchiature a raggi X ed è presente in tre diversi settori: medicale, sicurezza e controlli non distruttivi (CND) [1]. Gilardoni Spa offre una vasta gamma di prodotti che trovano applicazioni sia nel mercato aeroportuale che nel mercato non-aviation, incentrato su applicazioni in edifici di pubblica importanza. Ogni prodotto deve essere certificato da un istituto competente come l'ECAC (European Civil Aviation Conference). Le certificazioni si basano su test CTM (Common Testing Methodology) che tengono in considerazione l'affidabilità della macchina e la frequenza di Falsi Positivi (FP).

L'operatore che analizza le immagini dei bagagli scansionati ha il compito di prendere una decisione in base ad una soglia di allarmismo percepita. Nel momento in cui l'operatore ritiene ci sia una minaccia, il bagaglio passa ad un'analisi di secondo livello che prevede l'apertura e l'analisi manuale del medesimo. Queste procedure richiedono l'impiego di tempo, e nel caso di un falso positivo il passeggero può sentirsi ingiustamente accusato. Un operatore di sicurezza si trova in difficoltà nel momento in cui la minaccia non appare chiara nell'immagine, come nell'esempio di destra riportato in Figura 1.1. Infatti, a differenza della scansione sulla sinistra, in cui la sagoma di una pistola è molto chiara, nella scansione a destra vi sono molti oggetti non facilmente identificabili [2]. L'accuratezza dell'immagine finale porta quindi un beneficio a livello di prestazioni generali del sistema di sicurezza. Nei sistemi a scansione utilizzati in ambito di sicurezza, l'impiego dei raggi X è analogo a quello normalmente adoperato in campo medico radiologico. Il rivelatore è posizionato dalla parte del bagaglio opposta alla sorgente di radiazioni ed il suo compito è quello di rivelare la radiazione trasmessa attraverso il bagaglio. L'immagine prodotta consente di vedere eventuali oggetti presenti, tra cui quelli nascosti nelle sue cavità interne.

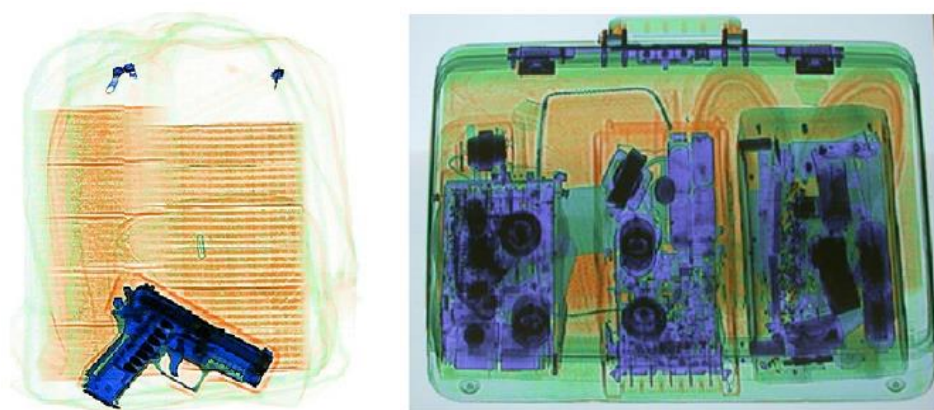


Figura 1.1: Immagine realizzata con sistema a doppia energia di una chiara minaccia e di un bagaglio contenente molti oggetti [2]

L'obiettivo principale di questo lavoro è quello di migliorare le prestazioni dei macchinari Gilardoni FEP, ovvero quelli dedicati alla scansione di bagagli, concentrandoci sul sensore primario della radiazione: lo scintillatore. Prima di tutto cercheremo di capire il loro funzionamento addentrando nella fisica dei sistemi a scansione a raggi X. Nella situazione più semplice in cui i fotoni sono monoenergetici e attraversano uno spessore di materiale in un setup sperimentale di "buona geometria" l'attenuazione del fascio è stabilita dalla legge di Lambert-Beer (Eq. 1.1) [3, 4].

$$I = I_0 e^{-\mu t} \quad (1.1)$$

In questa equazione  $I$  è l'intensità trasmessa mentre  $I_0$  è l'intensità incidente sul materiale.  $\mu$  rappresenta il coefficiente di attenuazione lineare e  $t$  lo spessore del materiale. Introducendo la dipendenza dalla densità  $\rho$ , l'equazione, ora scritta per  $N$  numero di fotoni, diventa:

$$N = N_0 e^{-\frac{\mu}{\rho} \rho t} \quad (1.2)$$

Per un campione contenente diversi materiali il coefficiente di attenuazione sarà pari ad una media pesata tenendo conto delle frazioni in peso  $w_i$ :

$$\frac{\mu}{\rho} = w_1 \frac{\mu_1}{\rho_1} + w_2 \frac{\mu_2}{\rho_2} + \dots \quad (1.3)$$

Ogni coefficiente è la somma di più probabilità che tengono conto delle diverse modalità di interazione dei fotoni: effetto Fotoelettrico, scattering Compton, scattering Rayleigh, produzione di coppie. La probabilità che ognuno di questi processi avvenga è strettamente legata all'energia del fotone interagente e dal numero atomico ( $Z$ ) del materiale campione [5]. Questo porta ad avere un'immagine su scala di grigi che rappresenta la proiezione del coefficiente di attenuazione medio lungo ogni segmento verticale del campione.

I sistemi di scansione a raggi X Gilardoni utilizzano come sorgente i monoblocchi AION, prodotti internamente all'azienda. Questo componente è composto a sua volta dalla sorgente vera e propria di fotoni (tubo a raggi X) e da un sistema di raffreddamento dedicato. La produzione di raggi X avviene tramite il processo Bremsstrahlung. Alcuni elettroni emessi per effetto termoionico da un filamento incandescente di Tungsteno (catodo) vengono accelerati all'interno di un involucro di vetro verso un target composto anch'esso di Tungsteno. Gli elettroni perdono energia all'interno del materiale tramite collisioni e emissione radiative con una provabilità specifica per cammino  $x$  dettata dalla seguente equazione:

$$\frac{(dE/dx)_r}{(dE/dx)_c} \approx \frac{EZ}{700} \quad (1.4)$$

Affinché le perdite radiative siano elevate rispetto a quelle collisionali è necessario che gli elettroni vengano accelerati ad alte energie  $E$  e che si utilizzi un materiale ad alto  $Z$  [3, 5]. I fotoni emessi hanno diverse energie a seconda di quanta energia l'elettrone perde nella sua collisione con gli atomi target. È altresì possibile che i fotoni vengano prodotti tramite eccitazione e successiva diseccitazione di un atomo target. Questi fotoni vengono emessi a determinati valori di energia caratteristici dell'atomo target (da qui il nome *radiazione caratteristica*). Lo spettro finale dei fotoni è quindi composto da una parte continua data dall'emissione Bremsstrahlung e da una parte discreta originata dalla radiazione caratteristica.

Il rivelatore di raggi X montato sui sistemi FEP si basa sul principio della conversione indiretta. I fotoni X sono prima convertiti in fotoni visibili e poi, in un secondo step, in elettroni. Il sensore primario è lo scintillatore mentre quello secondario è il fotodiodo. Sulle macchine Gilardoni il sistema è composto da uno scintillatore di Ioduro di Cesio drogato con Tallio (CsI(Tl)) e da un fotodiodo al Silicio cristallino comunemente chiamato PIN.

Per quanto riguarda la rilevazione di fotoni ad alta energia, come la radiazione gamma e i raggi X, è sempre preferibile l'utilizzo di scintillatori ad alto potere frenante come quelli inorganici. Il CsI(Tl) è uno scintillatore a stato solido inorganico in cui il processo di scintillazione è caratteristico della struttura elettronica a bande energetiche associata al reticolo cristallino [6].

Come mostrato in Figura 1.2 quando la radiazione interagisce con il materiale cristallino può trasferire una quantità sufficiente di energia ad un elettrone e portarlo dalla banda di valenza a quella di conduzione. In questa banda l'elettrone ha un'energia tale da permettergli di muoversi nel reticolo cristallino del materiale. Le radiazioni molto energetiche (come i fotoni  $x$ ) creano un grande numero di elettroni nella banda di conduzione.

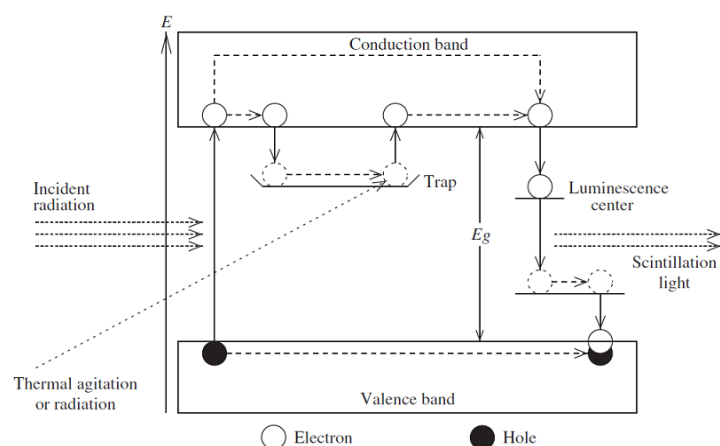


Figura 1.2: Meccanismo di scintillazione degli scintillatori inorganici [7]

Questi elettroni possono tornare direttamente alla banda di valenza emettendo un fotone ma questo processo è però poco efficace a causa dell'auto assorbimento dello stesso da parte di un altro elettrone. Inoltre, il fotone emesso avrebbe una lunghezza d'onda che tipicamente non appartiene allo spettro visibile. Per questo motivo il materiale deve essere "attivato" e ciò è fatto tramite l'aggiunta di atomi-impurità che vanno ad occupare siti interstiziali nel reticolo cristallino. Questi creano stati energetici intermedi tra la banda di valenza e quella di conduzione rendendo possibile il processo di scintillazione con buona efficienza. La scelta degli atomi attivatori è molto importante perché influenza la maggior parte delle caratteristiche di uno scintillatore come ad esempio il tempo di decadimento, la resa luminosa e soprattutto la lunghezza d'onda dei fotoni emessi [7].

A seguito del processo di scintillazione vengono quindi emessi un grande numero di fotoni con uno spettro caratteristico che ricade nel range del visibile. Questi fotoni vengono trasportati fino al fotodiodo PIN nel quale avviene la conversione in elettroni. Ciascuna lunghezza d'onda dei fotoni emessi dallo scintillatore è convertita con diversa efficienza. L'efficienza di trasformazione per ciascuna lunghezza d'onda è detta *efficienza quantica* (QE) dello scintillatore ed è caratteristica di ciascun foto-rilevatore.

I rilevatori di raggi X possono essere ottimizzati considerando *coupling* e *matching* tra scintillatore e fotodiodo. Un buon accoppiamento ottico è tale quando i due componenti hanno un indice di rifrazione simile, in questo modo la rifrazione della luce visibile proveniente dallo scintillatore viene minimizzata e il numero di fotoni che giungono al fotodiodo è ottimizzato [8]. Il matching invece riguarda le performance di conversione del foto-rilevatore. Affinché questo processo avvenga in modo efficiente è infatti necessario che lo spettro dei fotoni emessi dallo scintillatore corrisponda alle lunghezze d'onda in cui la QE del fotodiodo è massima.

Uno disegno schematico dei sistemi FEP della Gilardoni raggi X è riportato in Figura 1.3.

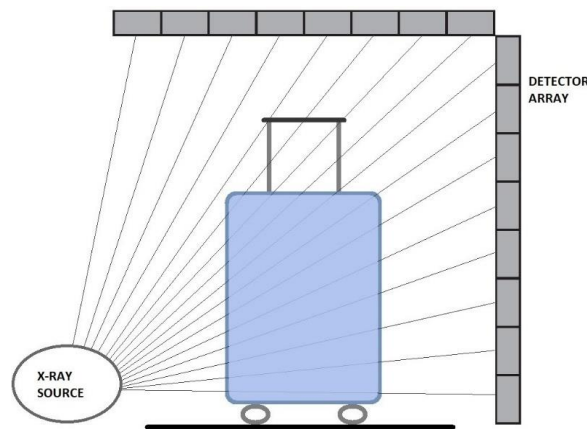


Figura 1.3: Sistema a scansione a raggi X installato su macchinari FEP

Il sistema usa un fascio di raggi X a ventaglio generato dal monoblocco AION posto in basso a sinistra in figura. I fotoni che vengono utilizzati hanno un'energia massima di 150kV e una tipica corrente di lavoro è di 1mA. Il bagaglio da ispezionare scorre su un rullo motorizzato e il fascio lo attraversa per successive sezioni. Le proiezioni di ciascuna sezione che vengono rilevate da un detector ad array con struttura ad L posto dal lato opposto del bagaglio. Le scansioni vengono successivamente elaborate da un software dedicato che ne ricostruisce la geometria. Un'immagine più accurata può essere ottenuta usando un sistema a doppia energia in grado di fornire informazioni sull'energia dei fotoni interagenti. Tipicamente questi rilevatori hanno una struttura a *sandwich* in cui due scintillatori sono separati da un filtro. I fotoni rilevati dal primo scintillatore sono quelli che hanno un maggior potere frenante e quindi quelli aventi bassa energia. Mentre al secondo scintillatore giungono solo quelli in grado di oltrepassare il filtro e quindi quelli più energetici. Questa informazione grossolana sull'energia può essere utilizzata per ricostruire più accuratamente la proiezione del bagaglio ispezionato.

Dopo aver compreso approfonditamente il funzionamento dei sistemi a scansione a raggi X ci siamo focalizzati sul sensore primario. Gli scintillatori vengono comunemente utilizzati in ambito medicale, in esperimenti di fisica ad alta energia, in ambito dosimetrico così come in sistemi di scansione volti ad applicazioni industriali. Il mercato globale ha subito una forte crescita negli ultimi decenni spinto da un'esigenza di miglioramento delle performance dei sistemi di acquisizione usati nei diversi ambiti. La nostra ricerca si è focalizzata sugli scintillatori inorganici in quanto mostrano le migliori prestazioni in termini di rilevazione di fotoni ad alta energia grazie alla loro elevata densità e al loro elevato numero atomico ( $Z$ ).

Gli scintillatori di questa categoria sono cresciuti tipicamente con il metodo Czochralski ottenendo una struttura cristallina quasi perfetta oppure possono avere

una struttura ceramica. In quest'ultimo caso non sono composti da un unico singolo cristallo bensì da molti micro-cristalli, detti grani, che vengono compattati tra di loro tramite il processo di sinterizzazione e pressurizzazione a caldo. Ad oggi rappresentano una vera e propria nuova classe di scintillatori [9, 10].

Per valutare la bontà di uno scintillatore in una specifica applicazione devono essere considerate una serie di proprietà, le principali sono elencate di seguito:

- La resa luminosa e la linearità della risposta con la dose assorbita
- La trasparenza e l'efficienza di trasporto della luce visibile
- Il potere frenante
- Il tempo di decadimento primario e l'afterglow
- La stabilità chimica e la resistenza ai danni da radiazione
- Dipendenza delle proprietà dalla temperatura

Negli anni, alcuni scintillatori sono stati prodotti con proprietà appositamente sviluppate per sopperire ad esigenze di specifiche applicazioni. Ne è un esempio lo scintillatore BGO che venne sviluppato attorno agli anni 80 con spiccate caratteristiche temporali adatte alla rilevazione di fotoni di annichilazione prodotti durante un'analisi PET [11]. Altri scintillatori sono stati invece prodotti con microstrutture cristalline innovative al fine di migliorarne alcune proprietà come l'efficienza di trasporto dei fotoni visibili. Il CsI(Tl), ad esempio, è utilizzato negli schermi CCD per imaging medico con una microstruttura colonnare in grado di canalizzare la luce verso il foto-rilevatore [12]. Questa struttura oltre a migliorarne l'efficienza è anche utile a ridurre il fenomeno del cross-talk. Infatti, inducendo una direzione preferenziale al moto dei fotoni riduce la loro diffusione all'interno dello scintillatore. Il risultato finale è visibile nell'immagine in cui si evince una miglior risoluzione spaziale. Recentemente, un crescente interesse è stato posto sugli scintillatori appartenenti alla classe dei granati attivati con ioni di Cerio [9]. Tra di essi le migliori performance sono state raggiunte dallo scintillatore GAGG(Ce) con una resa luminosa di oltre 60000ph/MeV e un ottimo potere frenante [13]. Ad oggi questo scintillatore è commercializzato nella versione cristallina ma gruppi di ricerca stanno lavorando per crearne una versione ceramica. Alcuni risultati sono già stati riportati e mettono in luce un ulteriore miglioramento delle proprietà ottiche [14]. Un materiale ceramico con ottime proprietà luminose è il ossi-solfuro di Gadolinio comunemente chiamato GOS e attivato con Praseodimio (Pr). Le peculiarità di questo scintillatore sono una ridotta afterglow e buone caratteristiche temporali che lo rendono un candidato per applicazioni di imaging come la tomografia computerizzata (CT) [15].

Oltre a questi abbiamo analizzato altri scintillatori di varia natura come il  $\text{CdWO}_4$ ,  $\text{PbWO}_4$ , la classe degli ossi-orto Silicati contenente gli scintillatori LSO, LYSO, GSO così come i composti di Alluminio Perovskite YAP, LuAP, LuYAP.

Anche la classe di scintillatori basati su alogenuri di Lantanio è stata presa in considerazione. La loro scoperta si attesta attorno all'anno 2000. Le migliori prestazioni sono ottenute con il cloruro di Lantanio e con il bromuro di Lantanio ( $\text{LaCl}_3$  e  $\text{LaBr}_3$ ) che sono due scintillatori attivati con Cerio. Essi presentano un'alta resa luminosa e tempi di decadimento rapidi dell'ordine dei ns. Altri scintillatori dalle ottime prestazioni sono ancora in fase di ricerca come quelli attivati con Europio (Eu). Ne è un esempio lo ioduro di Stronzio  $\text{SrI}_2(\text{Eu})$  la cui resa luminosa supera i 100000ph/MeV [16].

Tra tutti questi scintillatori abbiamo cercato un candidato in grado di migliorare le prestazioni del sistema di acquisizione usato nei macchinari FEP Gilardoni. Per fare ciò abbiamo tenuto conto della capacità dello scintillatore di stoppare la radiazione considerando densità e Z del materiale scintillante, la resa luminosa, l'afterglow e la non igroscopicità ed anche la lunghezza d'onda di picco dei fotoni emessi. Il tempo di decadimento primario è una caratteristica di seconda importanza in quanto il rivelatore lavora in current mode, cioè non viene rilevato il singolo impulso di corrente ma bensì viene integrata la corrente in un certo intervallo temporale. Abbiamo scelto di valutare nel dettaglio le performance del sistema utilizzando lo scintillatore GAGG(Ce). Questo scintillatore di alta resa luminosa possiede un'elevata densità e un alto Z efficace grazie alla presenza del Gadolinio. Inoltre, lo spettro di emissione è piccato ad alte lunghezze d'onda corrispondenti ad un'alte efficienze quantiche del PIN.

Per valutare le performance dell'intero sistema di acquisizione con il nuovo scintillatore abbiamo creato un modello che tenesse in considerazione l'efficienza di tutti gli step che concorrono al processo di acquisizione. Abbiamo quindi considerato l'energia depositata nello scintillatore, l'efficienza con cui è trasformata in luce visibile e l'efficienza con cui il foto-rilevatore trasforma la luce in corrente all'uscita del sistema. Possiamo riassumere tutti questi processi nella seguente equazione:

$$N^{\circ}e^{-} = E_d \cdot [\text{Mev}] \cdot LY \left[ \frac{\text{Ph}_{vis}}{\text{Mev}} \right] \cdot QE \left[ \frac{e^{-}}{\text{Ph}_{vis}} \right] \quad (1.5)$$

Quest'ultima rappresenta il numero medio di elettroni che vengono create dal sistema di rilevazione quando un fotone X impatta sullo scintillatore.  $E_d$  è l'energia media depositata nello scintillatore da un fotone proveniente dalla sorgente Gilardoni AION monoblocco. LY è la resa in luce luminosa dello scintillatore e QE è l'efficienza quantica media del PIN. La resa luminosa è un parametro noto, tipicamente fornito dal produttore dello scintillatore. L'energia depositata nello scintillatore e il parametro riguardante il matching hanno invece richiesto lo sviluppo di analisi approfondite.

Per valutare l'energia depositata nello scintillatore abbiamo utilizzato MCNP: un codice Monte Carlo che simula il trasporto di particelle all'interno della materia [17]. MCNP è un software molto versatile che permette di simulare vari tipi di sorgenti e di registrarne i loro effetti in complesse geometrie. L'utente può richiedere infatti una serie di output che vengono chiamati tally. I tally di nostro interesse saranno il tally f4 riguardante la fluenza dei fotoni e il tally f8 che invece rileva l'energia depositata. L'energia depositata nello scintillatore dipende però fortemente dall'energia dei fotoni incidenti e quindi dallo spettro emesso dal monoblocco AION. Quest'ultimo non è a noi noto pertanto è stato necessario sviluppare un modello anche per quanto concerne la sorgente. In Figura 1.4 è mostrata una foto del monoblocco e il modello creato.

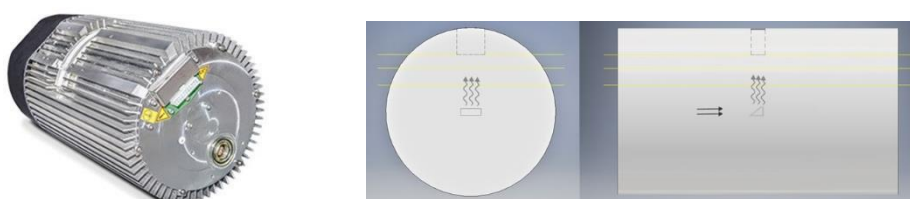


Figura 1.4: Monoblocco AION foto e modello

Nella simulazione MCNP abbiamo tenuto conto degli elettroni provenienti dal filamento di Tungsteno e accelerati a 150kV creando una sorgente di elettroni (freccie diritte in figura) di energia 150keV aventi direzione perpendicolare al target di Tungsteno posto a 45°. All'interno del target, MCNP simula le varie interazioni tra cui il processo di Bremsstrahlung che porta alla formazione di fotoni che fuoriescono dalla parte superiore del target (freccie ondulate in figura). Questi vengono poi filtrati da vetro borosilicato, dall'olio di raffreddamento e dal conetto di uscita raggi composto di PBT. Per ogni materiale è stata calcolata la composizione elementare e sono stati inseriti nella geometria con i rispettivi spessori. All'uscita della finestra in PBT è stata registrata la fluenza utilizzando il tally f4. Con lo scopo di validare la simulazione è stata effettuata una misura spettrometrica della sorgente nei laboratori dell'azienda Gilardoni Spa. Il rivelatore utilizzato in questo caso è stato il X-123 CdTe prodotto dall'azienda AMPTEK [18]. I risultati della simulazione e dell'esperimento sono mostrati in Figura 1.5.

I picchi caratteristici del Tungsteno posti a 59keV e 67keV sono ben visibili in tutti gli spettri. I dati sperimentali differiscono però di molto da quelli simulati nella regione delle basse energie. Anche considerando l'efficienza del rivelatore il risultato non è stato soddisfacente.

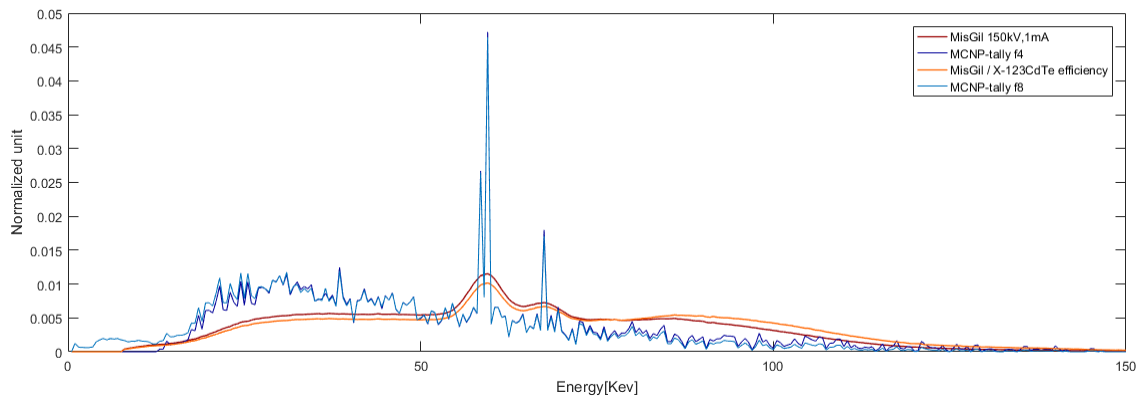


Figura 1.5: Monoblocco AION simulazioni e dati sperimentali

Per questo motivo abbiamo approfondito la nostra analisi cercando di creare nuove simulazioni che tenessero in considerazione le non idealità del rivelatore. Dapprima abbiamo provato a simulare una filtrazione equivalente per diversi mm di Al. Successivamente abbiamo simulato dettagliatamente il rivelatore introducendo nella simulazione la finestra di Berillio, i contatti in platino e diversi spessori di strato morto di CdTe. Nessuna delle precedenti analisi ha dato risultati convincenti.

A questo punto abbiamo messo in discussione la bontà delle misure ipotizzando la presenza di una componente di Pile Up nei conteggi del rivelatore CdTe non trascurabile. Sono state quindi svolte diverse misure a 150kV e a 85kV con e senza una filtrazione aggiuntiva di 1mm di Rame e sono state create le corrispondenti simulazioni. I risultati hanno mostrato una buona corrispondenza tra misure e simulazioni a 85kV anche per quanto riguarda il rapporto tra l'integrale della fluena con e senza filtro. In Figura 1.6 è riportato il miglior risultato ottenuto a 85kV.

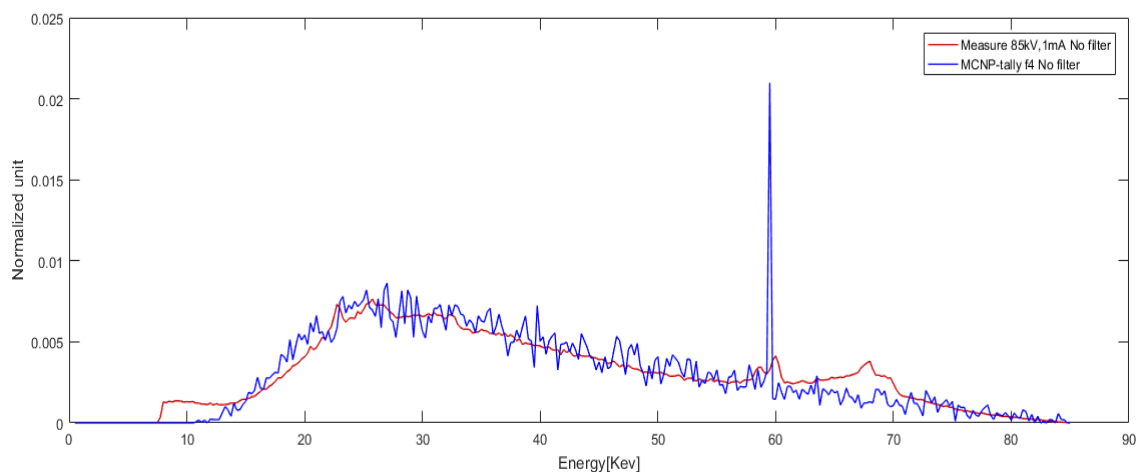


Figura 1.6: Monoblocco AION misura e simulazione a 85kV

Ora, ritenendo validate le simulazioni, ci siamo concentrati sulla deposizione di energia nello scintillatore. Abbiamo creato quindi una nuova geometria con MCNP come quella riportata in Figura 1.7 in cui lo scintillatore (in nero in figura), spesso 1mm, è posto a 50 cm di distanza dalla sorgente. Tra di essi è posta uno spessore di 4mm di Al (blu in figura) che vuole essere una filtrazione equivalente a un bagaglio che viene ispezionato dal macchinario FEP. Tutto il sistema è racchiuso in un parallelepipedo di dimensioni 5x5cm.

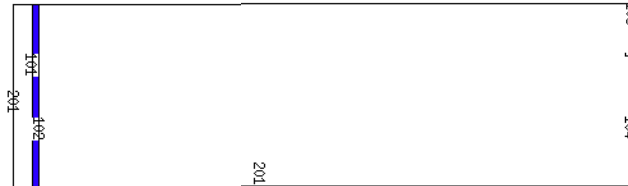


Figura 1.7: Geometria della simulazione MCNP utilizzata per confrontare gli scintillatori GAGG(Ce) e CsI(Tl)

I risultati hanno mostrato una deposizione di energia leggermente migliore per quanto riguarda il GAGG(Ce) con un'energia totale depositata di 27,19keV rispetto a 27,00keV del CsI(Tl) per fotone emesso dalla sorgente.

Per valutare la bontà del matching abbiamo invece utilizzato un codice MATLAB. Lo spettro di emissione del CsI(Tl), la QE del PIN non sono a noi noti e per questo motivo ci siamo affidati a dati ricercati in letteratura [11, 15]. I dati riportati in forma grafica non sono utili per un'elaborazione. Abbiamo quindi utilizzato il tool di MATLAB GrabIt per trasformarli in dati numerici. Lo spettro di emissione del GAGG(Ce) è stato reso disponibile da misure effettuate dal Politecnico di Milano in una precedente ricerca. I risultati normalizzati ad un'area unitaria sono riportati in Figura 1.8.

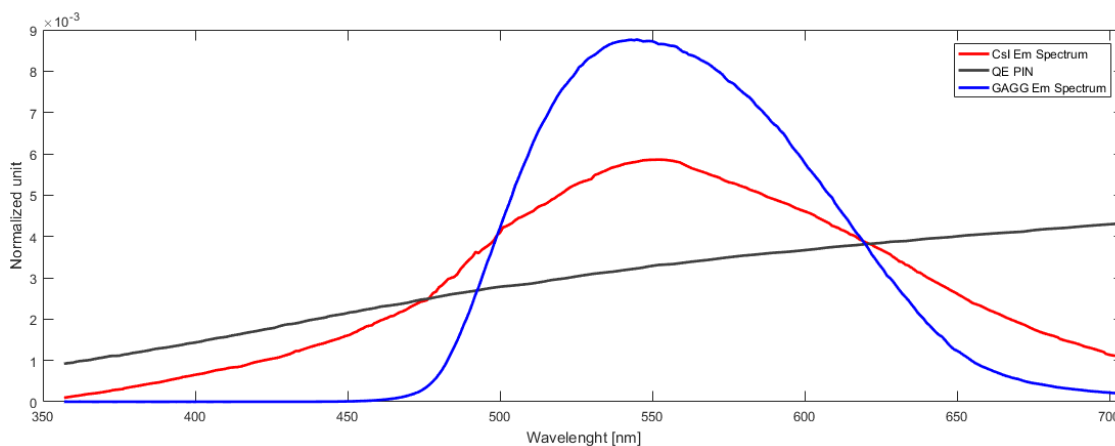


Figura 1.8: Spettri di emissione di CsI(Tl) e GAGG(Ce), QE del PIN

A questo punto abbiamo sviluppato un codice che effettuasse il folding tra lo spettro di emissione del CsI(Tl) e del GAGG(Ce) con la QE del PIN. Dello spettro

risultante ne è stato calcolato l'integrale. Questo valore corrisponde al numero medio di  $e^-$  che vengono emessi dal fotodiodo per fotone visibile emesso dallo scintillatore tenendo in considerazione del rispettivo spettro di emissione.

I risultati ottenuti sono riportati nella Tabella 1 seguente.

*Tabella 1 Risultati finali*

	<i>CsI(Tl)</i>	<i>GAGG(Ce)</i>	<i>HLY-GAGG(Ce)</i>
<i>Deposited energy [MeV]</i>	2.70E-02	2.72E-02	2.72E-02
<i>Light yield [ph/MeV]</i>	54000	54000	60000
<i>Matching conversion factor [e<sup>-</sup>/ph]</i>	50.69E-02	52.36E-02	52.36E-02
<i>Emitted e<sup>-</sup></i>	739.22	769.07	854.52
<i>Gain</i>	0	4.0%	15.6%

Per la nostra analisi finale abbiamo preso in considerazione uno scintillatore GAGG(Ce) avente una resa luminosa pari a quella del CsI(Tl) ed uno scintillatore "reale" ovvero quello fornito dall'azienda Kinheng nella versione High Light Yield (HLY) più luminosa. Per queste versioni del GAGG(Ce) è stato calcolato il guadagno teorico in uscita del segnale rispetto al CsI(Tl). I risultati sono molto promettenti. Per il GAGG(Ce) di pari resa luminosa il guadagno ottenuto è stato del 4,03% mentre nella sua versione più luminosa il guadagno ha raggiunto il 15,59%. I risultati ottenuti ci portano a concludere che lo scintillatore GAGG(Ce) è teoricamente più performante del CsI(Tl) nella nostra applicazione.

Nella nostra analisi abbiamo tenuto conto dell'energia depositata in esso da parte di una sorgente fotonica avente spettro di emissione pari a quello realmente emesso dal monoblocco AION e della bontà del matching con il fotodiodo PIN. Lo studio di questi scintillatori dovrà ora proseguire con un primo test sperimentale per valutarne praticamente i vantaggi e per considerarne altre proprietà, non meno importanti, che non sono state considerate nella nostra analisi. Una di queste è l'afterglow dello scintillatore GAGG(Ce) di cui non si ha una chiara evidenza nella letteratura ad oggi disponibile. Articoli recenti riportano buone prestazioni per quanto riguarda il GAGG(Ce) rispetto al CsI(Tl) [19], tuttavia informazioni dettagliate e complete devono ancora essere riportate. Questo lavoro ha voluto creare un metodo affidabile e efficace per la valutazione di nuovi scintillatori nella applicazione della Gilardoni Spa. Inoltre, la modellizzazione del sistema sorgente-scintillatore creata con MCNP apre a nuovi sviluppi futuri per quanto riguarda l'R&D di questi macchinari.

# Bibliografia

- [1] *Gilardoni x-ray website*, <https://www.gilardoni.it/>
- [2] H. Vogel, D. Haller. (2007), "*Luggage and shipped goods*", Ireland, European Journal of Radiology, 2, P.242-253
- [3] Arturo Gilardoni. (1973), "*Raggi x in medicina*"
- [4] K. Wells, D. A. Bradley. (2012), "*A review of X-ray explosives detection techniques for checked baggage*", Applied Radiation and Isotopes, 8, P.1729-1746
- [5] Knoll. (2010), "*Radiation detection and measurement* "
- [6] Takayuki YANAGIDA. (2018), "*Inorganic scintillating materials and scintillation detectors*", Japan, Proceedings of the Japan Academy, Series B, 2, P.75-97
- [7] Syed Naeem Ahmed. (2014), "*Physics and Engineering of Radiation Detection*", San Diego, CA, USA
- [8] Jin Hyoung Bai, Joo Ho Whang. (2011), "*The Optimization of CsI(Tl)-PIN Photodiode for High-Energy Gamma-Ray Detection*", Progress in Nuclear Science and Technology, P.308-311
- [9] Martin Nikl, Akira Yoshikawa. (2015), "*Recent R&D Trends in Inorganic Single-Crystal Scintillator Materials for Radiation Detection*", Advanced Optical Materials, 4, P.463-481
- [10] Jarek Glodo, Yimin Wang, Ryan Shawgo, et al. (2017), "*New Developments in Scintillators for Security Applications*", Physics Procedia, P.285-290
- [11] Paul Lecoq, Alexander Gektin, Mikhail Korzhik. (2017), "*Inorganic Scintillators for Detector Systems*", Cham
- [12] S. L. Bugby, L. K. Jambi, J. E. Lees. (2016), "*A comparison of CsI:Tl and GOS in a scintillator-CCD detector for nuclear medicine imaging*", Journal of Instrumentation, 9, P.P09009
- [13] M. Kitaura, A. Sato, K. Kamada, A. Ohnishi, M. Sasaki. (2014), "*Phosphorescence of Ce-doped Gd<sub>3</sub>Al<sub>2</sub>Ga<sub>3</sub>O<sub>12</sub> crystals studied using luminescence spectroscopy*", Journal of Applied Physics, 8

- [14] Takayuki Yanagida, Kei Kamada, Yutaka Fujimoto, Hideki Yagi, Takagimi Yanagitani. (2013), "*Comparative study of ceramic and single crystal Ce:GAGG scintillator*", *Optical Materials*, 12, P.2480-2485
- [15] C. Greskovich, S. Duclos. (1997), "*CERAMIC SCINTILLATORS*", Palo Alto, CA 94303-0139, *Annual Review of Materials Science*, 1, P.69-88
- [16] Nerine Cherepy, Benjamin Sturm, Owen Drury, et al. (Jan 1, 2009), "*SrI2 scintillator for gamma ray spectroscopy*", United States
- [17] *MCNP website*, <https://mcnp.lanl.gov/>
- [18] "*Amptek X-123 CdTe spectrometer brochure*"
- [19] Matthew Lowdon, Peter G. Martin, M. W. J. Hubbard, et al. (2019), "*Evaluation of Scintillator Detection Materials for Application within Airborne Environmental Radiation Monitoring*", Switzerland, *Sensors (Basel, Switzerland)*, 18, P.3828



# 1 Context analysis

## 1.1 Baggage check

The demands for security baggage checks are nowadays enormous. Four main purposes lead to the need for screening passengers and their baggage: the illegal movement of goods or prohibited items, fraud, tax evasion and, in ever-increasing importance, the terrorist threats.

Avoid terrorist attacks is the primary focus of baggage security operations, especially in airport security applications, following the devastating 9/11 attacks. The aviation safety legislation belongs to the International Civil Aviation Organization (ICAO) which is a United Nations specialized agency which was founded in 1947 by 52 countries that agreed to the Chicago Convention. The primary purpose of the agency is to update the legislation in the various fields of civil aviation by providing recommendations to member countries, in particular regarding to flight and passenger safety.

In the Chicago Convention 18 Annexes were adopted. They contain Standard Practices, mandatory rules for ICAO members and Recommended Practices. ICAO's Annex 17 sets the minimum level of aviation security standards expected from all member states and therefore all the governments must institute their own aviation security agency under the ICAO Annex 17. The development of airport security policies strictly follow a supplementing Annex named ICAO DOC 8973. This document provides standards for pre-board screening of passengers and baggage, the quality of scanners and their periodic testing procedures, cargo security controls and so on [1].

Explosives detection focuses mainly on the research of HME (Home-made explosives) in hand or hold baggage, whose composition and appearance can easily be confused with benign everyday luggage items. There are essentially four major approaches available for screened baggage inspection: manual hand search, sniffer dogs, trace explosives detection (TED) and the automated X-Ray inspection including certified explosive detection systems.

Manual search is slow and laborious, with an inspection rate of only a few tens of bags per hour. Sniffer dogs can carry again only a few hundred bags per hour. Manual inspection and sniffer dogs are then too slow as primary inspection methods, and therefore they are often used as a second-level inspection once an initial trigger

is produced. For these reasons automated X-Ray inspection systems using radiographic methods are the most common devices for initial baggage screening.

The output X-Ray image reveals both the shape and density of the contents of the luggage: items whose characteristics are similar to those of known explosives are identified as potential threats. All those machines must be certified by the competent institutes – ECAC (European Civil Aviation Conference) certifies compliance according to the ICAO directives. The certification of a system takes into consideration the reliability of the scanner basing on the number of false positives and false negatives produced by the system. If we assume that a binary decision has to be taken, we then have two options:

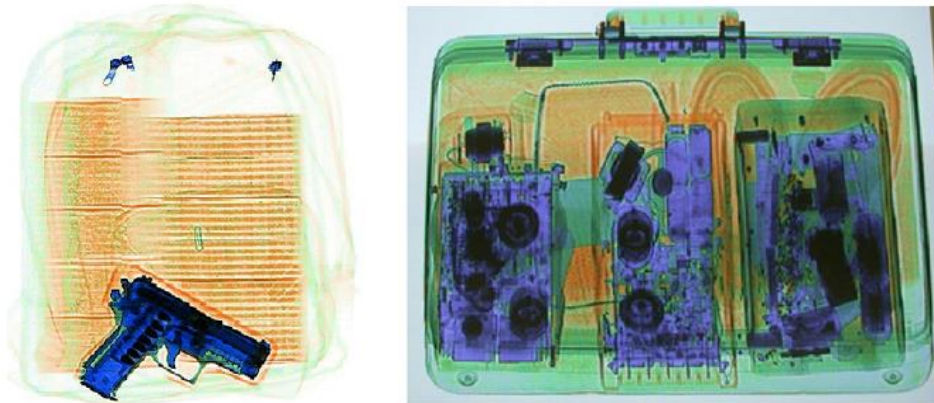
- Yes, when the operator supposes that a threat is present inside the baggage.
- No, when the operator supposes that a threat is not present inside the baggage.

Table 1.1 summarized the four possible outcomes:

*Table 1.1 Possible outcomes of a detection system*

<i>Decision</i>	<i>Threat present</i>	<i>Threat absent</i>
Yes	True Positive (TP)	False Positive (FP)
No	False Negative (FN)	True Negative (TN)

For taking a decision it is necessary to set a threshold at a certain signal strength. In this case signal is intended as an index of alarm that the operator can feel by observing the image of the baggage on the screen. If the signal is above the threshold, the operator blocks the baggage and addresses it to the second level inspection. Sometimes the image is misleading because it is not well defined. The following picture (Figure 1.1) depicts very well this fact. Two baggage are scanned with a dual energy system (dual energy system will be described in subsection 2.3.1). The left picture shows a clear image of a gun in a bag, which can be easily identified.



*Figure 1.1: Dual energy image of a pistol in a bag (left) and a lot of clutter in a baggage (right) [2]*

On the right, several objects are stocked together inside the baggage. This clutter defeats the object discrimination capability and some threats could not be visible [2]. In this case the operator is induced to consider a common object as a threat, sometimes only for a (justified) precaution. In the case of FP the second level inspection on the baggage is done which is actually not necessary. This is a waste of time for the operator and, from the psychological point of view, the baggage owner may feel unjustly accused.

On the other hand, the FNs are much more dangerous: in this case the threat passes the controls without being detected by the operator and the passenger's safety is lacking. Unclear images may be due to objects overlapping, objects clutter inside the baggage but also to intrinsic limitations of the detection system. If we assume that the signal produces a normal distribution of responses, the presence/absence of a particular threat or prohibited item might be expected to produce two Gaussian distributions (see Figure 1.2). The image quality of the system makes broader or narrower the distributions. Note that the threshold in the figure has been placed at the optimal value which minimized the FP and the FN but usually it is not the used one. This is true especially in airport security because a FN can lead to a catastrophic event and the probability of its occurrence must be as low as possible. Therefore, the threshold is shifted left such as the number of false alarms is increased while the probability of FN is minimized.

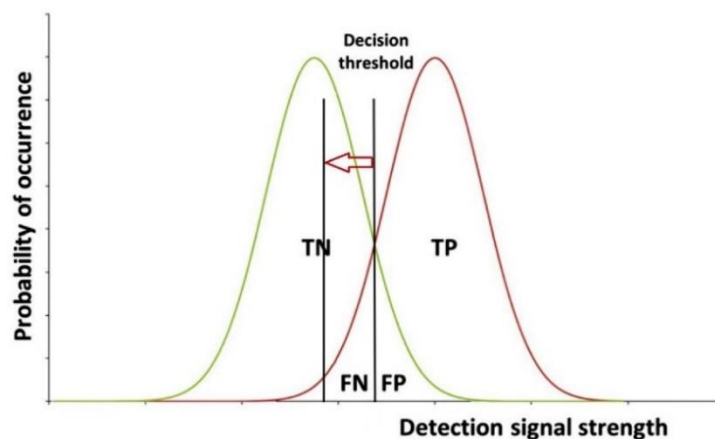


Figure 1.2: Associated distribution with respect to detection signal strength, example of threshold shift [1]

Scanning system must be able to screen at fast rate maintaining a low false alarm rate (FP) and enough high rate of detection (TP). To do that, it is important to improve the accuracy of the system which leads to narrow Full Width at Half Maximum (FWHM) of the Gaussian distribution of TN and TP and so a lower number of a false alarms.

When it comes to identify an object that is not explicit as it is in the left picture of Figure 1.1, the image quality plays a key role. The final image is created by a software that elaborates the signal coming from the primary X-Ray acquisition system. Therefore, the performance of the software strictly depends on the quality of the input signal. Optimizing the security detection system can be done working on the primary X-Ray acquisition system. This is exactly what this thesis work aims to make, focusing on the acquisition system of the FEP machines, the security scanner production line of Gilardoni Spa company.

## 1.2 X-Ray radiographic principles

The X-Ray imaging is based on the fact that X-Ray photons weakly interact with matter via electromagnetic force, thus providing a high penetrating capability. In Figure 1.3 is reported a simplified scheme of a standard projection radiography set up. An X-Ray tube is represented as the anode which emits X-Rays. The emitted photons are then filtered and collimated.

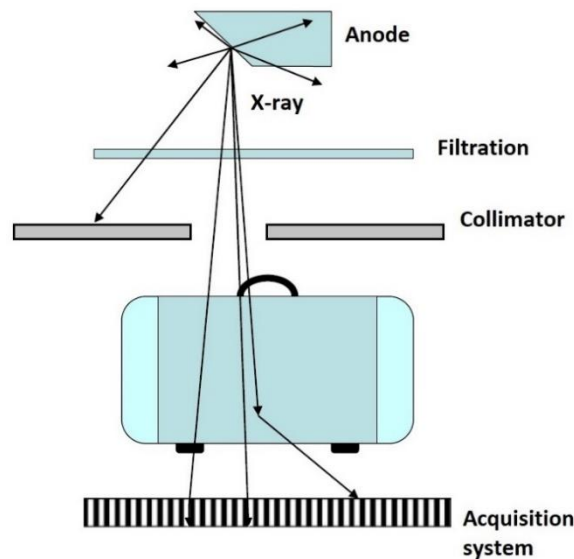


Figure 1.3: Schematic view of a baggage inspection system

Photons interact with matter through scattering, both elastic (Rayleigh) and inelastic (Compton), and absorption via photoelectric effect or pair production. The absorption mechanisms concur to a direct reduction of the photon flux while the Compton scattering reduce the photon energy and so increase the probability of the next interaction (lower energy leads to higher interaction probability).

In the simplest case we can consider a monoenergetic incident radiation field and a simple exponential law is valid, as follow:

$$I = I_0 e^{-\mu t} \quad (1.1)$$

$I_0$  is the incident photon intensity and  $I$  is the intensity transmitted through a medium of linear attenuation coefficient  $\mu$  and with thickness  $t$ . Equation (1.1) is called Lambert-Beer law and it is valid only if good geometry condition is respected during the experiment. In Figure 1.4 a configuration of good geometry is shown as well as a configuration where that constraint is not respected. In the latter case the detector also counts the scattered photons, and thus equation (1.1) is no more valid. Since the measure of  $I$  must collect only the primary radiation that does not interact with the matter, a collimators system is always employed.

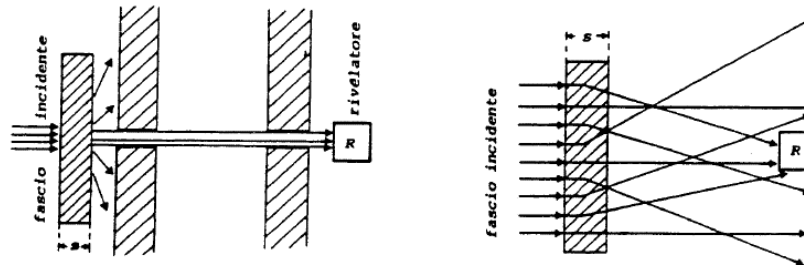


Figure 1.4: Example of good geometries (left) and bad geometry (right) configuration.

We can rewrite the equation (1.1) in terms of number of photons  $N$ , obtaining:

$$N = N_0 e^{-\frac{\mu}{\rho} \rho t} \quad (1.2)$$

where  $\mu/\rho$  is a new coefficient named *mass attenuation coefficient* which has the meaning of decreasing number of photon  $dN/N$  per unit path per unit density:

$$\frac{\mu}{\rho} = \frac{1}{\rho N} \frac{dN}{dl} \quad (1.3)$$

It is possible to express the mass attenuation coefficient as a series of coefficients each of them inherent to the specific interaction mechanism:

$$\frac{\mu}{\rho} = \frac{\tau}{\rho} + \frac{\sigma}{\rho} + \frac{\sigma_{coh}}{\rho} + \frac{k}{\rho} \quad (1.4)$$

These coefficients represent the probability of occurrence of the photoelectric effect ( $\tau$ ), Compton scattering ( $\sigma$ ), Rayleigh scattering ( $\sigma_{coh}$ ) and pair production ( $k$ ). In each case, these various processes involve interactions with the electrons in the medium of interest and hence the strength of interaction is dependent upon physical density as well as the electron density. We therefore expect a strong dependence to the atomic number ( $Z$ ) of the target material, which is indeed the number of electrons around the atom. The probability of occurrence of these processes has also a strong

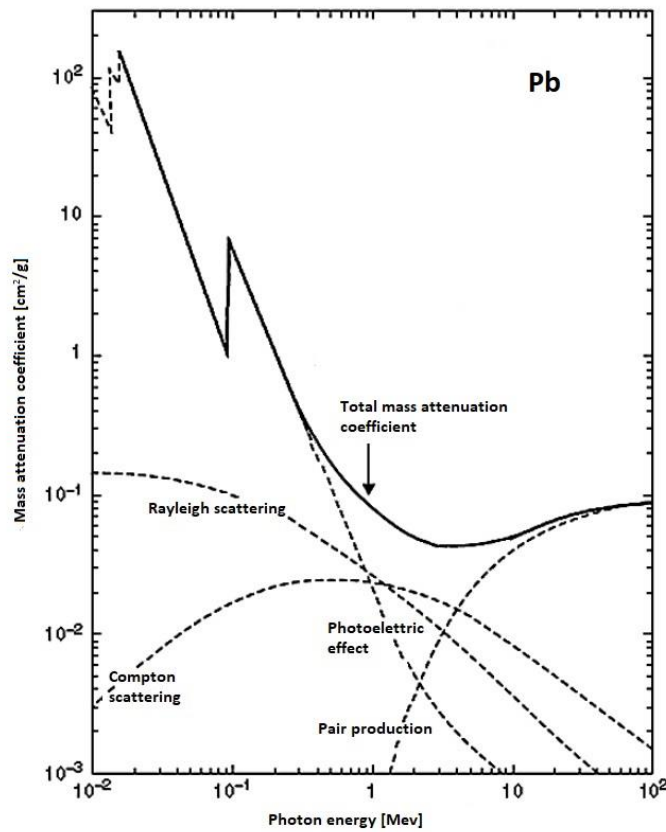


Figure 1.5: Pb attenuation coefficient for the photon interaction mechanisms

energy dependence as it is possible to see in Figure 1.5. This is an example of the different energy trends of the various photon interaction processes in Lead. In the low energy region Rayleigh scattering and the Photoelectric effect are dominant. The Rayleigh scattering does not involve any energy exchange and the only outcome is a change in the direction of the photon. For this reason, it is often neglected in the basic discussion of high energy photon interactions. At higher energies, the main process is the Compton scattering while for very high energy photons, above several MeV, the pair production process dominates.

In Table 1.2 the dependencies upon energy and atomic number are listed with an approximate energy ranges over which a given mechanism will dominate over the other.

Table 1.2 Photon interaction dependencies upon energy and atomic number [1,3].

<i>Interaction process</i>	<i>Variation with E</i>	<i>Variation with Z</i>	<i>Energy dominating range</i>
Rayleigh scattering	$\propto 1/E^2$	$\propto Z^2$	1-30 keV
Photoelectric effect	$\propto 1/E^{3.5}$	$\propto Z^{4-5}$	1-100 keV
Compton scattering	-	$\propto Z$	0.5-5 MeV
Pair production	$\propto E$ above the threshold energy (1.022 MeV)	$\propto Z^2$	> 5MeV

For a multi-element compound the resultant mass attenuation coefficient is given by:

$$\frac{\mu}{\rho} = w_1 \frac{\mu_1}{\rho_1} + w_2 \frac{\mu_2}{\rho_2} + \dots \quad (1.5)$$

where  $w_1, w_2$ , etc. are the weight fraction of the element 1,2, etc.

X-Ray inspection systems display grey scale images representing variations in the shape, thickness and composition of an object reflected in the attenuation coefficient. The so-called *contrast variations in a transmission image* represents the relative change in attenuation between one part of the medium and another. Thick, high density and high Z objects produce greater reduction in the photon flux than thin, low density and low Z objects. As such, it is possible to measure these features within certain detection limits and to develop correlations that reflect the decision threshold. Strictly speaking, these systems are not explosive detection systems because the image just shows the degree of absorption of the X-Rays. Anyway, they can reveal the presence of dangerous devices by directly showing the threat, like in Figure 1.1, or by showing fuzes, wires etc. [1].

### 1.3 Gilardoni X-Ray industry

Gilardoni Spa is a scientific industry founded in 1947 by Arturo Gilardoni in Mandello del Lario (Lc), Italy. It is an important manufacturer of scanning inspection systems recognized all over the world. Initially Gilardoni was a research and production laboratory for X-Ray tubes, but in the following the company started investing in the field of medical devices and security machines. One of the key developments is the L-configuration acquisition system that is mounted on Gilardoni's scanners.



Figure 1.6: Gilardoni Spa company [4]

Nowadays the company provides a wide range of products. It is internally divided in three departments [4]:

- [Medical division](#) (diagnostic radiology, angiography, mobile surgical units, emergency radiographic system, X-Ray irradiation systems).

- [Security department](#) (X-Ray system for baggage control and body scanners both for airport and other anti-terrorism sectors).
- [Non-destructive testing](#) division “NDT” (quality control systems using X-Ray and ultrasonic technologies for automotive, aerospace, and railway industries as well as for steel and light alloys production, and in the food sector).

This thesis work was carried out in the R&D Security department. In particular it is focused on the acquisition system mounted in the FEP machine line. In Figure 1.7 FEP ME 536 is shown as an example. The operation principle of the



Figure 1.7: FEP ME 536 device [4]

system is very simple: the baggage enters the machine thanks to a roller table and it is scanned by X-Rays during the movement toward the exit side. The machine has a mechanical and electronic apparatus for transport control of the baggage but this part of device, which is also very important, is not our business. The X-Ray scanning system is composed by:

- An X-Ray generator produced by Gilardoni called *AION monoblock*
- An X-Ray acquisition system

## 2 X-Ray scanning systems

The X-Ray scanning systems for baggage inspection are made by two main components, the X-Ray source and the acquisition system. This chapter is aimed at describing in details their working principle.

### 2.1 X-Ray source

In X-Ray scanning systems the radiation source is very important. The key requirement is that some photons must be blocked by the object under inspection while other photons must be allowed to pass for generating the transmitted image. The photon transmission capability or, conversely, the photon interaction probability, strictly depends on its energy. This was already reported in Figure 1.5. It is desirable to calibrate photon energies in order to satisfy the above-mentioned requirements for different applications (i.e. hand baggage, hold baggage, cargo scanner, etc.). The X-Ray tube is particularly suitable to do that by changing the kV parameter. While modifying the mA parameter, it is also possible to change the photon flux of the source (see section 2.1.3). Furthermore, the X-Ray tube is an ON-OFF photon source making its handling much easier than a radioactive source. For all these reasons the chosen photons source for our field of application is the X-Ray tube. In this section we will describe the physical principle of photon generation through the Bremsstrahlung process, the output photon energy spectrum and then the design and construction of an X-Ray tubes. Finally, the Gilardoni AION system will be detailed.

#### 2.1.1 X-Ray tube: photon generation principle

When a high energy electron enters in a target material, it can lose energy by radiative processes as well as by Coulomb/collisional interactions. Energy losses by Coulomb interactions do not generate photons and they are not considered in our discussion. The radiative emissions are due to two key processes: the braking of high-energy electrons (Bremsstrahlung) and the atomic transitions of the target nuclei (characteristic radiation). These processes are performed inside an X-Ray tube in a controlled manner. The radiative process takes the form of Bremsstrahlung photons along the electron track. From classical theory, any charged particle must irradiate energy when accelerated or decelerated: penetrating a material, electrons pass close to the atoms and can be deflected and slowed down by the attractive force

of the nuclei. The energy loss during this path appears in the form of an X-Ray. The *linear specific energy loss* through this radiative process is [3]:

$$-\left(\frac{dE}{dx}\right)_r = \frac{NEZ(Z+1)e^4}{137m_0^2c^4} \left(4 \ln \frac{2E}{m_0c^2} - \frac{4}{3}\right) \quad (2.1)$$

where  $m_0$  is the particle mass,  $N$  atomic density,  $E$  particle energy,  $Z$  atomic number of the target material. We see that  $m_0^2$  is present at the denominator and this leads to a low yield for heavy charged particles and a high yield for light charged particles, like electrons. The factor  $E$  at numerator indicates that radiative losses are more important for high particle energies and the factor  $Z^2$  shows that absorber materials of high  $Z$  are more likely to lose energy through radiative channel. Hence, the choice high  $Z$  elements - like Tungsten or Molybdenum - as target materials is the most appropriate choice. The ratio between radiative and collisional losses can be expressed with the following empirical formula:

$$\frac{(dE/dx)_r}{(dE/dx)_c} \approx \frac{EZ}{700} \quad (2.2)$$

where the energy  $E$  is in units of MeV. In our case typical energies are around one hundred of keV, so the fraction of energy losses due to radiation is small compared to those due to ionization and excitation of the target atoms. This is the reason of the heating of the target material [3].

### 2.1.2 Energy spectrum generated by the X-Ray tube

The X-Ray spectrum can be divided in two portions that have different physical origin: the continuous part of the spectrum and the characteristic spectrum. The two processes are schematically shown in Figure 2.1. An electron which strikes within the target experiences some braking actions and produces X-Ray photons.

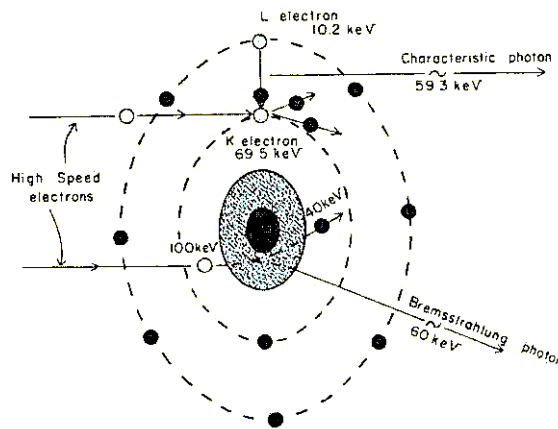


Figure 2.1: Radiative losses process, energy referred to Tungsten atom [9]

The energy spectrum deriving from the Bremsstrahlung process is a continuum: the photons continuously assume all possible energy values from zero to the electron kinetic energy. If a collision occurs near to the target atoms nucleus, the electrons are exposed to the greatest force and thus they lose most of their energy generating high energy photons. Vice versa, the electrons colliding in the outer zones of the atom undergo to a weaker interaction and lower energy photons are emitted. The Coulomb force decreases follow the inverse of the square distance from the nucleus. The result is a narrower area of high electric field (inner shells) and a larger area of low electric field (outer shells). The probability of interaction in the inner or outer shell is proportional to their area. Therefore, the electron has higher probability to interact in the outer shell where the field is low. This leads to higher production yield for low energy photons. This is reflected on the spectrum where the higher number of photons is produced at low energies. In the absence of a filter, the relationship between the number of photons produced and the energy is decreasing in linear way. On the other hand, in the presence of filtration such as the anode surface, the X-Ray tube window or added filter material, a significant number of low-energy photons are absorbed: the result is a distribution whose peak varies from 1/3 to 1/2 of the maximum energy value.

This continuous spectrum overlaps with single energy lines. Those lines are the *Characteristic radiation* of the atoms of the medium. They are produced when an incoming electron has enough kinetic energy (greater than the binding energy) to remove an electron from the target atom. Afterwards the orbital electron is removed, it leaves a vacancy that is filled by an electron coming from a higher energy level. As the filling electron moves down to fill the vacancy, it releases energy by emitting an X-Ray photon. This is known as characteristic radiation because the energy of the photon is characteristic of the chemical element of the material. In Figure 2.2 is reported a scheme of the X-Ray output spectrum produced by an X-Ray tube with

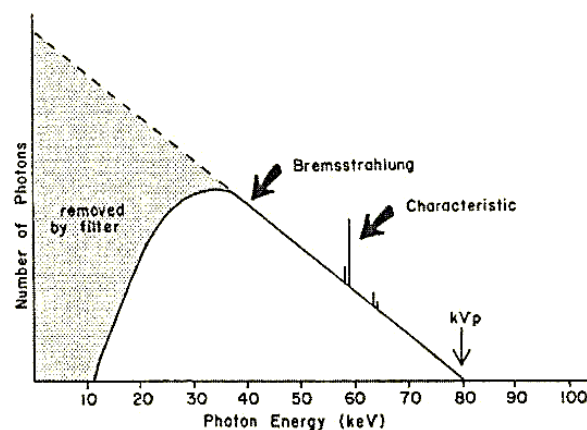


Figure 2.2: X-Ray spectrum scheme of X-Ray tube with Tungsten target [9]

Tungsten target working at 80 kV. It is possible to see that an important portion of the spectrum at low energy is removed by the filter while the end of the spectrum is

set to 80 keV which is the maximum energy that an electron can gain from the acceleration system (see section 2.1.3). The characteristic lines are the lines of K-alpha 1,2 and K-beta 1,2 of Tungsten. These lines are respectively around 59 keV and 67 keV.

### 2.1.3 Structure of an X-Ray tube

The X-Ray tube consists of a glass envelope containing two electrodes facing each other called *cathode* (negative electrode with one or two Tungsten filaments) and *anode* (positive electrode usually made of Molybdenum or Tungsten). Vacuum is created in the glass ampoule so that electrons can move from a cathode to an anode without encountering any obstacles in their path. Normally, the tube is controlled by a direct voltage and the electrons reaching the anode have different energies depending on the voltage value applied between the anode and the cathode (kV parameter). The electrons are generated by thermoelectric effect from the

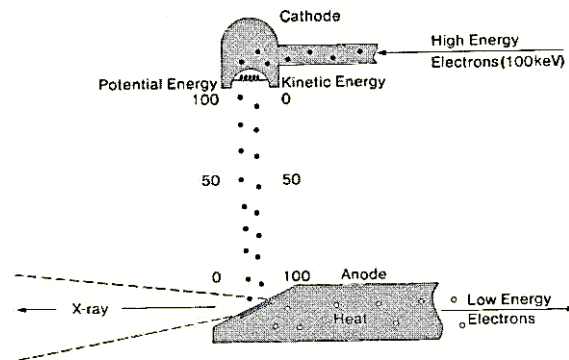


Figure 2.3: Energy Exchange within an X-Ray Tube [9]

filament, that is heated by the passage of the current (parameter mA). The purpose of the anode is to constitute a target against which electrons can impact and produce X-Rays. A schematic of the process is shown in Figure 2.3. Only 1% of the energy of the electron beam that collides into the anode is converted into X-Rays, while the remaining 99% is transformed into thermal energy, which causes heating of the material [5].

The choice of the anode material is made among elements having high atomic weight and high melting point. Tungsten is the most used material. The anode must therefore be manufactured to be able to get rid of a large amount of thermal energy as quickly as possible. Usually, the anode consists of a large copper cylinder with a plate of Tungsten on which the focal point is formed. The melting point of the Tungsten is 3400°C, therefore it is possible to withstand high thermal loads concentrated at focal point of a few mm<sup>2</sup> without causing significant material damage.

An example of a Coolidge X-Ray tube is reported in Figure 2.4 in which it is possible to see the long copper anode used for heat extraction: the heat diffuses from the focal spot through the Tungsten plate, and from there to the copper block that brings it out of the tube. Depending on the X-Ray tube power, the focus, which is usually square in size, has a side of about 0.3 mm in microfocus tubes, up to 4-5 mm in those of high power [5].

A solution to the power limit due to the limit in heat exchange is the rotating anode tube. In this case, the anode consists of a Tungsten rotating disk which is rapidly rotated in front of the electron beams. The heat is therefore spread over a large surface while the focus still has small dimensions. The rotation speed is around 3000 rpm, the anode disk becomes incandescent at significant thermal loads and the heat is dissipated outside by radiation through the glass walls of the tube [5].



Figure 2.4: Coolidge X-Ray tube at Gilardoni museum

#### 2.1.4 AION monoblock: Gilardoni's X-Ray generator

AION is a collection of X-Ray generators designed by Gilardoni Spa and applied to different security systems of their products line. Such modules have a solid structure in which the X-Ray tube and the cooling system are placed. The power supply is provided by a highly stabilized generator giving rise to an accelerating potential and variable current. The choice of these parameters is suited to have the best image quality for the different applications.

The X-Ray tube is enclosed in an envelope of borosilicate glass in which void is created. The cathode is a Tungsten filament and a high voltage is applied from cathode to anode with different values depending on the application: higher for cargo application and lower for luggage screening. The anode is composed of Tungsten material. Around the glass structure a cooling system is placed: this is a layer of circulating oil which removes heat from the X-Ray tube to maintain stable performances during the operating time and avoid some possible power load damage

to the envelope and the anode. The system is enclosed in a lead shield that is thick enough to reduce the escape of X-Ray not belonging to the beam. The exit window is made of plastic material (PBT Polybutylene terephthalate) and it shapes the beam like a fan. No added filtration is present, because a rather high fluence is required for attenuation measurements.

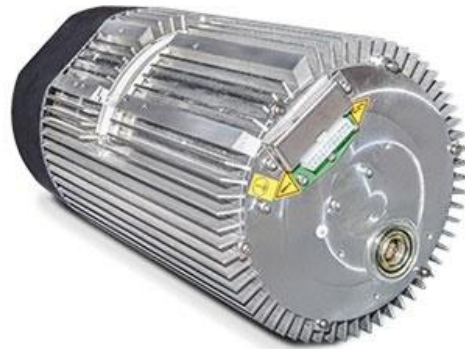


Figure 2.5: Gilardoni Spa AION monoblock [4]

## 2.2 X-Ray scanning system detector

In general, radiation detectors can work in two different operation modes, photon-counting and energy-resolving. The photon-counting detector integrates the photons of all energy bands of the beam that strike its surface. The energy-resolving detector has specified number of energy bins in which the number of photons are recorded according to their energy deposition in the sensitive volume. Here, each radiation signal is processed event-by-event (pulse mode) and fast timing is important. In contrast, the photon-counting detectors, integrate multiple events over typically few ms (current mode) and the fast timing is less critical.

Basing on the detector structure, it is possible to make another distinction: “one step” detectors, which directly convert X-photons into an electric signal, and “two steps” detectors, which exploits the indirect conversion of radiation into visible light which is then converted into an electric signal with a photocathode

This work will explain in detail only the indirect conversion/two steps configuration because it is the system mounted on Gilardoni FEP machines.

### 2.2.1 General working principle

The full X-Ray detector is an array of many closely spaced detector channels. The relative low space available between one and the next makes impractical the use of Photo Multipliers Tubes (PMTs) with their associated high-voltage power supplies. As a result, photodiode-scintillator arrays are typically used to convert the scintillator light into an electrical signal. Scintillators serve as the primary X-Ray sensors and must be thick enough to efficiently stop  $>95\%$  of the incident X-Ray flux [5].

The detection process can be divided in three steps described in Figure 2.6:

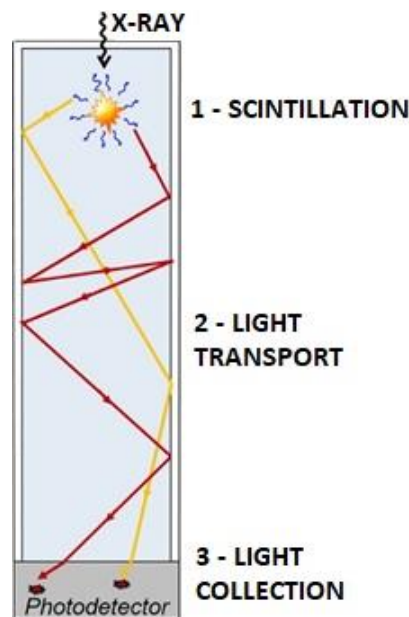


Figure 2.6: Three main step occurring inside the X-Ray detector [2]

1. The scintillator stops the incident high energy photon and produces visible light by scintillation, generally in a ns time scale. Photoelectric absorption is generally the main process required for analyzing radiation: in this process one photon is absorbed and one electron is generated with the same energy. This primary electron, in turn, can generate many excited secondary electrons via Coulomb scattering, which in turn may induce the scintillation (see section 2.2.2) [6].
2. The emitted visible light intensity is proportional to the energy deposited by the secondary electrons created by the incident ionizing radiation. The scintillation light is then transported inside the crystal toward the photodetector placed below it. The scintillator might be covered with a reflective material to enhance the light transport efficiency.
3. Light is collected and converted into an electrical signal by the photodetector.

The amplitude of the electrical signal is proportional to the amount of visible light and, therefore, to the energy deposited by the incident X-Ray photons. Optimizing the scintillation process, the optical transport and the light collection are all essential aspects of the detector design [7].

The scintillation process depends on the intrinsic properties of the scintillator but also on external factors including temperature, host defects,

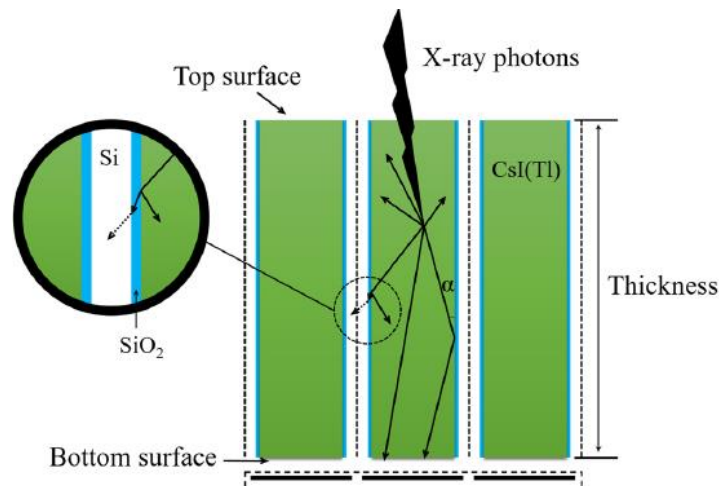


Figure 2.7: Operation principle of reflector material [18]

annealing, etc. Light transport is determined both by intrinsic optical properties and surface reflectance properties. It is common to have a reflecting layer like  $SiO_2$  or  $TiO_2$  inserted between two channels in order to increase the light collection capability. Reflectors act as light guides which direct the scintillator light to the photocathode surface. They are very important especially for scintillator geometries with high thickness to width ratios where internal light trapping and self-absorption can result in diminished detection efficiency. Moreover, the presence of the reflective material limits the light crosstalk between channels, thus optimizing the spatial resolution of the whole device, as shown in Figure 2.7.

Once light reaches the photodetector, it is converted into photoelectrons with a characteristic efficiency of the photodetector employed and of the geometrical arrangement. The crystal-photodetector optical coupling plays an important role for the detection efficiency. Various coupling strategies have been developed, but the most commonly used strategy is the direct coupling using optical glues (see subsection 2.2.4.1). In the next section we will focus on the physical principle of scintillators and photodetectors.

### 2.2.2 Scintillators

As already mentioned in section 1.2, interactions of X-Rays with matter mainly include three processes: Photoelectric, Compton and pair production. In order to maximize the interaction probabilities, scintillator materials are required to have a high density and  $Z$ . This is satisfied by solid state inorganic scintillators, which, for this reason, are the primary radiation sensors in many X-Ray applications. As hinted in 2.2.1, the aim of the scintillator is to convert high energy radiation into visible light.

In solid state inorganic scintillators, the luminescence arises from the energy states determined by the crystal lattice of the material. As shown in Figure 2.8, inorganic scintillators are insulators having a wide band gap between their valence and conduction bands. The lower band represents those electrons that are essentially bound at lattice sites, while the upper band represents those electrons that have enough energy to move throughout the crystal. Within this gap they also have the luminescence centers, which play a central role in producing the scintillation light. When a photon interacts with the scintillator it delivers energy to an electron

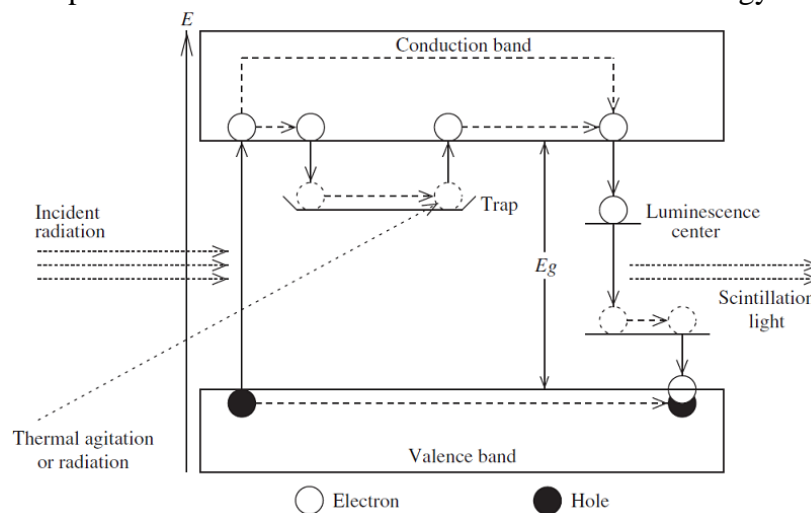


Figure 2.8: Principle of scintillator mechanism in inorganic scintillators [15]

called *primary electron*. If the transmitted energy is greater than the band gap of the material, the electron jumps up to the conduction band and leaves a hole in the valence band. Both the electron and the hole created are then free to move around the crystal. The electron can hit other electrons belonging to lattice atoms and excite them to the conduction band. Such electrons, not primary excited by radiation, are called *secondary electrons*. If the total deposited energy  $E$  is equal to 1 MeV, the number of secondary electrons is around  $10^5$  inside a volume of  $100\text{nm}^3$  [6]. We want to underline that in the literature there is not a universal definition of scintillation but essentially it follows the same process of photoluminescence (PL). The important aspect is the generation of multiple secondary electrons or not: in PL, the excitation

occurs for one electron per process while in scintillation it occurs for many electrons. It is possible to fix an excitation energy threshold of 0.1 keV between PL and scintillation [6].

In pure crystals, the de-excitation of an electron to the valence band with photon emission is an inefficient process due to self-absorption. Furthermore, the large band-gap of the material may result in a photon emission below the visible spectrum. Many materials do not provide an efficient scintillation mechanism and, to perform efficiently, they must be activated. Activate a crystal means introducing specific impurities with the aim of creating special sites in the lattice and modify the band structure. As a result, there will be new energy states, called luminescence centers, inside the gap [3].

If an electron jumps from the higher energy level of this center to the lower level a scintillation photon can be emitted. This process is not the only way for electron de-excitation and the occurrence of non-radiative process is also possible. In this case the energy is dissipated by heat carrying particles called phonons. If this happens, the radiative process is said to have been quenched and no visible photons are emitted [8].

There is also another possibility: an electron can jump to the so-called electron trap. These traps are metastable energy states that are formed by impurities and defects (in the case of crystalline scintillators). An electron trapped there can remain there for an extended period of time, which can be as long as an hour or more and as short as a few nanoseconds [8]. Such states require an additional amount of energy for jumping back to the conduction band from which de-excitation to the ground state is possible. One source of this energy is thermal excitation and the resulting light output is called phosphorescence or “Afterglow” which can be a significant source of background light in scintillators. Therefore, in scintillator materials, the secondary electrons are desired to reach the luminescence centers as much as possible. For this reason, the concentration of activators is very important and must be controlled carefully during the scintillator production process. For example, a parameter like the spatial scale of the dispersion of secondary electrons, which is around 100 nm, have to be considered. The concentration should ensure that the distance between activators inside the crystal lattice is shorter than 100nm [6]. The choice of the activator specie and its concentration is therefore very important because it directly affects the light output yield and the emission spectrum.

The proper choice of a scintillator depends on the application. For example, NaI(Tl), CsI(Tl) and CdWO<sub>4</sub> single crystals are used in applications where a high stopping power is required. An example is the gamma camera, the X-Ray detectors in computed tomography (CT), but also the detector used in security and baggage inspection.

### 2.2.3 Photodiode

The photodiodes used in the FEP detectors are usually the PIN photodiodes. A PIN is a diode with a wide, undoped, intrinsic semi-conductor region between a p-type region and an n-type region. Such devices have no internal gain and operate by directly converting optical photons into electron-hole pairs that are collected by an acquisition circuit. Visible scintillation photons carry about 3-4eV which is enough to create an electron-hole pair in a semiconductor material with a typical bandgap of 1-2eV. A common configuration for a PIN diode is reported in Figure 2.9.

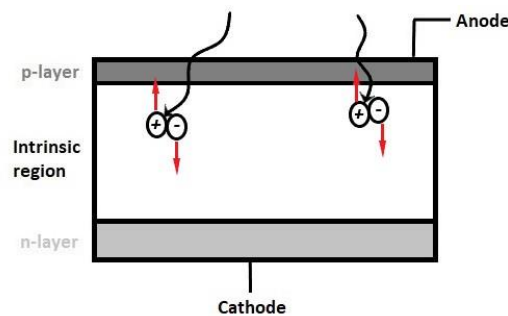


Figure 2.9: PIN photodiode, principle of operation

Light is incident on a p-layer entrance window which must be as thin as possible to enhance transmission of the light to the active volume of silicon (intrinsic region). After the pairs are produced by the visible light, they are collected at the anode (hole) and at the cathode (electron) and the corresponding induced charge is processed in an attached preamplifier to produce the output signal pulse. In a typical scintillation event, only few thousands visible photons are produced so the output signal amplitude is small. However, because of the high X-Ray fluence rate of screening luggage system no further primary amplification is required [9].

The parameter that characterizes this detector component is the *Quantum efficiency*, which is defined as:

$$QE = \frac{n^0 \text{ PHOTONELECTRONS}}{n^0 \text{ INCIDENT PHOTONS}} \quad (2.3)$$

In Figure 2.10 is reported the Q.E. of a PMT photocathode and of a PIN photodiode. The Q.E. of the PIN diode can be as high as 60-80% because is not limited by the need for charge carrier to escape from the photocathode surface as in the case of PMTs. The Q.E. of any photocathode depends strongly on the wavelength of the incident light and the material of the device. In particular PIN photodiodes are most sensitive from 500 to 1000 nm, amorphous silicon peaks near 550 nm while PMTs have high spectral sensitivity from 300 to 600 nm.

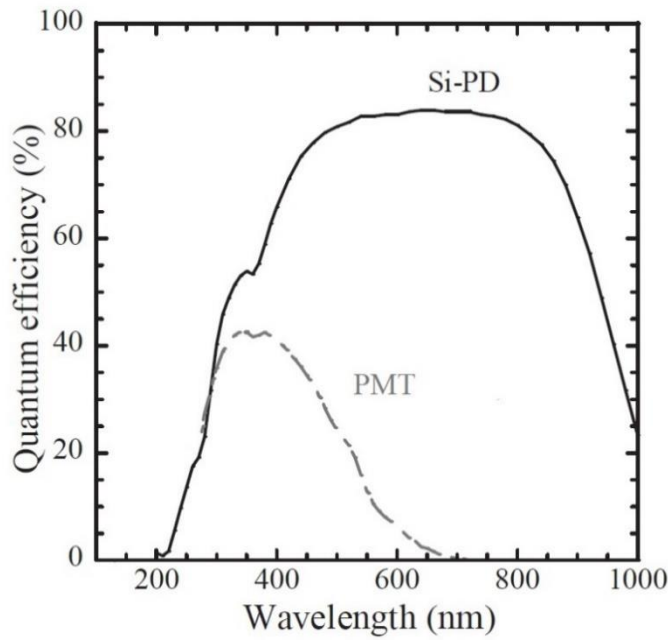


Figure 2.10: Quantum efficiency of PMT photocathode compared to Si-PD [10]

## 2.2.4 Detector efficiency optimization

### 2.2.4.1 Coupling

For an X-Ray detection system that uses scintillators, the detector efficiency is affected by the coupling of the scintillator to the photodiode. The light must pass through the surface between scintillator and photodiode and it is refracted in a different way depending on the indexes of refraction. Usually, scintillators have high indices of refraction (typical 1.7–2.3) and the best solution to obtain a good coupling is the use of an optical coupler with a refraction index halfway between scintillator and photodiode[10].

A practical example, which consider a system very similar to that mounted on Gilardoni FEP devices was reported by *Jin Hyoung Bai et al.* [11]. A photodiode covered by an outer anti-reflective coating with an index of refraction of 2.02 has to be efficiently coupled with a CsI(Tl) scintillator that has a refractive index equal to 1.78. A bonding optical adhesive was used to fill the space between the two components. The best coupling is reached with an optical grease having an index of refraction equal to the *geometric mean* of the two adjoining materials:

$$n_{opt} = \frac{n_1 \times n_2}{2} \quad (2.4)$$

In that example, an optical grease with a refraction index near to 1.82 was chosen.

### 2.2.4.2 Matching

The wavelength at which the scintillator emits also influences the efficiency of the detection system. Different light detection systems have high quantum efficiency over different portion of the visible spectrum until the near-IR. Matching the scintillator emission wavelength to the efficiency peak of a light detection system can be accomplished by choosing scintillators with an emission peak near the desired wavelength. This is taken in consideration in this work using a MATLAB code which is discussed in detail in 4.2.

## 2.3 Image acquisition system

Different methods can be used for capturing the attenuation picture. In radiography, which is the simplest case, the image is formed in a receptor. For example, a flat panel composed by many small detectors is positioned in front of the source with the object in between them. In this case the formed image represents the projection of the object on the panel plane. If the object is represented by a function  $f(x, y, z)$  the projected image  $p(x, y)$  is simply:

$$p(x, y) = \int_0^t f(x, y, z) dz \quad (2.5)$$

where  $t$  is the thickness of the object. So, the  $x$  and  $y$  coordinates are retained but the  $z$  coordinate is lost.

The next step of the evolution of these devices is the CT (computer tomography): this system uses a pencil beam which passes through the object. The X-Ray source is made to be rotated around the object. The signal is collected using digital X-Ray detector above which a collimator is mounted. The aim of the collimator is to align the X-Ray source and the detector to produce cross-sectional images of the baggage. These slices are called *tomographic images* and they can be digitally stacked together to form a three-dimensional image for an easier identification of possible threats inside the baggage.

The system installed on the FEP machine produce by Gilardoni Spa industry is quite different. A schematic view of the device is shown in Figure 2.11. We have already described the acquisition system and now we can focus on how the radiographic imaging chain works. The main four components are: the objects, the X-Ray source, the mechanic apparatus which move the baggage at an appropriate speed and the acquisition system. The AION monoblock is placed down on one side of the system while on the other side two array detectors are mounted. X-Ray

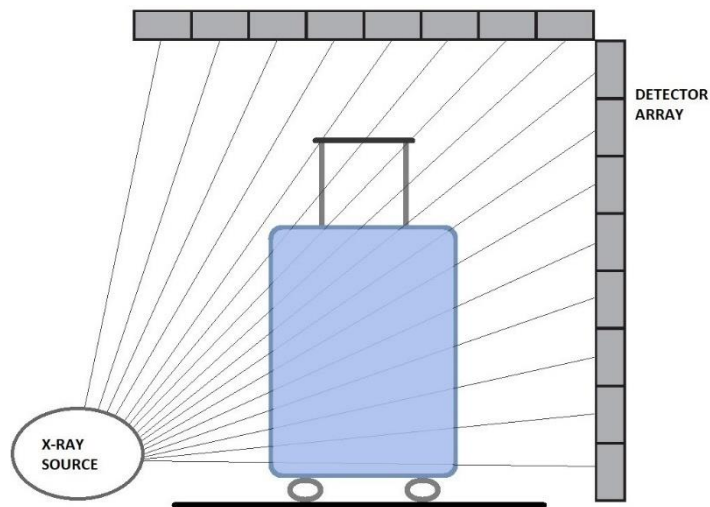


Figure 2.11: A schematic view of the X-Ray scanning system installed in FEP machine

projections are made by measuring the number of X-Ray photons transmitted through the objects and recorded at the detector side. The baggage is placed on a roller table that slides during the irradiation in order to get different sliced images of the baggage. The final result is the complete scan of the object which is elaborated from a software to obtain the final image. The X-Rays energy ranges from 10 to 150 keV for the baggage screening. The radiation detector is almost the most crucial step of the acquisition chain.

### 2.3.1 Single energy systems and double energy systems

Single-energy imagers are the simplest kind of X-Ray detectors and they were already described in section 2.2. They integrate the light coming from the impact of X-Ray photons in the scintillator during an integration time interval but do not provide any information about the energy of the impinging photons. These systems are nowadays widely used as cargo and vehicle screening systems.

As the X-Ray attenuation coefficients of materials in the objects are energy-dependent, additional material information can be acquired from spectral measurements. An innovative system was developed for the first time in a new generation CT scanner for medical imaging. These devices are called DECT (Dual Energy CT) and they are able to provide a gross information about the low energy and the high energy regions of the impinging X-Ray spectrum[12].

Two basic types of dual-energy systems are utilized: single broadband X-Ray beam and dual detector arrangement. The most Gilardoni's products is based on two-layer or "sandwich" detectors where different spectral sensitivities are used to

provide spectral information. X-Ray data are recorded by the two scintillator and two independent images are computer-processed to compare low-energy and high-energy X-Rays. The final image shows the shape of the object with a color scale generated by the software. The colors of the reconstructed image correspond to obtained gross information about the  $Z_{\text{eff}}$  on the measured sample. The improvement stays in the fact that the  $Z_{\text{eff}}$  of the material is identified with more precision thanks to the energy information.

An example of material decomposition through energy-selective CT was reported by *E. Shefer et al.* [13]. A Philips Healthcare team proposed a configuration depicted in Figure 2.12: two attached scintillator layers, optically separated, and read by a side-looking silicon photodiode.

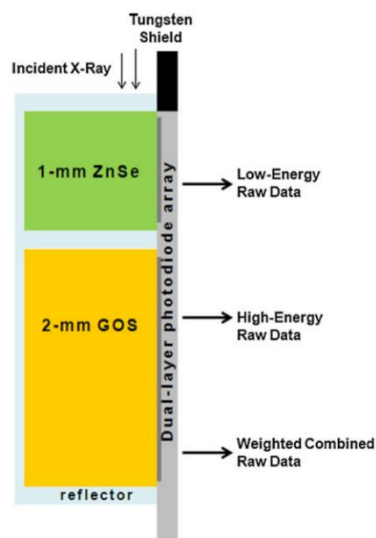


Figure 2.12: Schematic view of Philips dual layer detector

The use of edge-on photodiodes between the detector columns prevents also optical Crosstalk between near channels. The thickness of the ZnSe and GOS scintillators

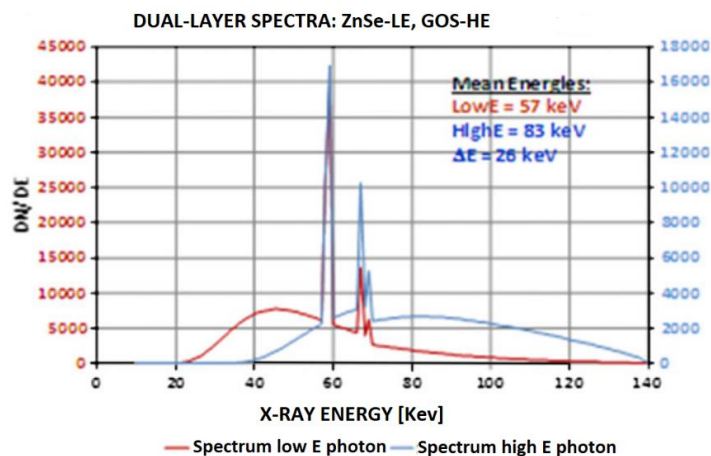


Figure 2.13: Energy deposition spectra in each scintillators, dual energy system [13]

have been optimized to maximize the deposited energy separation between them. The spectral deposited energy at 140kV for the low energy scintillator (red) and for the high energy one (blue) is shown in Figure 2.13.

An interesting DECT application is shown in Figure 2.14. Images of Conventional CT (left side in the figure) and DECT (right side) show the advantage in stone identification. For this reason, DECT is an important tool for urinary calculi imaging due to the high sensitivity of detecting stones and differentiating uric-acid (UA, dissolution therapy) and non-UA (surgical procedure) stones[14].

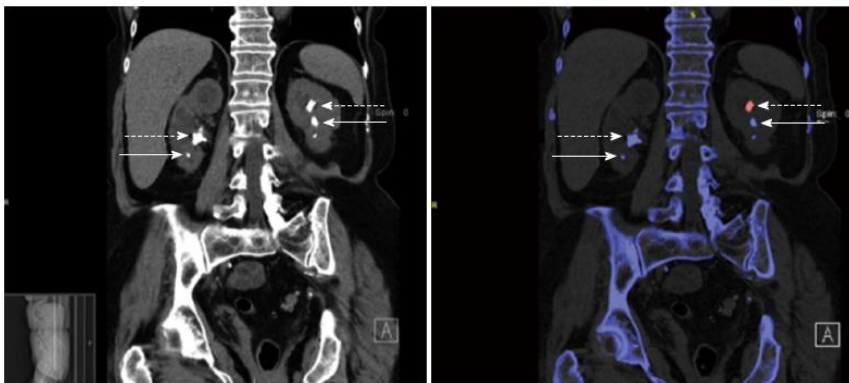


Figure 2.14: Conventional and dual-energy computed tomography images: the solid and dashed arrows point to stones and stents [14]

Soon the dual energy technology was employed also for baggage security applications. It makes possible the material classification into three categories: inorganic, organic and mixed. The result is an exceptional ability to detect and discriminate a wide variety of threat materials, providing enhanced overall security. Especially, organic materials, usually associated with dangerous compounds, mainly plastic explosives, are easier to achieve with dual-energy, as opposed to single-energy systems.

One of the key motivations in technological developments is to eliminate the ban on carrying liquid that is currently in place. Once this ban is eliminated (already legislated in Europe), the airport operators will be forced to use better technology for liquid security detection [15]. Gilardoni Spa has already developed products based on a dual energy detector. The dual energy high-quality color images have dramatically reduced the need for re-scans of baggage. The next figure is an example of scan captured by the FEP ME 640 AMX and the improvement is clearly visible. Furthermore, the superior capability of a dual energy system to distinguish organic material from inorganic materials make possible the development of a dedicated software able to automatically reveal some threat items [4].



Figure 2.15: Gilardoni's FEP ME 640 AMX baggage pictures, from below and from lateral side. Colors and B/W [4]



## 3 Scintillators review

Scintillators are commonly used in today's radiation detectors for medical diagnostics, industrial inspection, dosimetry, nuclear medicine, and high-energy physics [10]. In each application the scintillator is the primary radiation sensor: as explained in 2.2, it is a material that absorbs high-energy photons and then emits visible light. When our research began on this component, the aim was to evaluate the presence in the global market of a suitable, high performing scintillator which meets the needs of the Gilardoni's FEP production line. In this thesis work, the performances are evaluated for the single energy FEP systems. If a positive feedback returns, the research could be carried out for a future dual energy application. Our literature review starts firstly focusing on scintillators used in applications like security inspection and similar field like medical diagnostics. FEP machines source is an AION monoblock X-Ray tube which works at 150kV. Computed Tomography (CT) system exploit photons ranging from 80 keV and 140 keV which is very similar to our range of energy [16].

In the following, an introduction to scintillator science will be presented with a brief outline on the historical development and production process. A list of the most important scintillator features will be reported in section 3.3 with some examples of improvement based on the production method. The 3.4 section of this chapter will be a description of the most commonly used scintillators and, at the end, our candidate scintillator will be presented.

### 3.1 Historical development

Phosphor powders were the first category of scintillators exploited in the past. They were introduced in practice very soon, in the mid of 1940s. ZnS phosphor was used by Ernest Rutherford in the early years of nuclear physics as a scintillation detector. Up to the present-day phosphor powders can be found in a limited number of applications. In the late forties the first single crystal scintillators, NaI(Tl) and CsI(Tl), appeared and became widely used. Due to their low production cost and high overall efficiency they are still widely used nowadays.

In the following decades, some other materials were developed but the evolution was relatively slow. The world of inorganic scintillators has undergone a renaissance that began in the mid-1980s. From that year a lot of scintillators were growth with the Czochralski method, by which large size single crystals were produced. Stimulated by the discovery of new materials having excellent light yields

and/or fast decay times, many potential scintillator materials have undergone testing and evaluation in laboratories all around the world. At that time, the primary aim of the research was to improve the overall efficiency trying to get the best crystalline structure and the best combination of dopants. Instead, starting from the nineties, the researcher began to develop scintillator improving a specific feature. That was for answering to the very different requirements coming from the multiple fields of applications. Different scintillators in single crystal form appeared with improving timing feature, BGO and the class of Rare earth Oxyorthosilicate are examples. They were developed for timing coincident applications (i.e. PET, Positron Emission Tomography) that required a fast response. At the end of 20<sup>th</sup> century the research extended to new materials starting from Aluminium perovskite compounds to garnet material and Lanthanum halides.

Nowadays a latest class of materials appears in the global market, the ceramic scintillators. Thanks to an appropriate recently developed production technology, ceramic materials obtain competitive optical properties and become a new trend. In Figure 3.1 a list of most widely used scintillators is reported with the corresponding year of introduction.

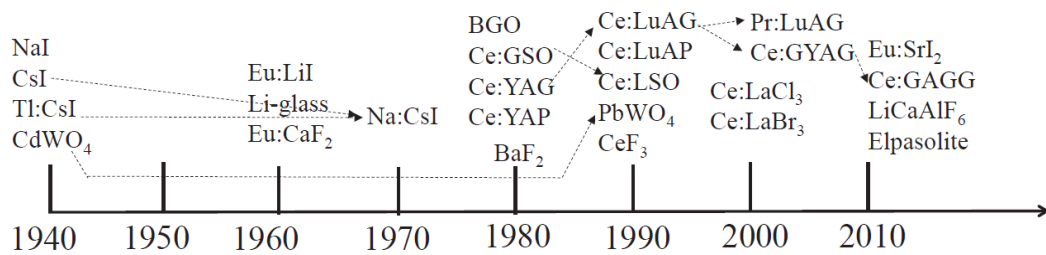


Figure 3.1: Scintillator evolution [6]

## 3.2 Scintillators production

Many crystal scintillators are grown with techniques like the Bridgman or Czochralski methods. These are melt-based methods, in which the mixture of starting materials is brought over their melting temperature. The crystal is produced either by pulling it from the melt (Czochralski) or slowly cooling the melt (Bridgman). The most common method is the Czochralski process which was already used by semiconductor material designed to electronic application. The process phases are shown in Figure 3.2. The crystal seed approaches to the overheated melt surface (A) and is immersed in the melt (B). The seed is put into rotation and the melted material starts solidification process increasing lap by lap the crystal diameter and forming the so-called shoulder of the crystal (C). The next step is the rotative extraction of a constant diameter crystal (D). The crystal is pulled up till the end of the process. The

growth ends with continuous diameter decrease (E) up to the separation of the crystal from the melt (F) [17].

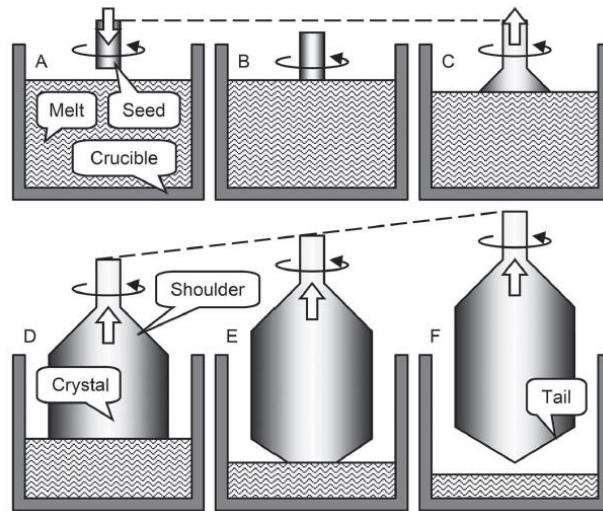


Figure 3.2: Czochralski single crystal production method [17]

This process becomes more expensive for high melting points materials. Many oxides have even higher melting temperatures (over  $2000^{\circ}\text{C}$ ), making them very difficult to grow. This fact reflects on the final cost of the scintillator and must be taken into account in the choice of scintillator. In such cases other methods can be used to produce samples of scintillators, such as ceramic processing [18]. In this method a mixture of proper proportions of dopants and host element undergoes to a chemical process to obtain a dried powder with precise chemical composition and grain size distribution. This is the starting sample of the next densification process which is realized through sintering and hot pressing. Sintering is a heat treatment where strong interparticle bonding transforms powder into a dense polycrystalline mass without melting it to the liquefaction point. Hot pressing further densifies the sample using a plunger system heated to high temperature (over  $1000^{\circ}\text{C}$ , depending on material). A pressure of several MPa compresses and densifies the powder resulting in a dense polycrystalline mass with a grain microstructure [10]. The final aspect is a transparent scintillator that efficiently transmits light to the photodetector.

### 3.2.1 Activator species

The activators are the ions responsible of radiation emission inside the scintillator material. Their study is very important for understanding and controlling the final luminescent feature of the scintillator.

Certain chemically pure crystal compounds, containing no added impurity, can be made to luminesce by an appropriate heat treatment. The heating produces a

stoichiometric excess of one of the constituents of the solid, and these excess ions, which occupy interstitial positions in the crystal lattice, function as luminescence activators. Scintillators containing these types of activators are called intrinsic.  $\text{CdWO}_4$  is an example, having already inside the groups  $\text{WO}_4^-$  which acts as luminescence center. The luminescence process in those species is quite different from the extrinsic scintillation (see [19, 20] for a detailed explanation). Extrinsic scintillator means that the scintillation process is due to specific dopant atoms added into the host material. This is the more widespread class of scintillators. Usually the host scintillator is followed by the dopant elements within the bracket.  $\text{NaI}(\text{Tl})$ ,  $\text{CsI}(\text{Tl})$  are example.  $\text{NaI}$  and  $\text{CsI}$  are the host materials while  $(\text{Tl})$  is the dopant ion.  $\text{Tl}$  is usually added in a small concentration to the alkali halide melt from which the crystal is grown [6, 20]. Like Thallium ( $\text{Tl}$ ) and Sodium ( $\text{Na}$ ), other commonly used activator elements are trivalent or divalent rare-earth ions, as example Cerium ( $\text{Ce}$ ), Europium ( $\text{Eu}$ ), Praseodymium ( $\text{Pr}$ ) and Terbium ( $\text{Tb}$ ). Among all these, the most common is  $\text{Ce}^{3+}$  which shows intense and fast photon emissions thanks to its  $5d-4f$  transitions [21]. Commercial  $\text{Ce}$ -doped scintillators are  $\text{LSO}$ ,  $\text{LYSO}$ ,  $\text{GAGG}$ ,  $\text{YAG}$ ,  $\text{YAP}$ ,  $\text{LaCl}_3$ ,  $\text{LaBr}_3$  [6].

In Figure 3.3 is shown the change in the emission spectrum coming from different dopants added to  $\text{CsI}$ . This allows to have different possibilities for better matching the scintillator to the light detector. For example, still in the same figure, it

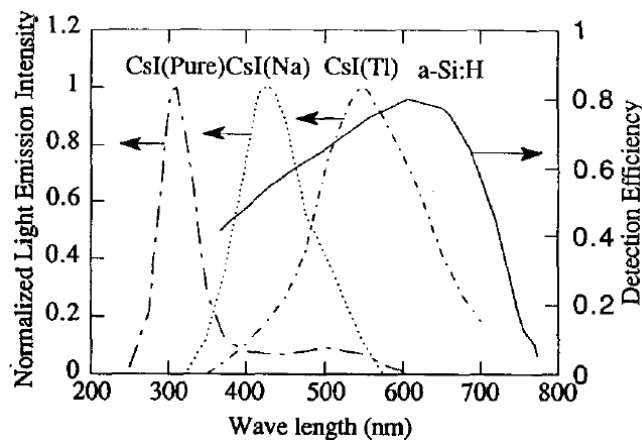


Figure 3.3: Scintillation spectra of  $\text{CsI}$  with different activator element and quantum efficiency of amorphous Silicon Photodiode [19]

is reported the quantum efficiency of an amorphous Silicon photodiode and it is possible to see that the best matching can be reach with the thallium doped  $\text{CsI}$ . Matching between scintillator and photodiode was already explained in 2.2.4.2.

For practical uses, sometimes host material is co-doped for increasing the performances.  $\text{CsI}(\text{Tl})$  was studied with a co-dopant ( $\text{Sm}$ ) in order to suppress the afterglow and Section 3.3.4 will report such example with a quick discussion.

## 3.3 Scintillator properties

The most important properties that must be taken in consideration in the choice of a scintillator are described below.

### 3.3.1 Light yield

Light yield is perhaps the most important parameter for any scintillation material. The reason is that if the light output is very low, the overall signal-to-noise ratio of the subsequent photodetector may not be acceptable. This is true especially for spectroscopic purposes where high carrier number is necessary in order to have results well above the systematic uncertainties of the system [8].

Each scintillator is characterized by a light yield defined as the number of emitted photons per unit of deposited energy (usually ph/MeV). For commonly used scintillators, a typical light yield is 20000-30000 photons per MeV [8]. Although there are no solid theories to predict the brightness of a scintillators, one phenomenological model is usually used to explain the observed light yield. Light output depends on the efficiency of electron-hole creation in the material, on the probability of capture at the luminescent centers and on the intrinsic emission quantum efficiency of these centers. So, it is possible to write the light yield as follow:

$$LY = \frac{E}{\beta E_g} \times S \times Q \quad (3.1)$$

where E is the deposited energy of ionizing radiation,  $\beta$  is a phenomenological parameter,  $E_g$  is the band gap energy, S is the energy migration efficiency from the host to emission centers and Q is the photoluminescence quantum efficiency, that is equal to the photoluminescence (PL) quantum efficiency. In this formula, the product  $\beta E_g$  is the energy required to generate a single electron-hole pair in the scintillators [6, 22].

Furthermore, the response of the scintillator must be directly proportional to the incident X-Ray dose up to the maximum imparted dose available from the X-Ray tube and it may, as much as possible, be independent on photon energy of the incident X-Ray. This is usually called *linearity of scintillator response* and it is another important feature that must consider.

### 3.3.2 Transparency and light transport

The transparency of the scintillator material is an important feature because the visible scintillation photon must be transported efficiently to the photodetector. The complete absorption of the incident X-Ray flux is required. Absorption mainly occurs in the entrance layers of the scintillator, which is at the opposite side of the photodetector. The emitted scintillation light must be transported through the material without significant attenuation. Light is emitted in all directions isotropically and not only towards the photodiode. About that some particular microstructure have been developed in order to “channeling” the light in the right direction and micro-columnar structures of Cesium iodide are an example [13, 23]. Columnar structure acts as an optical waveguide directing light towards the photodetector by a combination of reflection and scattering at surfaces. This is not to be confused with the design of a structured scintillator where columnar structures are fabricated to reach good spatial resolution. A comparison of the two is shown in Figure 3.4.

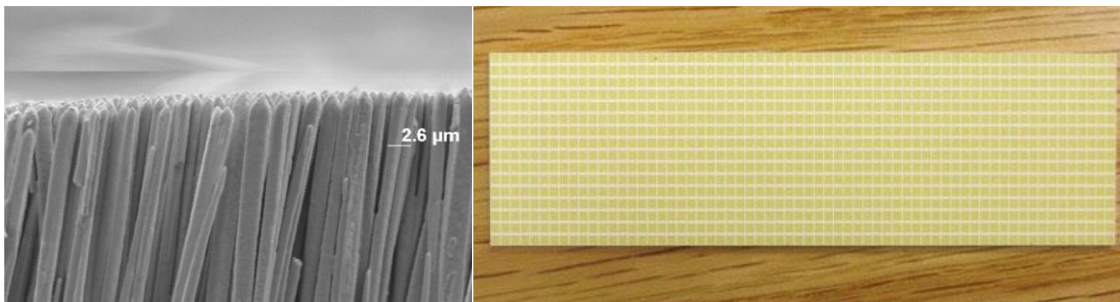


Figure 3.4: SEM micrograph of a microcolumnar film of CsI:Tl,Sm [23] and structured scintillator segmented by reflector (white strips) [13]

### 3.3.3 X-Ray stopping power

Another property is the photon stopping capability. Photon detection efficiency depends on how well and how quickly the impinging photons lose energy in the scintillation medium [8]. Some deleterious effects can arise from the insufficient absorption of the X-Ray flux on the scintillator. If the X-Ray photons are allowed to pass through the scintillator without absorption, the efficiency of the X-Ray detection is diminished. It may happen that these photons interact with the photodiode placed below the scintillator and this results in electronic defect creation in the diode, which manifests itself as an additional source of noise. This is essentially the problem of direct conversion in *Charge-Coupled Device* (CCD). In

medical imaging, CCD is a panel of semiconductor covered by a scintillator layer. Direct exposure of CCD to high radiation doses degrades its performance over time [8]. Therefore, it is important that the scintillator material is able to absorb nearly all of the incident X-Rays and it can be evaluated taking in consideration the stopping power of the material which was already discussed in 1.2. If we want to evaluate the lost fraction of photon after passing through the scintillator that is:

$$e^{-\mu(E)t} \quad (3.2)$$

where  $\mu(E)$  is the energy-dependent attenuation.  $t$  is the thickness of the scintillator and it must be chosen in order to have the max possible photons stopped consistent with the requirement that the scintillation light be efficiently transported to the diode surface. From that it is possible to understand the number of stopped photons inside the scintillator and evaluate the energy deposition. Particular attention must be paid to the energy deposition. The stopping power strictly depends on the photon energy and in some cases the evaluation of this parameter is not obvious and requires special tools. An example is our application, where a Polychromatic spectrum is produced by the X-Ray tube and the energy deposition evaluation must be done using a software (see 0).

To have an idea of the stopping power capability of the scintillator, we can appeal to the  $Z$  value of the host material. For a scintillator which is composed by multiple elements, it is possible to evaluate the effective atomic number ( $Z_{\text{eff}}$ ) parameter for a certain interaction process. Up to a hundred of keV for high- $Z$  materials the main interaction process is the Photoelectric effect. Although there are no concrete expressions, the  $Z_{\text{eff}}$  for Photoelectric effect can be expressed as [6]:

$$Z_{\text{eff}} = \left( \sum w_i Z_i^4 \right)^{1/4} \quad (3.3)$$

where  $w_i$  and  $Z_i$  are the fraction of the total mass associated with the  $i$ -th element and the atomic number of the  $i$ -th element, respectively. In this case  $Z_{\text{eff}}$  is an index of the capability of the scintillators to stop photons by Photoelectric effect. If the aim is to detect high-energy photons, such as X-Rays, dense materials having high  $Z_{\text{eff}}$  are preferred.

### 3.3.4 Primary decay time and afterglow

The time profile of a typical scintillation light is a pulse which rises very quickly (typical less than 1 ns) and decay rather slowly, with a time which can be as low as a few nanoseconds and as high as several milliseconds. Such delayed emission can degrade image quality and reduce the image accuracy. There are two mechanisms which contributes to the time of emission. The first is the intrinsic decay time of the emitting site. Usually it is in the order of ns and it is relevant in application

where a fast-primary response is required. It is evaluated by fitting the first part of scintillation decay curve with a decreasing exponential:

$$I(t) = I_0 e^{-\frac{t}{\tau}} \quad (3.4)$$

where  $\tau$  is the *characteristic decay time*. Sometimes the sum of two or more exponential functions are used for fitting experimental data and more  $\tau$  parameters are recorded.

The second mechanism is the most deleterious for our application: it leads to a very long tail of light emission, which produces an annoying constant light background. This process, named *afterglow*, derives from trapping of electrons or holes by lattice defects and their delayed thermal release. A practical example is reported in Figure 3.5 where CsI(Tl) is excited by a 100ms long pulse at different temperature [24]. It is possible to see that at low temperatures emission takes a long time to attenuate (black line). That is because traps remain filled and needs more time to empty. Instead, at high temperatures, traps empty rapidly appearing in a faster decay (blue line). In this recent work, the effect of co-dopant ( $\text{Sm}^{2+}$ ) in CsI(Tl) is studied. It was seen that Sm co-doping leads to a significant afterglow reduction [25]. Co-doping is a new trend in scintillator science and it is nowadays under development for a future commercial-scale production.

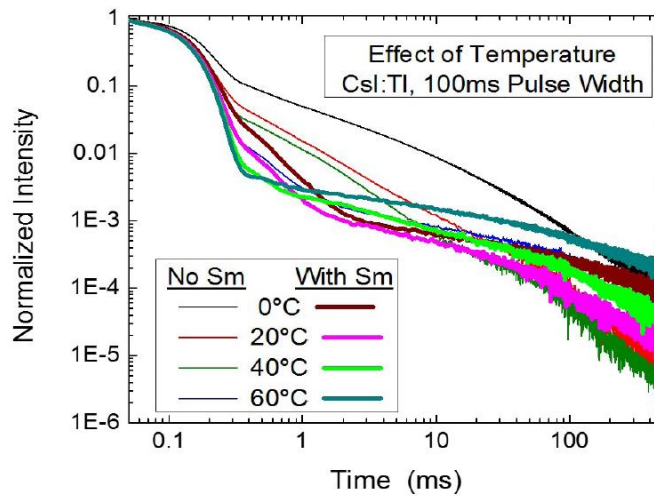


Figure 3.5: Afterglow data comparing CsI (Tl) and CsI (Tl,Sm) measured at different temperature [25]

As said, afterglow is very undesirable for applications using integrating techniques where delayed light, that can persist up to  $10^3\tau$  or longer, can become a significant contribution to the measured signal. Sometimes image reconstruction software requires a complex algorithm of data deconvolution to suppress the afterglow effects. Although these efforts actually improve the image, an increased projection noise is always present due to afterglow [26].

In the literature, afterglow is commonly characterized by a time value at which a certain reduction in light emission is recorded but there is not a standard definition for the experiments. Sometimes the time is recorded at different percentage of light reduction and so it is very difficult to compare different scintillator basing on this feature. There is also another method for evaluating this effect, that is also quite common, and it is the fraction of the scintillation light that remains 3 ms after stopping the X-Ray irradiation. An example of afterglow measurements is reported in Figure 3.6 where light outputs of different scintillators are recorded after that an electromagnetic shutter, a thick lead absorber, stop the irradiation. The voltage drop was normalized to 1 V for all the crystals in order to be independent of the light yield of crystals [27].

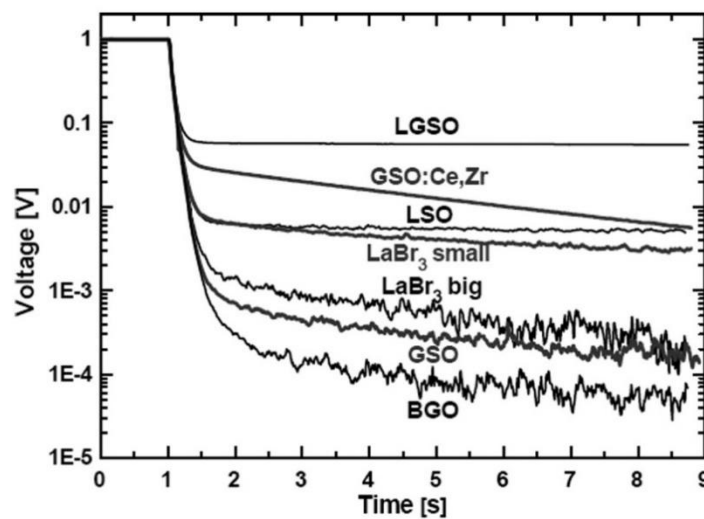


Figure 3.6: Afterglow of different scintillator [10]

### 3.3.5 Chemical stability and radiation hardness

It is very important that the properties of the scintillator remain constant during the whole working life of the machine. This requires high chemical inertia of scintillator material to avoid undesirable chemical reactions which may cause properties degradation. For ensuring chemical stability, some scintillators are encapsulated in an airtight container. All the hygroscopic materials suffer to moisture degradation and must therefore be canned. An example is the NaI scintillator which is a very hygroscopic material: if exposed to the atmosphere for any period of time, it deteriorates due to water absorption.

Maintaining radiation defect concentration under control is another important requirement to have the reproducibility of light output. In the literature, the ability to preserve properties under continuous irradiation fields is called *radiation hardness* [22]. Radiation defects can lead to form new levels in the energy

scheme of the material affecting the stability of light emission. This is a matter of concern mainly in bulky scintillation elements, where the scintillation process belongs to the entire microscopic structure of the scintillator [27]. The presence of radiation defects can induce a shift of the absorption spectrum which can overlap the emission spectrum. In this case re-absorption losses occur resulting in the overall light yield reduction of the scintillator. Radiation damage is characterized experimentally by exposing the scintillator to a relevant radiation dose and measuring the change in light output taken before and after the damage dose.

An example is given in Figure 3.7 where pure CsI scintillator was irradiated for several time. The decreasing in light gain after irradiation is not specific only to un-doped CsI, and many other materials have shown similar behavior [8]. This parameter has been considered mainly in the research for high-energy physics, but it also has importance in some medical imaging techniques [13], industrial flaw detection and synchrotron beam diagnostics applications as well [28].

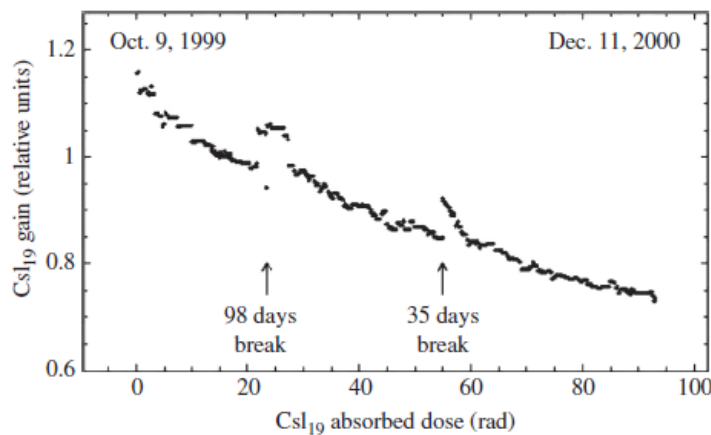


Figure 3.7: Decrease in gain of a detector based on undoped CsI [8]

### 3.3.6 Other properties

Almost all the parameters we described in the preceding sections depend on the temperature of the material. That is why the values given in the literature always correspond to operation at a certain temperature or within a range of temperatures [8]. Of course, an ideal scintillator must have all properties independent of temperatures, but in reality the most important parameter that must have limited reliance on temperature is the light yield.

The scintillator material should also have good machinability properties to be manufactured in different shape and size. Furthermore, its index of refraction should permit efficient coupling of the scintillation light to the visible light sensor [3].

### 3.4 Scintillators: market and research

An optimum scintillator should have high light output, high X-Ray stopping power, good spectral match with the photodetector, short primary decay time, low afterglow, high radiation damage resistance, light-output stability (time, temperature) but also compact packaging and easy machining. Easy machining is not a direct requirement but concurs to the final cost as well as the price of raw materials. Clearly it is not possible to have all these features in one material and the choice must focus on the properties that are more important for a specific application. A short primary decay time is not required when we are working in current mode while it is essential in pulse mode application. In spectroscopy measurements decay times of the order of nanoseconds are essential to avoid pulse pile-up. Figure 3.8 shows a correspondence between scintillator properties and the different fields of applications [22].

Applications Properties	Tomography CT, PET	Nuclear medicine SPECT	High-energy physics	Industry	Security	Environment
High density and atomic number	++	+	+++	++	+	++
High light yield	+++	++	+++	+	-	++
Fast response	+	-	++	-	-	-
High transparency	+	-	+++	+	-	-
Convenient emission range	+	-	++	+	++	++
Radiation stability	-	-	+++	-	-	+
Large size of single crystal	+++	-	+++	-	-	-
Low cost	+++	+++	+++	++	++	+

Figure 3.8: Field of application and required parameter importance [22]

As said in sub-section 3.3.3, X-Ray detections requires dense materials containing high-atomic-number elements are crucial. For that reason, organic scintillators will not be considered in our review. The focus for our application will be on inorganic scintillators having high brightness that is an important feature for obtaining good contrast in the final image (high signal to noise ratio) while timing is less demanding [18].

For the application on Gilardoni FEP machine, one of the major requirements is the use of low-afterglow scintillator materials. This is a well-known problem, especially in medical CT where the same physical process is used. It is reported that high scintillator afterglow can cause ring artifacts and image distortion in the final CT images. It occurs especially for CT modes with short integration periods and sometimes it is required a software correction. For some low-afterglow scintillators, like GOS, this can be not required [13].

In the following subsections we will list the advantages and disadvantages of some inorganic scintillators that are commonly used in radiation detectors focusing on their improvement and application. We will start from the scintillator currently used on Gilardoni FEP system, the CsI(Tl).

### 3.4.1 CsI(Tl)

As say before, CsI(Tl) was one of the first scintillators that had practical application. It is an alkali halide that has high  $Z_{\text{eff}}$ , high absorption efficiency and high light yield (66,000 ph/MeV). The emission peak is at 550 nm matching very well the PIN photodiodes. Other relevant features are the low-hygroscopicity, good machinability and resistance to radiation-induced damage [8]. CsI(Tl) exhibits high values of afterglow (0.3%), that, as mentioned before, concurs to image degradation [10].

In section 3.3.2 we already mentioned that a better light transport in CsI scintillator is possible when it is grown in columnar structure. That columnar microstructure also increased the spatial resolution, as it is shown in Figure 3.9.

CsI in columnar structure was employed in the scintillator-CCD medical imaging screens. These devices are composed by a layer of scintillating material coupled to amorphous silicon as readout photodetector. The needle layer can be directly deposited on the large photodetector surface through vapor deposition techniques. Detectors with an active area of over  $1000 \text{ cm}^2$ , with a thickness of 1–2 mm, are used in medical radiography, like in the gamma camera, providing remarkable upgrades in many kinds of medical imaging [28, 29, 30, 31].

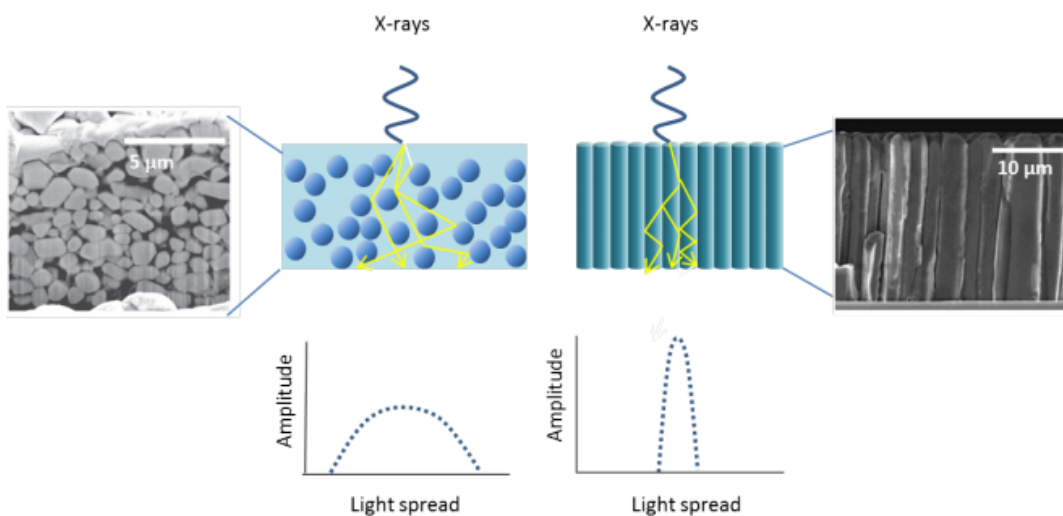


Figure 3.9: Schematic view of spatial resolution improvement due to columnar CsI(Tl)(right) on GOS(Tb) (left) [31]

### 3.4.2 NaI(Tl)

Another crystal produced in the late forties, together with the CsI(Tl), was Sodium iodide doped with thallium (NaI(Tl)). Till today it has been widely used thanks to its low production cost and high overall efficiency [28]. Its key features include high light yield (41,000 ph/MeV), very low scintillation light self-absorption, easy availability, low production cost and the ability to produce large area crystals. The emitted photons have an energy of 3 eV, that correspond to a wavelength of 415 nm [32]. The biggest problem of NaI(Tl) is its vulnerability to moisture. Because of its strong hygroscopicity, it must be used in a sealed assembly. NaI(Tl) applications include medicine, physics and environmental science. Since the properties of scintillators can be changed by varying doping levels, NaI(Tl) is usually tuned according to the application [8].

A relevant application of NaI(Tl) was the Anger camera, introduced by Hal Anger in 1958. Anger camera consists of a large NaI(Tl) slab read out by several photomultipliers (PMTs), allowing a precise determination of the  $\gamma$  interaction point. This invention offered unprecedented perspectives in the field of nuclear medicine imaging and non-invasive clinical investigations. But in spite of its very high light output NaI(Tl) suffers of a relatively low density ( $3.67 \text{ g/cm}^3$ ), that limits the spatial resolution and the image quality[19].

### 3.4.3 CdWO<sub>4</sub>

CdWO<sub>4</sub>, or simply CWO, is a dense crystalline scintillator with relatively low light yield (30% of CsI(Tl)), even though it has some desirable properties like the low intrinsic background and the low afterglow. The main issue of CdWO<sub>4</sub> is its long decay time, that makes it unsuitable for most applications [8]. Due to its high densities and the presence of Tungsten ( $Z=74$ ) as a major constituent, the CdWO<sub>4</sub> have high X-Ray absorption coefficients [20]. It has been successfully used in low intensity radiation applications such as spectrometry of very low activity of radioactive substances [8].

Applications in medical and security systems CT scanners are also reported. The main advantage of CdWO<sub>4</sub> over CsI(Tl) is the very low afterglow level (0.05% after 3ms). However, it is not optimal for CT applications due to its brittleness and due to the toxicity of Cadmium [18, 19].

New generation CT machines accomplish at least 100 projections per second and the most important requirements concerning scintillators becomes the short decay time. So, CT diagnostics based on CdWO<sub>4</sub> single crystals needs alternative materials to replace it [22]. This has been an argument for the search of a new generation of CT scintillators [19].

### 3.4.4 BGO

After the 1980s, some new materials that did not exist in the natural world were developed and an important example is the compound  $\text{Bi}_4\text{Ge}_3\text{O}_{12}$ , commonly called BGO. Its advantages include high absorption efficiency due to high  $Z_{\text{eff}}$  number ( $Z_{\text{eff}}=74$ ), short primary decay time, high-energy resolution, high-radiation resistance, great ability to produce large-size crystals and mechanical stability [8].

Because of its high  $\gamma$ -ray absorption efficiency, BGO is commonly employed in applications involving high energy photons. Most of the PET scanners produced in the last decade were built with BGO crystals. Unfortunately, a low light yield and a secondary decay time of 300 ns are still limiting factors. Modern PET systems are based on faster scintillators, like  $\text{Lu}_2\text{SiO}_5(\text{Ce})$  (LSO), its Y-admixture  $(\text{Lu},\text{Y})_2\text{SiO}_5(\text{Ce})$  (LYSO) as well as  $\text{Gd}_2\text{SiO}_5(\text{Ce})$  GSO [19].

### 3.4.5 $\text{PbWO}_4$

$\text{PbWO}_4$  is a very dense material ( $8.28\text{g}/\text{cm}^3$ ) with a high stopping power for high energy radiations. Its scintillation light is peaked at 440 and 530 nm, with decay times of 10 and 40ns. The main shortcomings of this material are the low light yield, on the order of 500 ph/MeV or fewer, that leads to rather poor energy resolution [18] in spectroscopy application. It also presents a strong temperature dependence of the scintillation light yield ( $-1.9\%/^{\circ}\text{C}$ ). The low melting point ( $1123^{\circ}\text{C}$ ) and the good abundance of the raw material make it a low cost scintillator, similar to  $\text{NaI}(\text{Tl})$  [19].

$\text{PbWO}_4$  has been developed for high-energy physics applications at CERN. It was selected by the Crystal Clear Collaboration for studying the new physics domain made accessible by the Large Hadron Collider (LHC) [19]. The particle detector of the structure is the CMS that is designed to see a wide range of particles and phenomena. Like a cylindrical onion, different layers of detectors record different particles interaction. This key data is used to build up a picture of events at the heart of the collision [33]. The layer dedicated to high energy photons and electrons detection is called Electromagnetic Calorimeter (ECAL). ECAL is composed by 75000 crystals of  $\text{PbWO}_4$ . This scintillator was chosen among other materials on the market because of its high stopping power, its fast decay time and its low price [19, 24].

### 3.4.6 Rare-earth oxyorthosilicates LSO-LYSO-GSO

Some rare-earth oxyorthosilicates have good scintillation properties. Their chemical formula is  $\text{Ln}_2\text{SiO}_5$  or  $\text{Ln}(\text{SiO}_4)\text{O}$  where Ln is Y, Gd or Lu. The materials currently available on the market will be describe here.

Lutetium silicate  $\text{Lu}_2\text{SiO}_5$  (LSO) is cerium-doped oxides that was discovered in 1990. It has high density ( $7.41 \text{ g/cm}^3$ ) and fast decay time (40 ns). Its scintillation light yield approaches 30,000 ph/MeV and its emission spectrum peaks at 440 nm. The main disadvantage of LSO is its very high melting point ( $>2000^\circ\text{C}$ ) which lead to high production price [24]. LSO is also known for its large afterglow, that makes it not acceptable for some application like CT detectors [Comparative Study of Scintillators for PET/CT Detectors]. A variant of LSO in which some of the lutetium is replaced by Yttrium atoms (LYSO) has recently been developed for increasing the stopping power of high energy photons [34].

At present, the LSO and its Y-admixture LYSO crystal are recognized as the best scintillators for PET, replacing BGO crystal that has lower decay time [26].

The problem in all lutetium-based scintillators is the presence of the radioactive isotope  $^{176}\text{Lu}$ . This isotope can introduce no negligible counting rates for some applications. For example, this is one major drawback of LSO for low energy Single Photon Emission Computed Tomography (SPECT) imaging [19].

Another rare-earth oxyorthosilicate Ce-doped is  $\text{Gd}_2(\text{SiO}_4)\text{O}$  (GSO) which has similar desirable properties to LSO but a relatively low light yield (8000 ph/MeV). It has the advantage to have no radiative isotope and therefore it can be used in low-signal-count-rate applications like hard gamma ray astronomy. Thanks to the great temperature stability, it is widely used in the oil well industry and geophysical explorations up to at least  $150^\circ\text{C}$  [17, 28].

### 3.4.7 Aluminium perovskite compounds YAP-LuAP-LuYAP

Some rare-earth Aluminum perovskites have shown very good scintillation properties. In general, they have high densities, short decays times and short peak emission wavelengths. The main disadvantages are a quite low light yield and modest density ( $5.37 \text{ g/cm}^3$ ). Cerium-doped Yttrium Aluminum perovskite,  $\text{YAlO}_3$  (YAP) was the first studied scintillator of this category. It has a fast decay time of about 20 ns that makes this material very attractive in all application where fast decay time is important. YAP is also well known for its mechanical stability and it can be cut in thin elements with high precision. This has been exploited by many researchers to design and develop high position sensitive detectors.

To increase the stopping power of YAP, Yttrium ( $Z=39$ ) can be substitute with Lutetium ( $Z=71$ ) obtaining  $\text{LuAlO}_3$  (LuAP) that has higher density of  $8.34 \text{ g/cm}^3$ . The emission wavelength of LuAP is suitable for matching to the most of photodiodes and imaging applications with good spatial resolution performances are reported [8, 35].

LuYAIO<sub>3</sub> (LuYAP) is a mixed composition YAP and LuAP. It was developed to capture complementary characteristic of the two former materials.

### 3.4.8 Lanthanum halides LaCl<sub>3</sub>-LaBr<sub>3</sub>

After the discovery of these materials around the year 2000, it took only 5 years before crystals of significant dimension were commercially available. Ce-doped LaCl<sub>3</sub> and LaBr<sub>3</sub> show a very high light yield and both materials have high  $Z_{\text{eff}}$  that lead to high stopping power. The fast decay time is another important feature of these materials that brings them to be good candidates for high resolution gamma spectroscopy. The scintillation decay trend of LaBr<sub>3</sub>(Ce) is dominated by a fast and approximately single-exponential component with a characteristic decay time reported of about 15 ns. The best performances are achieved with LaBr<sub>3</sub> that has a light yield of over 60,000 ph/MeV, leading to improved energy resolution [6].

Drawbacks associated at these scintillators are the presence of radiative isotope <sup>138</sup>La resulting in an intrinsic constant background. As mentioned before for <sup>176</sup>Lu, that is a problem for low count rate application like radio-astronomy spectroscopy [17]. Hygroscopicity is a relevant problem of these materials limiting long time operations in open air. Indeed, the emission wavelength peak places in the lower part of the visible spectrum (358nm) and it leads to a good matching with PMTs with bi-alkali photocathodes [6].

### 3.4.9 Garnet scintillators YAG-LuAG-GYAG-GAGG

Garnet materials typically have chemical composition of RE<sub>3</sub>(Al,Ga)<sub>5</sub>O<sub>12</sub>, where RE stays for rare-earth. Some impurity ions are added to create luminescence centers. The first discovered garnet scintillator was Y<sub>3</sub>Al<sub>5</sub>O<sub>12</sub>(YAG) that was firstly developed in 1960 for laser applications. In 1990s scintillator properties of Ce-doped YAG was investigated. YAG(Ce) exhibits intense light emission and fast decay time. It has been used mainly for charge particle detectors due to its relatively low  $Z_{\text{eff}}=32$  and its relative low density (4.56 g/cm<sup>3</sup>). To increase  $Z_{\text{eff}}$  of the material it was attempted to substitute Y with Lu creating the so called LuAG scintillator ( $Z_{\text{eff}}=63$  and density of 6.67g/cm<sup>3</sup>) [17]. Further studies consider the Gd-substitution leading to the develop of (Gd,Y)<sub>3</sub>Al<sub>5</sub>O<sub>12</sub>(GYAG).

R&D of these garnet scintillators has recently led to a new ultra-efficient single crystal family, the so-called multicomponent garnets. The balanced admixture of Gd and Ga cations in Aluminum garnet efficiently decreases the trapping effect leading to very high light, low decay time and low afterglow [17, 36]. An example is the newly Gadolinium Aluminum Gallium Garnet (Gd<sub>3</sub>Al<sub>2</sub>Ga<sub>3</sub>O<sub>12</sub>) also simply called, GAGG. It is another Ce-doped solid-state scintillator that was recently

developed as  $\gamma$ -Ray scintillator and it has the advantages of high light yield, short decay time and high density where compared to the other Ce-doped garnet scintillators [37].

### 3.4.10 Ceramic scintillators GOS

Recently an interesting class of materials, the ceramics scintillator, become available in the global market. The development of appropriate production technology aims to obtain competitive materials with properties similar to single crystals scintillator [28]. These materials are constituted by tight aggregated crystal micro-grains, each randomly oriented with respect to their neighbors. They are still under development as an alternative to materials for which crystals cannot form or the production process is expensive (for example due to high melting point). Development of such materials for the scintillator applications was triggered by the needs of CT medical imaging to substitute  $\text{CdWO}_4$  and  $\text{CsI(Tl)}$  crystals that are not optimal ones [28].

In the mid of 80th the first polycrystalline ceramic scintillators were introduced. The host materials are Yttrium and Gadolinium oxides,  $\text{Y}_2\text{O}_3$  and  $\text{Gd}_2\text{O}_3$ , that, after doping with Pr and Tb, demonstrate reasonable scintillation properties. Nowadays they are replaced by Yttrium Gadolinium oxide  $(\text{Y, Gd})_2\text{O}_2(\text{Eu})$  (YGO), and Gadolinium silicate  $\text{Gd}_2\text{O}_2\text{S}(\text{Pr, Ce, F})$  (GOS) based ceramic materials. YGO has a long decay time (1 ms) which result in a high level of afterglow that is again an important problem in CT application. GOS scintillator showed better figure-of-merit due to elevated density and effective atomic number. Several other dopants were studied (Tb, Eu, Pr, Nd and Dy). In practice the most suitable are  $\text{Tb}^{3+}$  (dominant emission peak at 540 nm) and  $\text{Pr}^{3+}$  (dominant emission peak at 490 nm). GOS(Pr) shows a very high scintillation intensity, further improved with Ce and F co-doped. The F-dopant increases emission efficiency, whereas the Ce-dopant concurs to reduce afterglow [10, 28].

Some materials mentioned in subsection 3.4.9 are also being investigated as candidates for incorporation into a ceramic. Ceramic YAG(Ce) and LuAG have demonstrated light yield superior of that of single crystal with the same decay time [17]. In an effort to increase  $Z_{\text{eff}}$  number Gadolinium has been added to produce  $(\text{Y,Gd})_2\text{Al}_5\text{O}_{12}$  (GYAG). Ce-doped GAGG scintillator was also developed in recent year in ceramic form achieving a light yield of over 70000 ph/MeV that is the highest light yield among the oxide scintillators [6]. The ceramic process opens the door to many combinations of material and activators that can further challenging the market producing scintillator with superior performances at a relative lower cost.

### 3.4.11 New Eu-doped rare-earth iodides scintillators

Recently a new class of halide scintillator has been identified as an extremely promising scintillator, that is the class of  $\text{Eu}^{2+}$  doped rare-earth iodides. Example of host material are  $\text{SrI}_2$ ,  $\text{CaI}_2$  and  $\text{BaI}_2$ . The most performant among them is the Eu-doped Strontium iodide  $\text{SrI}_2(\text{Eu})$  with a light yield reported of more than 100000 ph/MeV [19]. The main disadvantage is the slow decay time (over 1  $\mu\text{s}$ ) that is typical of Eu doped material [3]. First tests in gamma spectroscopy demonstrate that an energy resolution of about 3–4% at 662 keV could be reached, which is significantly better than conventional alkali halide scintillator performance. Therefore, the slow decay time limits its application at low-count rate measurement [3, 38].

## 3.5 Candidate scintillator

There are several factors that determine the suitability of a scintillator for our application. The reference scintillator is the  $\text{CsI}(\text{Tl})$  that is now used inside the acquisition system of FEP machine. The  $\text{CsI}(\text{Tl})$  in the form of columnar structure is used only on CCD panels and there is not any report in the market. Furthermore, for a possible FEP application, the candidate scintillator must be available in an array structure, that is needed for perfectly coupling with the already present PIN array line. So, another scintillator must be found for our application.

In the Table 3.1 a list of the already cited scintillators is reported with a summary of the most important features. To find candidate scintillator it is necessary to take into account all the properties described in section 3.3 and their relative importance for our application. Firstly, we focus on the light yield of the scintillators. As explained before in subsection 3.2.1, light yield indicates the number of scintillation photons that would be expected from a given deposited energy. The more photons will be produced, the better the contrast obtained in the final figure. With that constrain, a lot of scintillators are not acceptable for our application. If we want a final performance comparable to  $\text{CsI}(\text{Tl})$  the candidate scintillator must have a comparable light yield. Light yield of  $\text{CsI}(\text{Tl})$  is about 66000 ph/MeV, so, in general, all the scintillators with a light yield lower than 40000 ph/MeV must be discarded. A scintillator with a lower light yield than  $\text{CsI}(\text{Tl})$ , can still have comparable light output if its stopping power is better than  $\text{CsI}(\text{Tl})$ . As said in subsection 3.3.3, this is not simply to determine, essentially because it depends on the energy of the impinging photons and in our case the photon source is polychromatic. An indicator of stopping power level can be found in the density and in the  $Z_{\text{eff}}$  of the material. The higher these parameters are, the higher the stopping

Table 3.1 Survey of selected scintillators [3, 8, 10, 17, 18, 26, 28, 34, 39, 40, 41, 42, 43]

<i>Material</i>	<i>Light yield [ph/MeV]</i>	<i>Peak emission [nm]</i>	<i>Density [g/cm<sup>3</sup>]</i>	<i>Dominant decay time [ns]</i>	<i>Afterglow A : [% 3 ms] B : [% 3s] C : [% 6ms]</i>	<i>Hygroscopic</i>
<i>CsI(Tl)</i>	<i>50000-66000</i>	<i>550</i>	<i>4.51</i>	<i>1000</i>	<i>0.5a 0.5-5c</i>	<i>Slightly</i>
NaI(Tl)	38000-42000	410	3.67	230	-	Yes
<i>CdWO<sub>4</sub></i>	<i>20000</i>	<i>475</i>	<i>7.9</i>	<i>2000-14000</i>	<i>0.05a, 0.04b, Very low</i>	<i>No</i>
BGO	8000-10000	480	7.13	300	0.010b	No
PbWO <sub>4</sub>	300-500	410-430	8.28	2-10	-	No
LSO(Ce)	26000-27000	420	7.4	40	0.59b	No
GSO(Ce)	8000-12500	440	6.7	60	0.03b	No
LYSO(Ce)	30000-33000	420	7.1	45-53	0.52b	No
YAP(Ce)	18000-21000	350-370	5.3-5.5	30	-	No
LuAP(Ce)	12000-17000	365	8.3	18	-	No
LaCl <sub>3</sub> (Ce)	46000-49000	330-350	3.86	25-28	-	Yes
LaBr <sub>3</sub> (Ce)	61000-65000	358-380	5.08-5.3	16-35	0.06-0.46b	Very
LaBr <sub>3</sub> (Ce,Sr)	73000-77000	385	5.08	25	-	Very
YAG(Ce)	8000	550	4.55	70	-	No
LuAG(Ce)	24000-26000	525	6.67	55-65	-	No
GAGG(Ce)	50000-60000	520-540	6.63	90-170	-	No
GOS(Ce)	8000-10000	430	6.7	30-60	0.15c	No
GOS(Pr,Ce,F)	52800 (80% CsI(Tl))	490-510	7.3	4000	<0.01a, Very low	No
GOS(Tb)	50000	545	7.3	6x10 <sup>5</sup> -10 <sup>6</sup>	Very low	No
SrI <sub>2</sub> (Eu)	80000-120000	435	4.6	600-1600	-	Yes

power will be. In order to minimize the transmitted flux, it is possible to maximize the thickness but that could be done consistently with the requirement that the scintillation light must be efficiently reflected out of the scintillator volume onto the PIN surface. So, it is always better to have high-Z elements in the composition of the material and high density. For these reasons, we will focus only on scintillators having comparable or higher density than CsI(Tl).

Another important parameter is the peak emission wavelength. PIN photodiodes convert with good efficiency only visible photons with high wavelengths, better above 500nm (see 2.2.4.2). Another requirement for directly coupling scintillator with the PIN is that scintillator must be bare and without this one any scintillator must be avoided.

Hygroscopic scintillators must be encapsulated in sealed assembly (see 3.3.5) therefore they are not suitable to our application.

Considering all these constraints, the most promising class for our application is the Ce-doped garnet scintillators and the new class of ceramic scintillators. Unfortunately, this last class is very difficult to find on producers' catalogue because their recent discovery. Ceramic scintillators are nowadays under development and they maybe will be available on large scale in the next future. The only ceramic scintillators nowadays available on the market is the GOS scintillator, that is already used in Gilardoni dual energy systems. GOS scintillator has high yield, suitable emission wavelength (over 500nm) that could match in a very good way the PIN quantum efficiency. GOS scintillators could be a possible candidate scintillator.

As said, also Ce-doped garnet scintillators result to have desirable features for our application. Among them, prominent features are shown by GAGG(Ce) a Ce-doped newly developed scintillator. It is one of the brightest available scintillators with an emission peak at 540nm that could match very well with PIN. GAGG(Ce) has also good  $Z_{\text{eff}}$  thanks to the presence of Gd elements and higher density in respect to CsI(Tl).

The choice is limited to only two scintillators: GOS(Tb) and GAGG(Ce). GOS scintillator has lower light yield than GAGG(Ce) and the peak emission wavelength is less suitable to use it with PIN detector. For this reason the candidate scintillator will be GAGG(Ce) and from it we will expect better performances than now used CsI(Tl) one.

There is also another reason behind the choice of GAGG(Ce) as candidate scintillator. Recent study revealed that a ceramic version of GAGG(Ce) was fabricated by the vacuum sintering successfully, exhibiting better performance than the single crystal counterpart [44]. It is reported that ceramic GAGG(Ce) shows an absolute LY of 70000 ph/MeV with a primary decay time of 165ns. In general, advantages in terms of LY, optical properties, scintillation responses and afterglow

are expected from ceramic version but those are not fully analysed yet. Furthermore, the cheap production method could lead to a final benefit on the cost. In our work, we will focus on properties belonging to single crystal GAGG(Ce). Ceramic specifications will be very similar to the single crystal and, for this reason, our work could be useful for evaluating, in the future, a commercial GAGG(Ce) ceramic version.

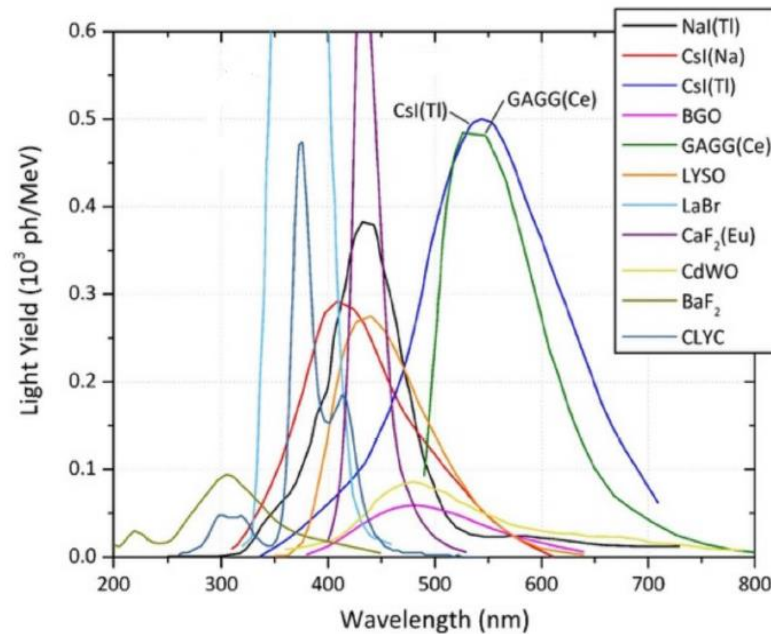


Figure 3.10: Emission spectrum of common scintillators [42]

In Figure 3.10 the emission spectrum of CsI(Tl) and GAGG(Ce) is reported. It is possible to see that the emission spectrum of GAGG(Ce) peaks approximately in the same spectral region than that of CsI(Tl). This is the best solution for matching the quantum efficiency of PIN. An investigation of this matching parameter will be found in the section of MATLAB Code. The deposited energy, that is affected strongly by scintillator composition, will be evaluated by MCNP software. Despite a deep research on the afterglow of GAGG(Ce), not comparable values were found. That is the problem described in subsection 3.3.4. In fact, in literature there is not a standard proceeding to measure it and the in general the literature is lacking because of its relative recent discovery.

In Table 3.1, the information about afterglow are measured at different time after the stop of photon flux (A;B;C). Sometimes there is not a reported value but only an approximate scale: Low, Very Low, High, Very High [27]. Kinheng producer reports that GAGG(Ce) has low afterglow [40]. Timing measurement of GAGG(Ce) was reported by *Pawel Sibczynski et al* [45]. As in Figure 3.11, GAGG(Ce) has faster decay time than CsI(Tl) and it seems to have also lower afterglow but, for a reasonable afterglow comparison, an experimental test should be

done with a sample of CsI(Tl) and GAGG(Ce) in standard working condition of FEP machine.

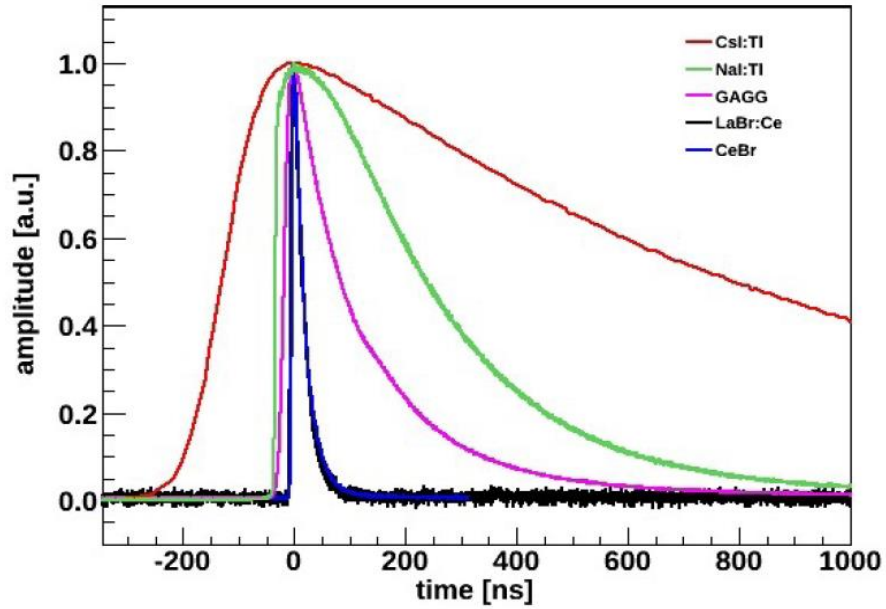


Figure 3.11: Decay time measurements of CsI(Tl) and GAGG(Ce) [45]

## 4 Efficiency evaluation

To evaluate the performance of the whole acquisition system, the efficiency must be evaluated for any acquisition step, which were already described in 2.2.1. The final aim is to evaluate the acquisition system performance with the GAGG(Ce) in comparison to the system with the CsI(Tl). As reported in Figure 4.1, there are four main processes that should be considered.

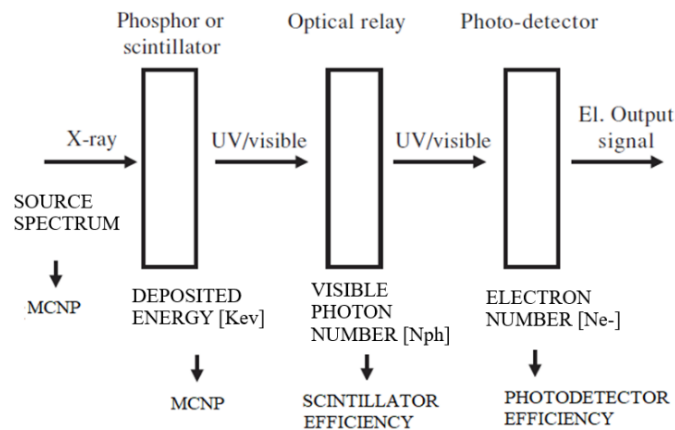


Figure 4.1: Acquisition system steps with each relevant quantity

Firstly, we must estimate the source spectrum because there is no data available about that concerning, neither experimental nor simulated. Thus, we must construct a model starting from the photon source.

The deposited energy inside the scintillator is the first step for the acquisition system. As mentioned in 1.2, the stopping power of a scintillator strictly depends on the energy of the impinging photons. The AION monoblock is a polychromatic source, that generates a broadly energetic spectrum (like that reported in Figure 2.2). This fact denies us the use of the Lambert Beer equation( 1.1 ) which is only valid for monoenergetic photons and for a defined geometry. To evaluate the source spectrum coming out from the AION monoblock and subsequently the deposited energy inside the scintillator, we will make use of MCNP software [46].

*“MCNP is a general-purpose Monte Carlo N-Particle code that can be used for neutron, photon, electron, or coupled neutron/photon/electron transport” [47].*

We decided to work with MCNP software because it is a versatile and functional software capable to simulate complex geometries. The user can also instruct MCNP to make various output (tallies) related to particle current and particle flux.

The second step is the optical relay of the light. Its efficiency must consider the light transport and the self-absorption phenomena inside the scintillator material, which strictly depends on the scintillator thickness. Due to the complexity of visible light physic inside a material, it must be experimentally evaluated. Thus, these processes are taken in consideration simply using the light yield parameter provided by the productor, assuming that the reported light yield does not change significantly with the scintillators thickness.

The last step is the conversion of visible photons into electrons, that is done by the PIN. The process efficiency corresponds to the matching performance already described in section 2.2.4.2. To evaluate it, we will use a MATLAB code, considering the Q.E. and the scintillator emission spectrum energy dependencies. As a result, we will find a final percentage of conversion.

There is also another sub-step before the photon conversion, that is the multiple surface crossing done by the visible photons coming from the scintillator. Visible photons firstly cross scintillator-optical glue interface and then the optical glue-PIN interface. Light refraction can lead to photon losses. This is the coupling issue and its optimization was already discussed in 2.2.4.1. We will assume that the coupling will be the same for each simulated scintillator and that it does not benefit either of them.

To sum up all the efficiencies we can describe our model with the following equation.

$$N^{\circ}e^{-} = E_d \cdot [Mev] \cdot LY \left[ \frac{Ph_{vis}}{Mev} \right] \cdot QE \left[ \frac{e^{-}}{Ph_{vis}} \right] \quad (4.1)$$

Equation (4.1) represents the mean number of outgoing electrons from the acquisition system when an X-Ray photon impinges on the scintillator.  $E_d$  is the mean deposited energy in the scintillator by a photon belonging to the AION monoblock flux. LY is the light yield of the scintillator while QE is the mean quantum efficiency of PIN which, in this case, correspond to the number of electrons emitted per scintillation event in the scintillator. From now on we will evaluate in details the arguments that we have quickly introduced in this section.

## 4.1 Monte Carlo models

The use of modelling simulations is well established in physic research as well as in medical imaging research. This stems from the flexibility such models offer and the ability they provide to compute otherwise unobtainable quantities of interest. Historically, researchers have invested a lot of effort on modelling the transport of primary ionizing radiation and secondary charged particles. Many

deterministic methods based on Lambert Beer's attenuation law have been proposed as well as many Monte Carlo (MC) approaches which simulate in a very accurate way high energy photon physics. The operation mode of MC code will be described in 4.1.1. Various detailed ionizing radiation MC simulation packages have resulted from these efforts, for example, EGSnrc, PENELOPE, MCNP, FLUKA, GEANT4, SIMSET, and VMC++ [7]. For the aim of this thesis work, such instruments are of particular interest and, as already said, among those we decided to work with the MCNP code.

After a quick summary on Monte Carlo code functioning, we will focus on the source of photons, trying to understand and model the internal structure of an AION monoblock. Then, we will proceed with data validation against experimental measurements. Once the source spectrum is considered to be accessible, we will be able to estimate the deposited dose by the Gilardoni AION monoblock in materials. So, in the last subsection, the obtained results of the first set of simulations will be used as the source term to assess the energy deposition performances of GAGG(Ce) compared to CsI(Tl) crystal.

#### 4.1.1 Monte Carlo methods

Monte Carlo methods are very different from deterministic transport methods. Deterministic methods solve the transport equation which is valid for the average particle behaviour while Monte Carlo obtains answers by simulating individual particles and recording some aspects of their average behaviour.

In the framework of particle transport, the Monte Carlo technique consists of following each of the many particles from a source throughout its life to its death (*i.e.* the residual particle energy is below the set energy threshold, or the particle escapes from the simulation universe). Particles are transported between events (for

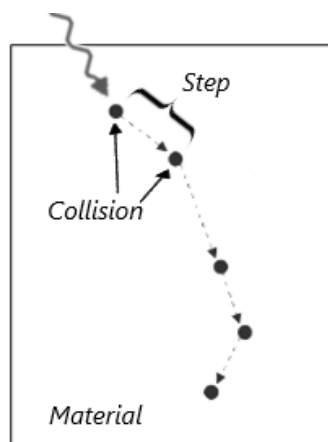


Figure 4.2 Monte Carlo particle simulation scheme

example, collisions) and each event is simulated sequentially to describe the whole phenomenon.

In Figure 4.2 is shown an example of how the path of a photon and electron (black dot) in matter is composed of several steps. Monte Carlo simulation transports both photons and electrons step-by-step in the material. The probability distributions that govern the events are experimental data measured in real experiments or from physical models which are collected in proper libraries. These distributions are randomly sampled to determine the outcome of each step. The statistical sampling process is based on the extraction of random numbers, as for gambling (hence the name Monte Carlo). In order to adequately describe a physical phenomenon, usually, the number of trials is very large, that leads Monte Carlo methods to be very computationally expensive.

#### 4.1.1.1 MCNP

MCNP (Monte Carlo N-Particle) is a widely used Monte Carlo code and it will be employed in our work. MCNP has the possibility of accommodating complex 3D geometries of any material and the multiple types of possible source definitions are some of its peculiar characteristics. The code treats an arbitrary three-dimensional configuration of materials in geometric cells bounded by surfaces. For photons, the code takes account of both Rayleigh and Compton scattering, the possibility of fluorescent emission after photoelectric absorption and absorption in pair production with local emission of annihilation radiation [47]. Furthermore, there are several features available to the user for detector simulations including pulse height output, which records the deposited energy in detector volumes. That could be very useful for simulation where energy takes much importance, like in dual energy detectors. An MCNP drawback is the lack of physic required to properly simulate all the parameter of a nuclear instrumentation chain. Examples of detector features not accounted for in MCNP include the effects of pulse pile-up, dead time, discriminator settings, tube bias and radiation damage [48]. Anyway, for our application MCNP provides performances that are more than enough.

The user creates an input text file that is subsequently read by MCNP. This file must contain information about the problem such as: the geometry specification, the description of materials, the location and characteristics of the source, the type of output desired and any variance reduction techniques used to improve efficiency [49, 50]. All the information is specified by dedicated commands, called “Cards”. The input text file is composed by three main blocks each one containing different cards type, as reported in schematic way in Figure 4.3: MCNP.txt example.

The user can instruct MCNP to make various output related to particle current, particle flux, and energy deposition. MCNP outputs are called tallies and are usually normalized “*to be per starting particle*” [50]. We will make use of tallies regarding

the flux averaged over a cell (f4) and pulse height distribution in a cell (f8) for our application. In order to understand the meaning of these output we will recall some theoretical concepts.

```

                                PROBLEM TITLE
c
c *****
c ***** CELL CARDS *****
c *****
c
Card 1.....
Card 2.....
.....
Card N.....
                                Blank line delimiter
c *****
c ***** SURFACE CARDS *****
c *****
c
Card 1.....
Card 2.....
.....
Card N.....
                                Blank line delimiter
c *****
c ***** DATA CARDS *****
c *****
c
Card 1.....
Card 2.....
.....
Card N.....
                                Blank line delimiter
    
```

Figure 4.3: MCNP.txt example

The definition of particle flux is:

$$\phi(\vec{r}, E, t) = vN(\vec{r}, E, t) \tag{4.2}$$

where  $v$  is the particle velocity and  $N$  is the particle density in a volume. Thus, the time integrated flux is:

$$\bar{\phi}_V = \frac{1}{V} \int dE \int dV \int dt \phi(\vec{r}, E, t) \tag{4.3}$$

It can be rewritten substituting Eq. 4.2 as follow:

$$\bar{\phi}_V = \frac{1}{V} \int dE \int dV \int dt vN(\vec{r}, E, t) \tag{4.4}$$

Defining  $ds$  to be the differential unit of track length:

$$ds = v dt \tag{4.5}$$

equation 4.4 becomes:

$$\bar{\phi}_V = \frac{1}{V} \int dE \int dV \int ds N(\vec{r}, E, t) \tag{4.6}$$

The quantity  $ds N(\vec{r}, E, t)$  may be thought as a track length density. Thus, the average flux can be estimated by summing track lengths. This is exactly what tally f4 performs, showing a final outcome in units of counts/cm<sup>2</sup> [47].

To modify what tallies produce as output the user can rely on many optional MCNP commands. For example, in our simulation we want to sort the fluency tally into energy bins. This may be accomplished by making use of the tally energy card (*En card*) which subdivides the output tally into energy groups [49].

We will also make use of f8 tally. The f8 pulse height tally provides the energy distribution of pulses created in a cell. In the output MCNP file this tally appears as count per energy bins defined by the En card. The energy bins correspond to the total energy deposited in a detector in the specified channels by each physical particle. It is very useful if the aim of the simulation is modelling a physical detector. It can also provide the total deposited energy in a cell when it is recalled in \*units [47].

#### 4.1.2 MCNP photon source modelling

FEP machine photon source is the Gilardoni AION monoblock. We want to realize an MCNP model of this source and, afterwards, we could correctly evaluate the deposited energy in the scintillator in a new simulation.

In order to create a proper geometry in the MCNP code it is necessary to understand the internal structure of this component. Firstly, looking at Figure 4.4, we will recall the operation of the system.

As said in section 2.1.1, photons are created through Bremsstrahlung process. The source of electrons, placed inside the tube, is the starting point of photon production.

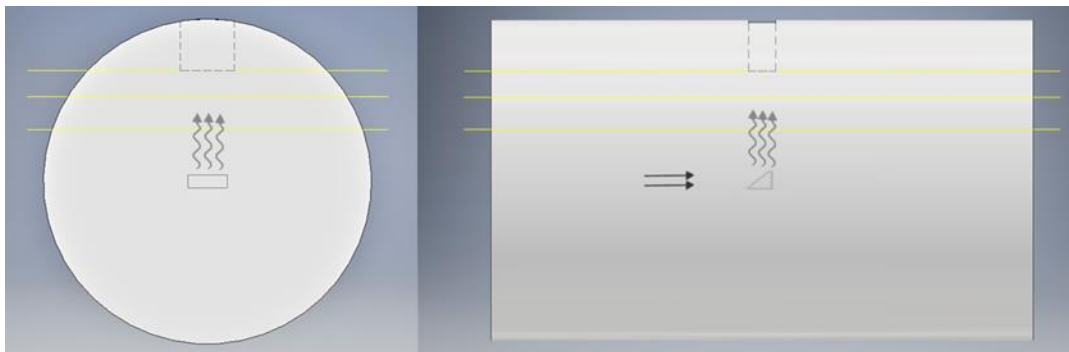


Figure 4.4: AION monoblock modelling picture

In Figure 4.4 two projections of AION monoblock are reported. The X-Ray output window is the dotted rectangular in the upper part of the schematic while the target is the one located at the centre and it is at 45°. The straight arrows represent the electrons, while the wavy arrows are the photons.

The electrons are accelerated by 150kV from the filament (not reported in figure) to the target. Once Bremsstrahlung occurred, the photon flux emerges from the target.

The output spectrum of AION monoblock is the outcome of three different filtrations, in Figure 4.4 they are represented by the layers between the yellow lines.

To have a final representative simulation these filters must be characterized both for density and for atomic abundance (or elemental mass fraction). Density data were already available from the Gilardoni dataset. Whereas, atomic abundance required a quick bibliographic research, especially for multi-element materials. As reported in Table 4.1, the most important parameters are the material composition, the density and the focal distance by which the thickness of each layer can be found. The mineral oil composition and the particular composition of borosilicate glass was obtained throughout a literature research [51]. For glass and oil MCNP material cards, we derived the elemental mass fraction for each element included into the material. In fact, MCNP accepts only the atomic abundance or the mass fraction as the microscopic description of the materials.

Table 4.1 AION monoblock filter composition

<i>Material</i>	<i>Composition</i>	<i>Density [g/cm<sup>3</sup>]</i>	<i>Thickness [mm]</i>	<i>Focal distance [mm]</i>
Filter 1: Glass	Borosilicate glass: 15-25% B <sub>2</sub> O <sub>3</sub> 65-70% SiO <sub>2</sub> Alkali and Al <sub>2</sub> O <sub>3</sub>	2.29	1.5	36
Filter 2: Isolating oil	As mineral oil	0.854	5	37.5
Exit cone: PBT	(C <sub>12</sub> H <sub>12</sub> O <sub>4</sub> ) <sub>n</sub>	1.24-1.34	1.5	42.5

As an example, in Table 4.2 it is reported the data of Boron trioxide, which is the main molecule inside borosilicate glasses.

Table 4.2 Mass fraction evaluation of Boron trioxide, B<sub>2</sub>O<sub>3</sub>

<i>Element</i>	<i>Atomic abundance</i>	<i>Atomic mass</i>	<i>Total mass</i>	<i>Mass fraction</i>
Oxygen	3	15.99	47.997	0.6894
Boron	2	10.81	21.62	0.3105

Elemental mass fraction referred to the single molecule must then be weighted by the molecular abundance into the material. Wherever a range of values is present, the choice was to take the mean value. Carrying on with the same example, Table 4.3 shows the results for total elemental mass fraction inside borosilicate glass material.

Table 4.3 Total elemental mass fraction evaluation

	<i>W<sub>i</sub>%</i>	<i>Si</i>	<i>B</i>	<i>Al</i>	<i>Na</i>	<i>K</i>	<i>O</i>
<i>SiO<sub>2</sub></i>	0.675	0.4674					0.5326
<i>B<sub>2</sub>O<sub>3</sub></i>	0.2		0.3105				0.6894
<i>Al<sub>2</sub>O<sub>3</sub></i>	0.0625			0.5293			0.4707
<i>Na<sub>2</sub>O</i>	0.03125				0.7419		0.2581
<i>K<sub>2</sub>O</i>	0.03125					0.8302	0.1698
<b>Total elemental mass fraction</b>	<b>1</b>	<b>0.315495</b>	<b>0.0621</b>	<b>0.033081</b>	<b>0.023184</b>	<b>0.025944</b>	<b>0.540176</b>

From the simulation we desire to obtain an output spectrum in terms of photon fluency to further use it as a source in the upcoming GAGG(Ce)-CsI(Tl) comparison simulation. Thus, we rely on the tally f4 of MCNP recording the average flux in a cell placed right after the PBT exit window. The result is shown in Figure 4.5: Simulated spectrum of Gilardoni AION monoblock photon source. As it is possible to see, there are three important peaks, around 58 keV, 59 keV and 67 keV. These are the characteristic lines of Tungsten  $K\alpha_2$ ,  $K\alpha_1$  and  $K\beta_1$  respectively. As reported in 2.1.2, we were expecting these lines because we work with an X-Ray tube which effectively has a Tungsten target.

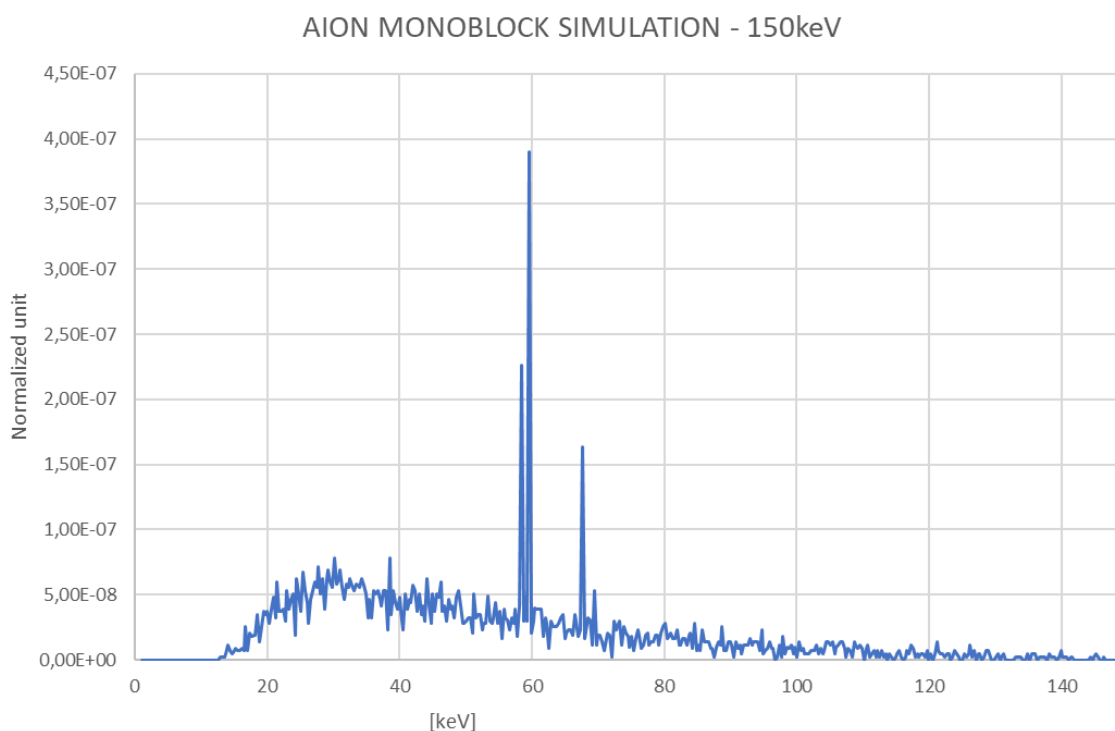


Figure 4.5: Simulated spectrum of Gilardoni AION monoblock photon source

### 4.1.3 Simulated data validation

The obtained fluency spectrum will be used as a source term for the energy deposition calculations. However, the accuracy of the simulation must be validated by comparing simulated data with experimental data. Thus, a spectroscopy analysis was done in the laboratory of Gilardoni Spa industry.

#### 4.1.3.1 Experimental setup

The experimental setup is depicted in Figure 4.6. It comprises an AION monoblock placed on a movable carriage and an X-Ray detector.



Figure 4.6: Experimental setup for spectroscopy analysis

The detector is the X-123 CdTe spectrometer produced by AMPTEK company. A spectrometer is able to discriminate photons according to their energy. This is possible thanks to ability of counting the number of charges created in the active material by radiation [3]. They operate in "pulse mode": all the generated charge by the single particle is completely collected by an electric field. The detector takes some time to completely carry out the charge collection process. The time period during which the detector can't detect a new event due to the analysis of the former one is called *dead time*. Having a high fluence rate it is possible that more photons simultaneously interact in the detector. This is the so-called *pulse pile up* phenomenon. The recorded energy becomes the sum of the interacting photons energies and so the measurement is distorted. Perhaps, the requirement of one interaction per collection time sets a limit in the photon flux detectable.

The AION monoblock is placed on a movable carriage pneumatically controlled by the operator. That is fundamental because the PBT exit window must be precisely aligned to the detector. If it is not, the photon beam changes its spectrum and the measured data may be distorted. During the test session, we had evidence of that, recording different outcomes at different alignment of the system. This could

be due to the small focal spot of the beam; if the beam is recorded at high angle, photons are mainly scattered, and they show altered energy undermine the measure.

To have the best possible outcome, the detector is aligned near the PBT exit window and then it is moved on the carriage to the farthest position from the source. This procedure reduces the photon flux intensity that otherwise would blind the detector because of pile up. The spectroscopy analysis is performed at the minimum current, 1 mA, and at 150kV which is the standard operation voltage.

Figure 4.7 shows the acquired spectrum. The Tungsten characteristic radiations appear at 59 keV and 67 keV. Peak appears in a broad shape because of the detector resolution. We can assume that the main interaction process in the detector is the photoelectric interaction. This is a licit assumption because we are working with relative low energy photons. In the following subsection it will be proved by looking at Figure 4.8.

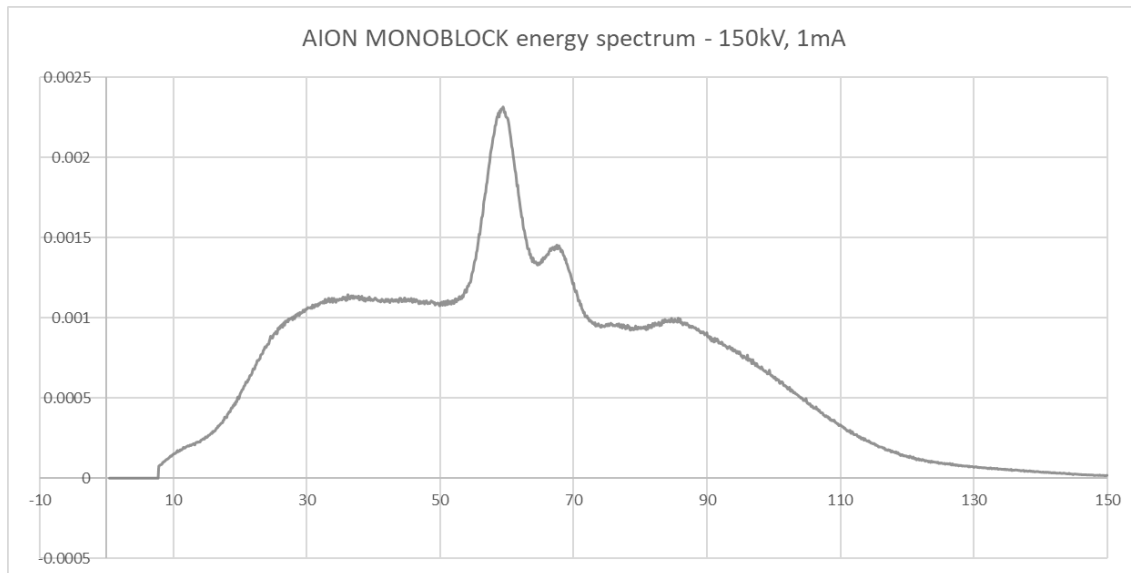


Figure 4.7: AION monoblock measured energy spectrum with X-123 CdTe spectrometer, normalized unit vs keV

When a photon interacts by photoelectric effect it loses all its energy in one collision creating a photoelectron with almost the same energy. Such electron strongly interacts by electromagnetic force with the matter and, in turn, it releases all its energy in a short range. Hence, we can suppose within reason that the deposited energy in the detector corresponds to the measured photon fluency. As a result, the two spectrums can be compared.

By looking at them it is evident that the high energy spectrum region is quite different. Thus, a further detailed analysis must be done.

#### 4.1.3.2 Data interpretation

We start trying to understand the meaning of each measured quantity and then we will focus on the features that are not taken into account in the simulation. The simulated spectrum represents the photons fluence, while the recorded spectrum is essentially the energy deposited in CdTe volume. A first hypothesis is that the discrepancy of data is due to the different efficiency at different energies of the spectrometer.

From AMPTEK X-123CdTe data sheet, the efficiency is reported to be high for low energy photons while it is low for high energy photons (see Figure 4.8). It is possible to see that the main contribution to the total interaction efficiency is due to photoelectric effect [52, 53].

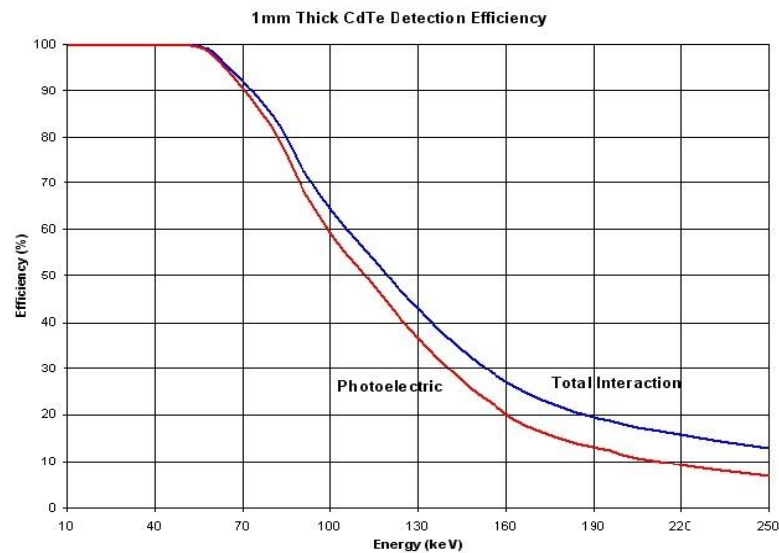


Figure 4.8: AMPTEK X-123CdTe efficiency [49]

With the purpose of taking into account the detector efficiency, we have two possibilities. The first method consists of multiplying the efficiency reported on the AMPTEK data sheet by the emission spectrum, while the second is to perform a new MCNP simulation using the tally f8, which corresponds to the deposited energy. Both these ways were carried out, without any important discrepancy as shown in Figure 4.9.

In order to directly compare all the spectrums, they have been normalized to a total integral equal to one.

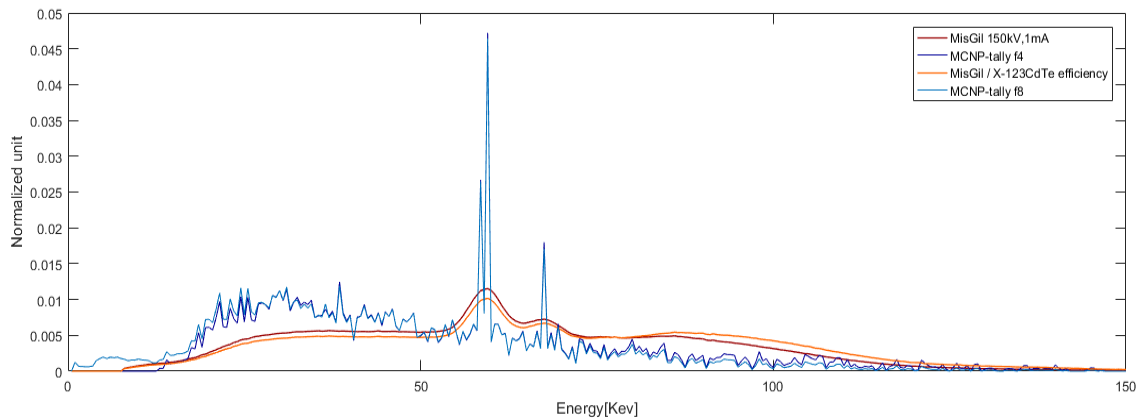


Figure 4.9: AION monoblock, experimental and simulated spectrum considering spectrometer efficiency

As we can see from the graphic in Figure 4.9, the high energy region has again higher count for experimental data with respect to the simulated one. Whereas for what concerns the lower part, the experimental spectrum seems to be cut compared to the simulated one.

This outcome is achieved with the presence of an additional filtration. For example, an increasing Al filtration on a Tungsten X-Ray tube spectrum is shown in Figure 4.10 for two different maximum spectrum energy. As it is possible to see the Al filtration lead to a hardening of the spectrum which has exactly the same effect recorded in our experimental data (compared to the simulated one).

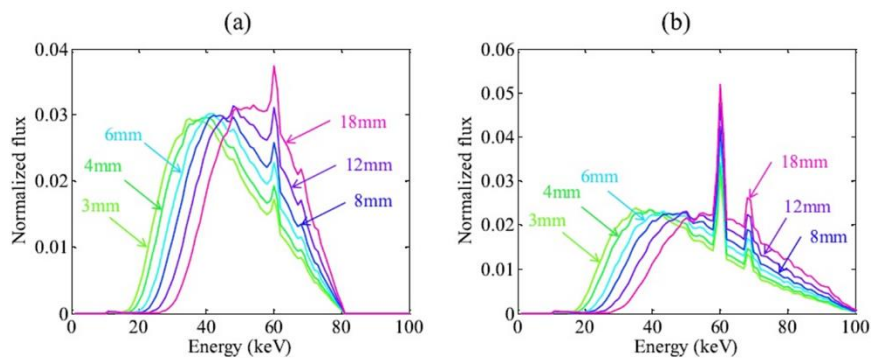


Figure 4.10: 80kV(a) and 100kV(b) model spectra with different thickness of Aluminium filtration [50]

So, driven from this bibliographic evidence we manage to redo our hypothesis assuming that an additional filtration is present. We tried to perform different geometries exploiting MCNP potentials before challenging the goodness of the experiment. The simulated spectrum is now used as the photon source for a new

simulation, where different spectra are recorded behind different Al thickness value. The results are shown in Figure 4.11.

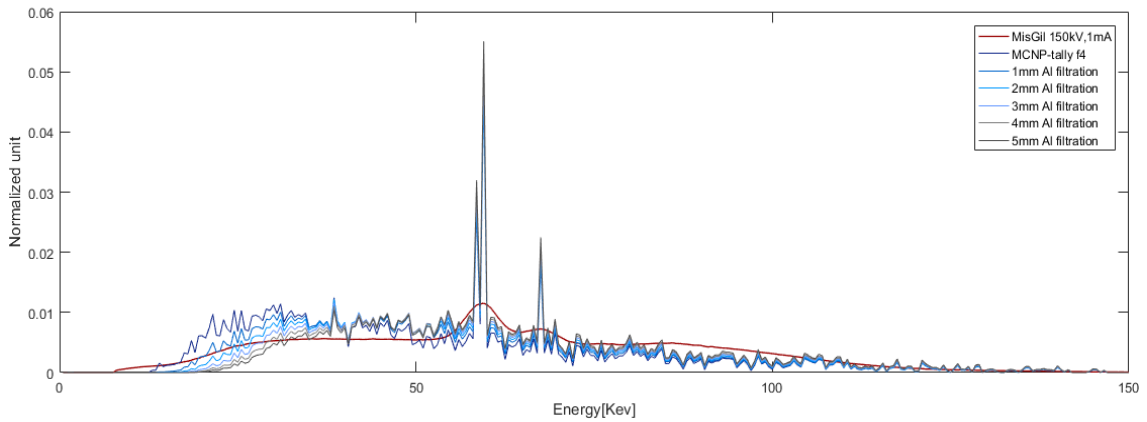


Figure 4.11: AION monoblock, simulated spectrum with different Al filtration. Experimental data has been reported as reference

The 2mm Al filtration seems to be the more appropriate filtration, but again the upper energy region has a different trend. It is important to say that this hypothesized filtration could not be a real filtration but just an equivalent filtration due to detector non-ideality. As reported in AMPTEK X-123CdTe data sheet, CdTe material stays behind a 100  $\mu\text{m}$  thick Be window and behind Pt electrodes. It is also guessable the presence of a dead layer which acts as an added filter. In order to clear up any doubt and trying any possibility, we create a new simulation taking into account also these non-idealities.

Such new simulation has the geometry reported in Figure 4.12 where a Be window 100  $\mu\text{m}$  thick is placed before the Pt contact 0.2  $\mu\text{m}$  thick. This data is reported in [52, 53, 54].

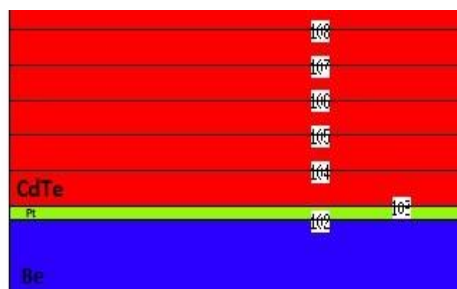


Figure 4.12: Dead layer simulation geometry, Xming software

To simulate the dead layers effect, we create five CdTe layers that have values from  $5\mu\text{m}$  to  $25\mu\text{m}$  with  $5\mu\text{m}$  interval. The used tally is again the f8. However, the active volume or, alternatively, the cell where the flux is averaged by MCNP, is placed behind the Be window, the Pt contact and the dead layer. The results of tally f8 in the active volume with and increasing dead layer filtration are shown in Figure 4.13. In this case, no relevant changes are achieved. This is essentially due to the small thickness of dead layers that do not have any appreciable effect on the resulting spectrum.

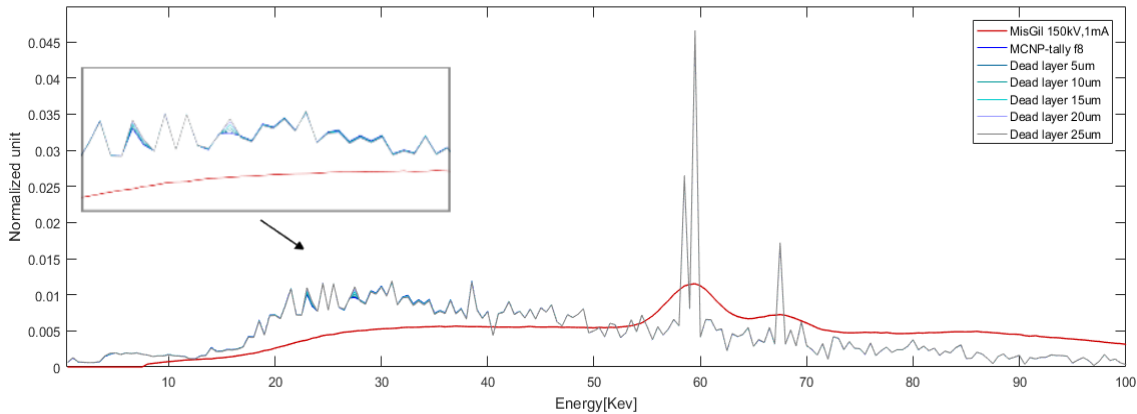


Figure 4.13: Energy spectrum with different dead layer

At this point, in order to evaluate the reliability of the measurements we repeated the measure following the same procedures and experimental setup. The outcome is reported in Figure 4.14 (blue line) where the first measurement is also reported as reference. We try to find the best alignment for the system, but the spectrum appears with a large peak centred around 90keV. Such peak has not physical justification to be generated inside the target material.

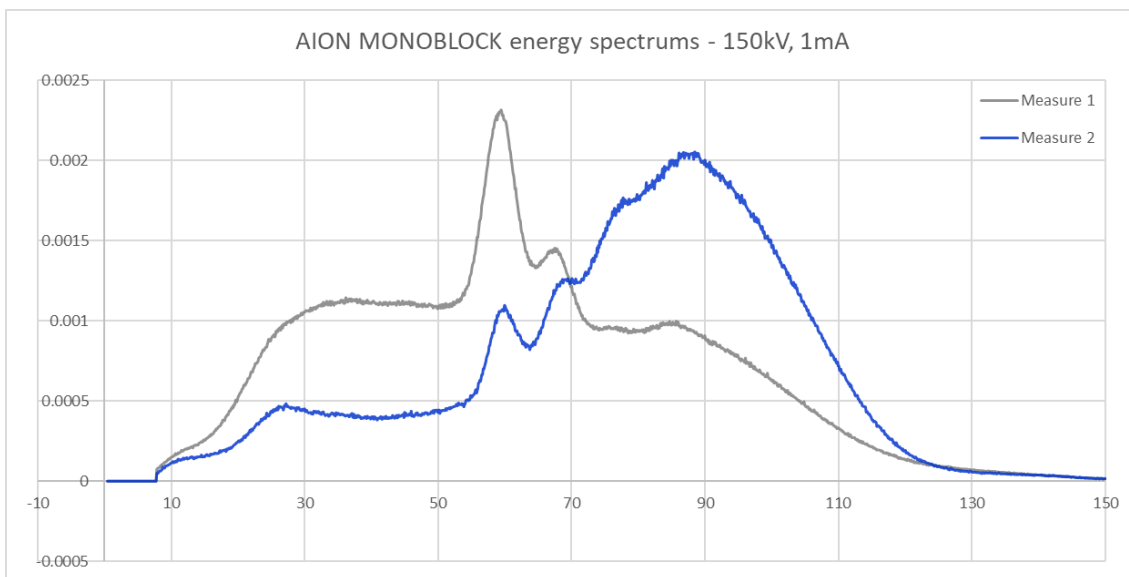


Figure 4.14: AION monoblock energy spectrum, different measures

Our hypothesis is that it is due to pulse pile up of the detector and, to prove our hypothesis, we proceed repeating different measurements and creating the associated simulations.

Firstly, we changed the voltage from 150kV to 85kV and then we filtered each spectrum with 1mm of Cu, all the results are summarized in Figure 4.15. Looking at the different recorded spectrum, we can see that at 85kV the high energy peak vanishes and the spectrum appears to be very similar to a typical Tungsten X-Ray tube spectrum, as the schematic reported in Figure 2.2. Comparing to the simulated one data, the measured spectrums seems very similar.

Equation ( 2.2 ) states that the radiative losses, and so the Bremsstrahlung process, increase its efficiency linearly with energy. This means that the photon flux at 150kV is almost twice the photon flux at 85kV. Such photon flux is probably too intense to be recorded without an important amount of pile up for the detector. It is reported that to ensure reasonable spectroscopic performance the maximum count rate is set at  $1.2 \cdot 10^5 \text{ sec}^{-1}$  for the X-123 CdTe using a peaking time of 2.4 $\mu\text{sec}$  [53]. To prove the presence of pile up, we evaluate the ratio between the simulated and measured total fluence with and without an additional filtration. The outcome is reported in Table 4.4.

Table 4.4 Fluence ratio evaluation

<i>Spectrum</i>	<i>Total fluence</i>		<i>Time [s]</i>	<i>Ratio</i>
	No filtration	1mm Cu		
85keV measured	1270728	174405	200	0.137248
85keV simulated	1.00E-02	8.35E-04	-	0.083470
150keV measured	9466409	8020810	200	0.847292
150keV simulated	1.00E-02	2.25E-03	-	0.225098

The ratio at 150kV is 0.84, that is very high with respect to the simulated one, equal to 0.22. Instead, the ratio measured at 85kV is similar to the simulated one (equal to 0.13 and 0.08 respectively). From this analysis we can conclude that the measures at 150kV are not reliable due to the potential and not-excludable pulse pile up effect.

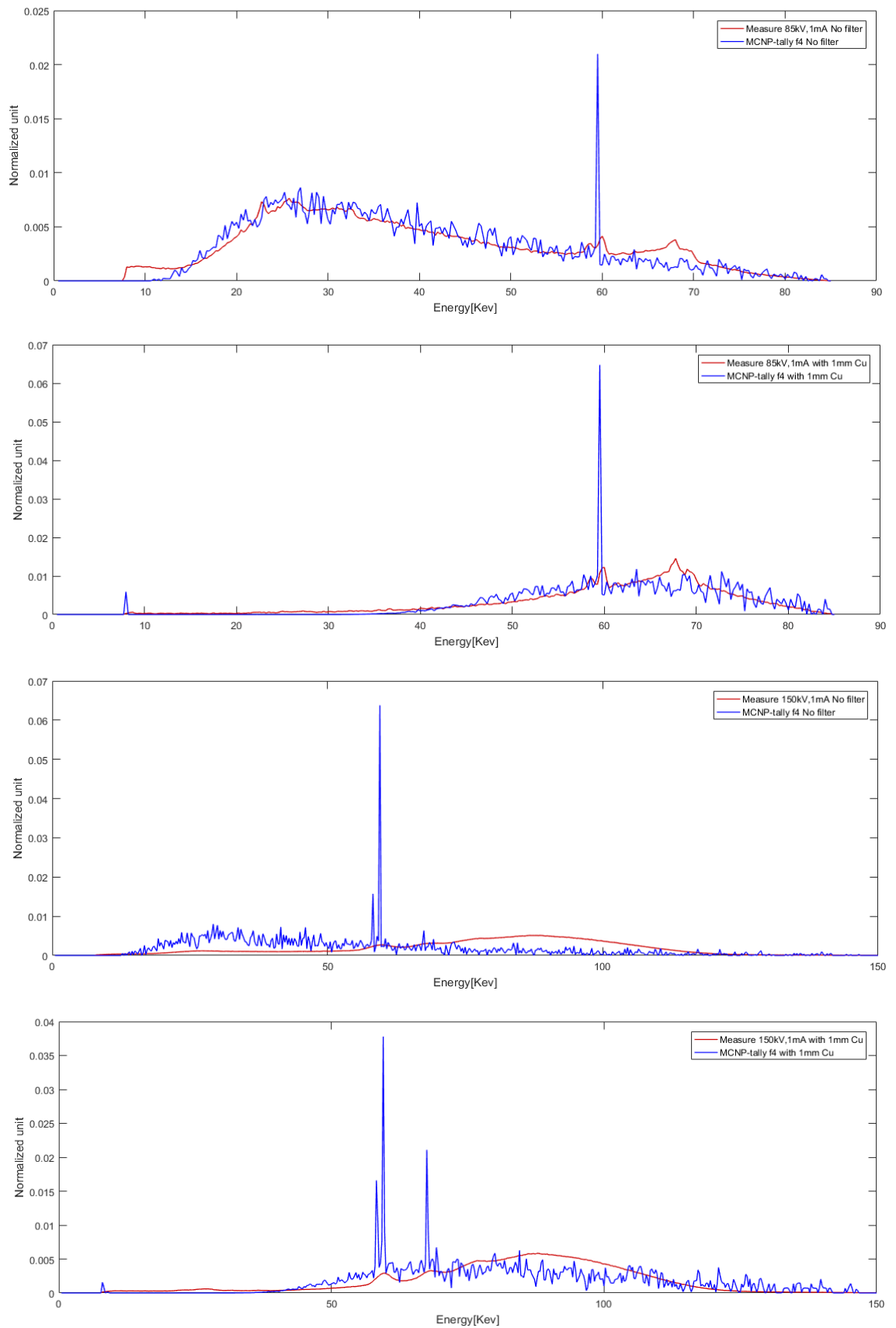


Figure 4.15: Simulated and experimental spectrums at 85kV and 150kV, with and without filtration

The validation process is now retained concluded. We ensured the inconsistency of the 150kV measure and we found a good match between the measure and simulated data at 85kV.

#### 4.1.4 Energy deposition evaluation code: MCNP tally f8

Once the simulation of the source term has been validated, we proceed with the energy deposition evaluation comparison between GAGG(Ce) and CsI(Tl). In this case the useful MCNP tally is the f8 tally, which correspond to the pulse height spectrum of the deposited energy. The simulated geometry is very simple. The source and the scintillator are placed in a rectangular parallelepiped (surfaces parallel to axes) which as the arbitrary dimension of 5x5cm. The whole system is shown in Figure 4.16.

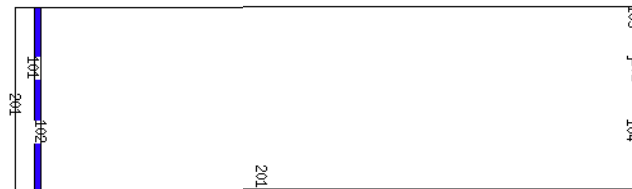


Figure 4.16: Geometry of the scintillator energy deposition simulations

The source emits photons perpendicularly to the detector with an energy spectrum equal to the one recorded in the AION monoblock simulation. The scintillator is located to an arbitrary distance of about 50cm (black layer in figure) and it is 1mm thick. Between the scintillator and the source there are 4mm of Al as an additional filtration (blue layer in figure). Such equivalent filtration was introduced in order to properly simulate the FEP machine during its operation. Usually, the AION monoblock spectrum is always attenuated by the baggage under inspection and so it never reaches the scintillator with its original shape. In Table 4.5 the main parameters of the simulations are reported.

Table 4.5 Simulation parameters

<i>Material</i>	<i>Density [g/cm<sup>3</sup>]</i>	<i>Thickness [mm]</i>	<i>Distance from the source [mm]</i>
Al	2.07	4	1
CsI(Tl) scintillator	4.52	1	51.4
GAGG(Ce) scintillator	6.6	1	51.4

The deposited energy in GAGG(Ce) and CsI(Tl) are simulated in two different simulations. The results are shown in Figure 4.17.

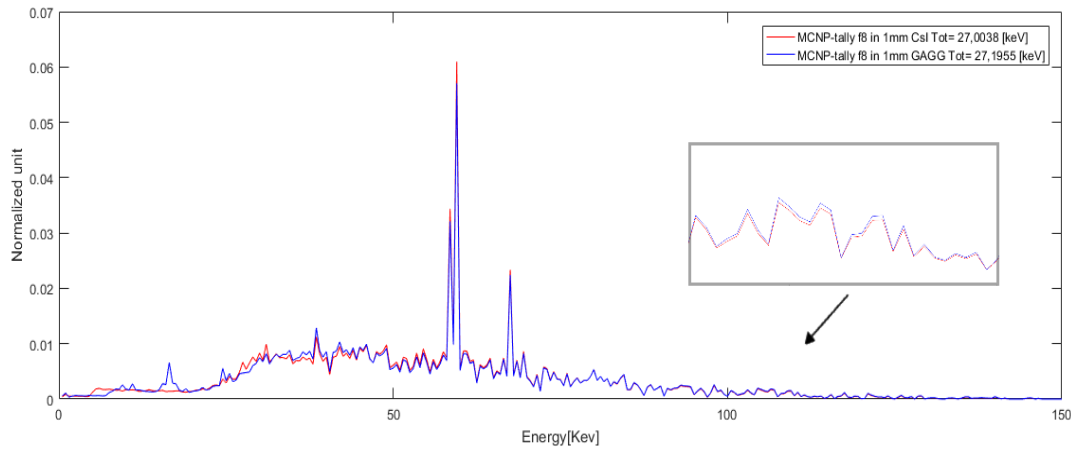


Figure 4.17: MCNP-tally f8 (pulse high spectrum) in GAGG(Ce) and CsI(Tl)

As it is possible to see the deposited energy spectrum is very similar. Between 30keV and 40keV the CsI(Tl) appears to be more efficient. The reason should be researched in the trend of the attenuation coefficient of CsI(Tl) as a function of the energy, which is shown in Figure 4.18 for the interval 10-100keV. The trend shows a peak exactly in the interval 30-40keV. This corresponds to the sum of Cs and I k edge and it is the source of high efficiency absorption in this range.

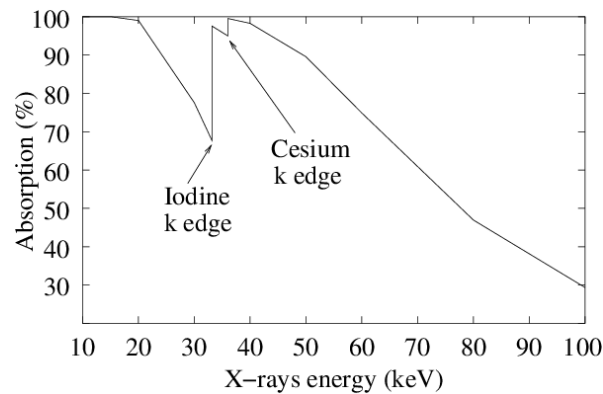


Figure 4.18: Attenuation coefficient trend of CsI(Tl) [51]

Apart from that, the GAGG(Ce) energy deposition is higher compared to the CsI(Tl) one. This is confirmed by tally \*f8 representing the total energy left in the material. Such value is equal to 27,00keV for CsI(Tl) and it is equal to 27,19keV for GAGG(Ce). Such energies correspond to the mean deposited energy per source photon. Once this result has been achieved, we proceed our analysis focusing on the matching with the PIN photodiode.

## 4.2 MATLAB code for matching evaluation

Matching efficiency was already discussed in section 2.2.4.2. The matching analysis is commonly done approximately looking at wavelength of the main emission peak. It is important to say that the emission spectrum could be very broad, and it could also have different emission peaks. So, in order to evaluate the efficiency of the electron conversion of the photodetector it is important to take into account the whole spectrum. Thus, we carry out the folding of the two spectrums multiplying wavelength by wavelength the scintillator emission spectrum to the quantum efficiency of the photodetector. To do that we developed a MATLAB code.

### 4.2.1 GrabIt tool: from graphic to raw data

Usually, the scintillator producers reported on their brochure only the peak emission value of the emission spectrum of the scintillator. The emission spectrum depends on the host material and on the activator elements responsible for the scintillation process. For this reason, for CsI(Tl), of which we do not have a direct spectrum measurement, we rely on bibliographic data. We assume that the emission spectrum is the same for all the CsI(Tl) scintillators available in the market. That is not exactly true because the emission spectrum depends on the activator concentration and on the production process (i.e. the resulting defect concentration of a production method can quench light wavelength in a different manner modifying the spectrum). In particular, such data are already reported in Figure 3.3, where CsI spectrums are recorded for different CsI activators. We focus on the CsI(Tl) spectrum.

In order to transform such graphical data in raw data available for MATLAB elaboration we made use of the MATLAB tool GrabIt. Thanks to it, multiple data sets can be extracted from a single image file, and the data is saved as an n-by-2 matrix variable in the workspace of MATLAB. After loading the image file, it is necessary to calibrate axes dimensions selecting 4 points on the image. Then, it is possible to grab points by clicking on graph lines. In Figure 4.19 an example of GrabIt user interface is shown.

We repeat this process also for the quantum efficiency of PIN, extracting data point from the Figure 2.10. At the end, we have raw data available for further elaboration.

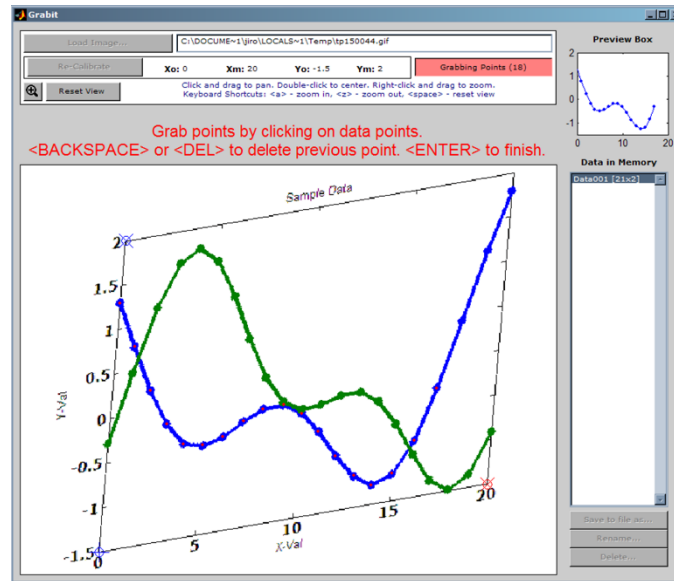


Figure 4.19: GrabIt interface

## 4.2.2 MATLAB matching code

From GrabIt data-image extraction we have now available the raw data shown in Figure 4.20. These data have not the same wavelength scale because of the casualty of choosing points by mouse click on the image during GrabIt acquisition.

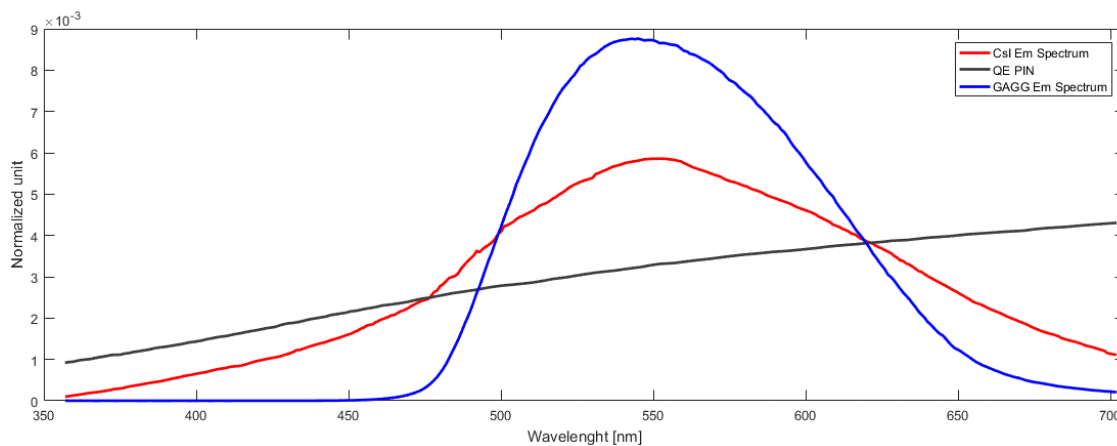


Figure 4.20: Emission spectrum of CsI(Tl) and GAGG(Ce). QE of PIN

In order to evaluate the goodness of matching we want to multiply the emission spectrum to the QE of PIN for each wavelength values. In other words, we want that all the spectrums have the same scale of energy. To do that we used the function “interp1” of MATLAB. The command syntax is displayed in the following example:

$$vq = \text{interp1}(x,v,xq) \quad (4.7)$$

This function returns interpolated values of a 1-D function at specific query points using linear interpolation. Vector  $x$  contains the sample points, and  $v$  contains the corresponding values,  $v(x)$ . Vector  $xq$  contains the coordinates of the query points [55]. An operation graphical example is shown in Figure 4.21.

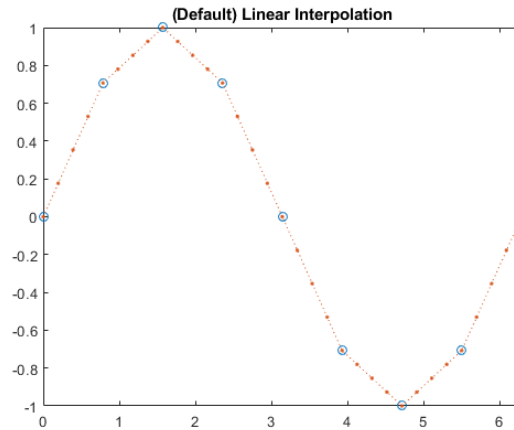


Figure 4.21: *Interp1* operation example [49]

Once this is done, we normalize the emission spectrum areas to 1 and we proceed with the multiplication. To do that we used the element-wise multiplication:

$$C = A.*B \quad (4.8)$$

this function simply multiplies arrays  $A$  and  $B$  element by element and it returns the result in  $C$ . Doing so, we are able to obtain a final spectrum corresponding to the elements by elements multiplication of each scintillator emission wavelength to its corresponding PIN QE. At the end, we need to evaluate the integral of the resulting spectrum summing each wavelength channels. The results are reported in the following section.

### 4.3 CsI(Tl), GAGG(Ce) comparison result

We reported all the results in the following Table 4.6.

Table 4.6 *Efficiency results summary*

	<i>CsI(Tl)</i>	<i>GAGG(Ce)</i>	<i>HLY-GAGG(Ce)</i>
<i>Deposited energy [MeV]</i>	2.70E-02	2.72E-02	2.72E-02
<i>Light yield [ph/MeV]</i>	54000	54000	60000
<i>Matching conversion factor [e<sup>-</sup>/ph]</i>	50.69E-02	52.36E-02	52.36E-02
<i>Emitted e<sup>-</sup></i>	739.22	769.07	854.52
<i>Gain</i>	0	4.0%	15.6%

As it is possible to see the deposited energy is better for GAGG(Ce) scintillator, essentially for its superior density. Unfortunately, the LY of CsI(Tl) installed on FEP machine is unknown to the company. The LY of CsI(Tl) is reported to be in the range of 50000-60000ph/MeV in literature (see Table 3.1). On the website catalogue of the most relevant scintillator producers it is reported to be about 54000ph/MeV [39, 42]. For this reason, we decide to use such value for our analysis. Meanwhile, for the GAGG(Ce) scintillator, LY up to 60000 are reported on the producers' website. We evaluate a hypothetical scintillator which has the same LY of CsI(Tl) and a real scintillator produced by Kinheng company in the High Light Yield (HLY) version [40].

The matching conversion factors is the result of the integral of the multiplied spectrum described in 4.2.2 section. The emitted  $e^-$  is the multiplication of the preceding three steps efficiency and the gain is per percentage advantage resulting in emitted  $e^-$  for GAGG(Ce) with respect to CsI(Tl) calculated using the following equation:

$$\text{Gain} = \frac{e^- \text{ GAGG} - e^- \text{ CsI}}{e^- \text{ CsI}} \times 100 \quad (4.9)$$

It is clear that the GAGG(Ce) scintillator has better capability to stop photons coming from the AION monoblock photon source. It also has a better matching with the PIN photodiode. Such advantages make it theoretically more performing than CsI(Tl) scintillator in our application. The percentage gain of the output signal using GAGG(Ce) scintillator with the same CsI(Tl) LY, can reach a value of 4%. Meanwhile, if we consider the HLY-GAGG(Ce) produced by Kinheng company, a gain of about 16% could be reached.

# 5 Conclusion

In this work we reviewed the common scanning techniques paying special attention to the X-Ray baggage scanners. We deeply understood their functioning, from the photon source to the acquisition system. The scintillator plays a central role in this system having the aim to be the primary X-Ray sensor. We analyzed in detail the scintillator operation and we believed that we could have proposed a new and innovative method that could help the Gilardoni Spa in the choice of new scintillator materials for their applications.

Over the last two decades, X-Ray security system as well as high energy physics and medical imaging required a strong drive toward innovation of their acquisition systems. This has reflected on the market of scintillator promoting an active R&D leading to a broad choice of performant materials. Since the market has such a wide choice, we believed that the best solution was to review them. Our research led us to a summary of performant scintillators. Among those we chose GAGG(Ce) as a candidate scintillator to improve the output signal performance of the acquisition system of Gilardoni Spa FEP machines. In order to confirm that, we evaluated the new efficiency of the system in comparison with the CsI(Tl) scintillator which is the one nowadays used into Gilardoni Spa acquisition system.

Our model for performance evaluation was essentially divided in two parts. The first one is centered on the deposited energy comparison between GAGG(Ce) and CsI(Tl). To accomplish it we developed a modelling of the Gilardoni Spa photon source using MCNP Monte Carlo simulations. Once we had validated the simulation, we obtained a powerful tool that allowed us to perform a wide range of analysis. The comparison between CsI(Tl) and the candidate scintillators lead us believe that the GAGG(Ce) was the best choice.

The second part was developed using MATLAB software for evaluating the goodness of matching between scintillators and PIN. Once again, the outcome was better for GAGG(Ce).

In conclusion, the electrical signal gain is expected to reach up to 16%, leading GAGG(Ce) to be a real performing potential substitute. A future practical application of this new scintillator has to be completed taking into account other parameters that are not easily comparable. This is the case of the afterglow characterization. GAGG(Ce) is a recent discovered scintillator and because of this the literature is lacking. CsI(Tl) is known to have an high afterglow while the GAGG(Ce) is still under investigation. A recent study suggest that the afterglow should be lower for GAGG(Ce) [45]. However, the only way for a complete

evaluation of some parameters is testing them directly on field. A conclusive experimental test was scheduled with a sample of GAGG(Ce) produced by Hamamatsu. Due to the Covid-19 emergency it has not been completed.

However, our thesis work opens to a wide range of possible future evaluations and analysis. The MCNP modeling of AION monoblock could be used for further works. An example is reported in Appendix 1, where a dual energy system is modelled and simulated. Information about the pulse height spectrum of the deposited energy could be recorded in each layer of the sandwich detector. Simulation of different layer thickness could carry on in a rapid way, simply modifying a value in the simulation. This could be done to accomplish requests such as a different distribution of information (*i.e.* a higher percentage of information in the high energy region).

Furthermore, the proposed approach of performance evaluation is very reliable, and it considers the most important parameters with their energy dependencies. Such method could be valid for future evaluations like the attracting class of ceramic scintillator. About that, some recent studies show very promising performance of ceramic GAGG(Ce) compared to the single crystal one. This work could be a starting point for future goodness evaluation of this scintillator in Gilardoni Spa application.

# 1 Appendix

## *Gilardoni Spa dual energy system*

During this work we create a powerful tool based on the MCNP code. After had modelling and then validated the simulation inherent to Gilardoni Spa AION monoblock, it is possible to use that tool in a large field of new analyses. Such appendix would be an example of a possible further analyses.

The dual energy system was already described in 2.3.1 in a general way. Gilardoni Spa offers a wide range of products based on that system, especially the airport security scanner. The technology used in this system is the L array detector structure already studied in 2.2.1. The difference relies in the scintillators geometry which is actually a dual energy configuration. The Low Energy Scintillators (LES) is the GOS scintillator which was taken into account in our literature review. For the high energy scintillator (HES) the company's choice was the CsI(Tl) scintillator. Between LES and HES there is a layer of Cu material. The aim of this layer is to separates as much as possible the low energy spectrum region to the high energy spectrum region. In the Table A1.1 there is a summary of the dual energy layer, layer thickness are confidential data.

*Table A1.1 Geometry specification*

<i>Scintillator</i>	<i>Thickness</i>
GOS	t1
Cu	t2
CsI(Tl)	t3

To evaluate the effectiveness of the Cu layer we develop a MCNP simulation of the system. We want to study the percentage of information coming from LES and from HES. The photon source is the already validated simulation of AION monoblock, while the detector geometry corresponds to that shown in Figure A1.1.

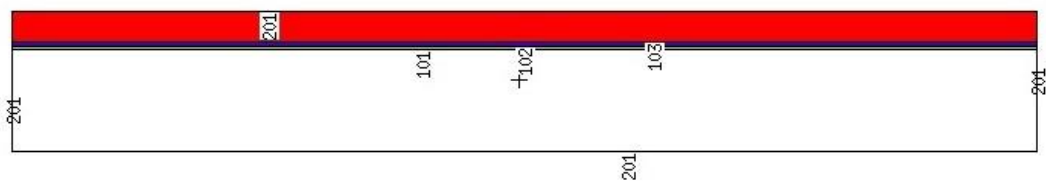


*Figure A1.1: Geometry of dual energy simulation*

The density data and material specification of each scintillators were provided by the company. The MCNP tally is again the tally f8 corresponding to the deposited energy into a specified cell. The pulse height spectrum is recorded in LES cell and in HES cell.

The results are shown in Figure A1.2. The two spectrums are well separated. LES scintillator is actually efficient in the low energy region of the spectrum and its counterpart, the HES, records energy belonging to the high energy region. From the simulation we can also deduce the ratio of each integrals, which correspond to the total deposited energy.

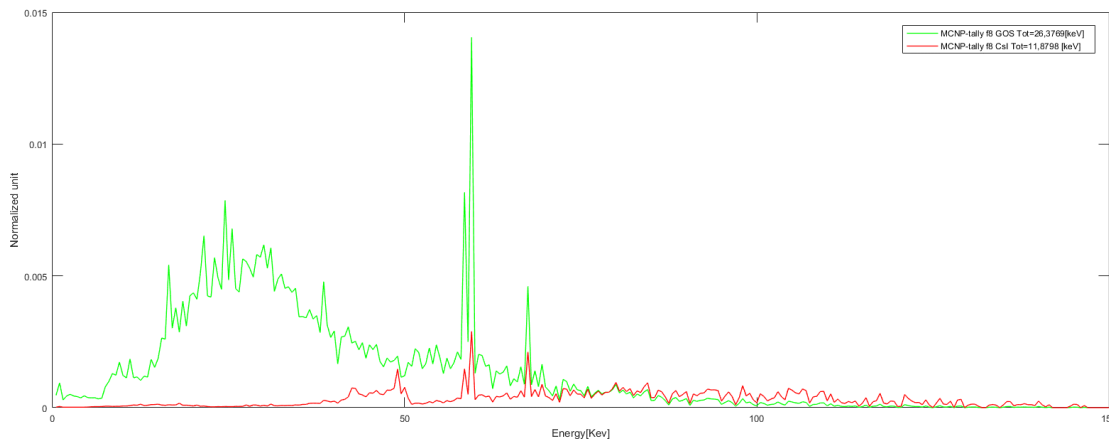


Figure A1.2: Simulated energy spectrum in LES and HES

In Table A1.2 we can find a summary of all the outcome. In this table it is also reported the percentage of the energy deposited in each scintillator.

Table A1.2 Outcomes of the simulation

	<b>Deposited energy</b> <b>[keV]</b>	<b>Percentage</b>
LES	26,3769	68,95%
HES	11,8798	31,05%
Total	38,2567	100%

The photon fluence at the HES interface is strongly reduced by the Cu filter which allows passing only the energetic photons. Meanwhile the deposited energy is further lowered.

To entirely evaluate the system, we also focus on the goodness of the matching among GOS scintillator and PIN. We follow the same procedure used for GAGG(Ce)-CsI(Tl) comparison. The GOS emission spectrum is quite complex, as show in Figure A1.3. Again, we start our analysis extracting data from a literature spectrum using GrabIt tool and then we multiply it, element by element, to the QE

following the same procedure described in 4.2.2. All the spectrums are collected in the Figure A1.3 while the obtained matching factors are reported in Table A1.3.

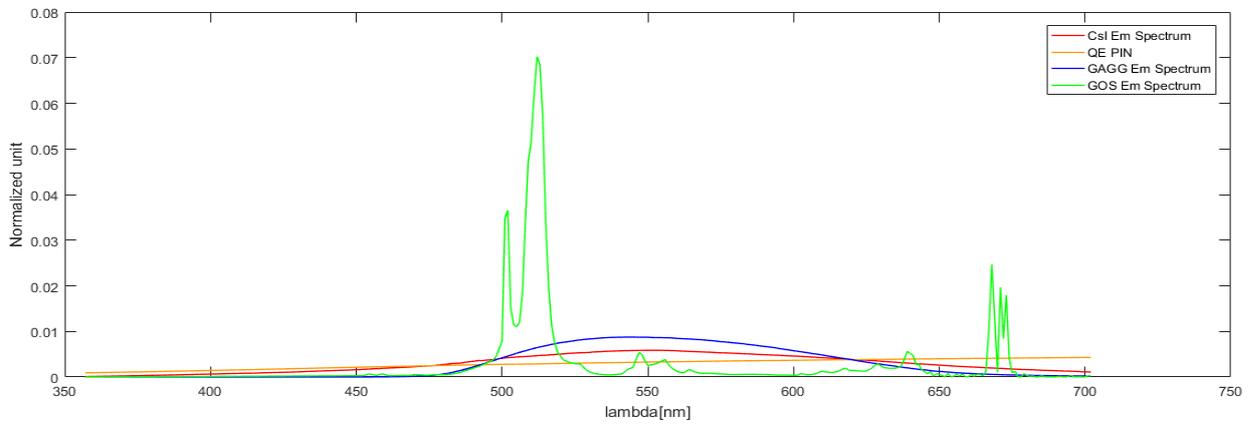


Figure A1.3: Emission spectrum of the analyzed scintillator and PIN QE.

The GOS scintillator has a worse matching factor compared to the CsI(Tl). This is probably due to the peaked emission spectrum around 510nm.

Table A1.3 Matching factor results

	<b>Matching factor</b>
GOS	0,0031071
CsI(Tl)	0,0032421



## 2 Appendix

### *Energy deposition in different scintillators thickness*

As a further development of our work, we can focus on the thickness of scintillators. In fact, basing on the MCNP code developed 4.1.4 it is possible to estimate the energy deposition dependencies from the thickness of each one. Thus, we modify the code to simulate thicknesses from 0.5mm to 3mm separated by 5mm intervals. The scintillators analyzed in this section are again the GAGG(Ce) and the CsI(Tl) and the photon source is the one simulated and validated in our thesis work corresponding to the Gilardoni AION monoblock.

The results are plotted using MATLAB and they are shown in Figure A2.1 and in Figure A2.2. From that we have again the evidence that the CsI(Tl) scintillator is more capable to stop low energy photon than the GAGG(Ce). The trend of energy deposition for CsI(Tl) rapidly increases around 30-40keV. The reason can be sought in the presence of the K-edges of the Iodine and Cesium in this energy range (Figure 4.18).

It is also possible to plot the total deposited energy inside the scintillators against the thicknesses of each one. The result is reported in Figure A2.3 and the trend seems to be an exponential one. The scintillators increase a lot their efficacy to stop photons from 0.5mm to 2mm whereas for an increasing thickness above 2mm the gain in the deposited energy is instead quite low. Above 3mm the deposited energy does not appear to increase even further. Over a certain threshold thickness

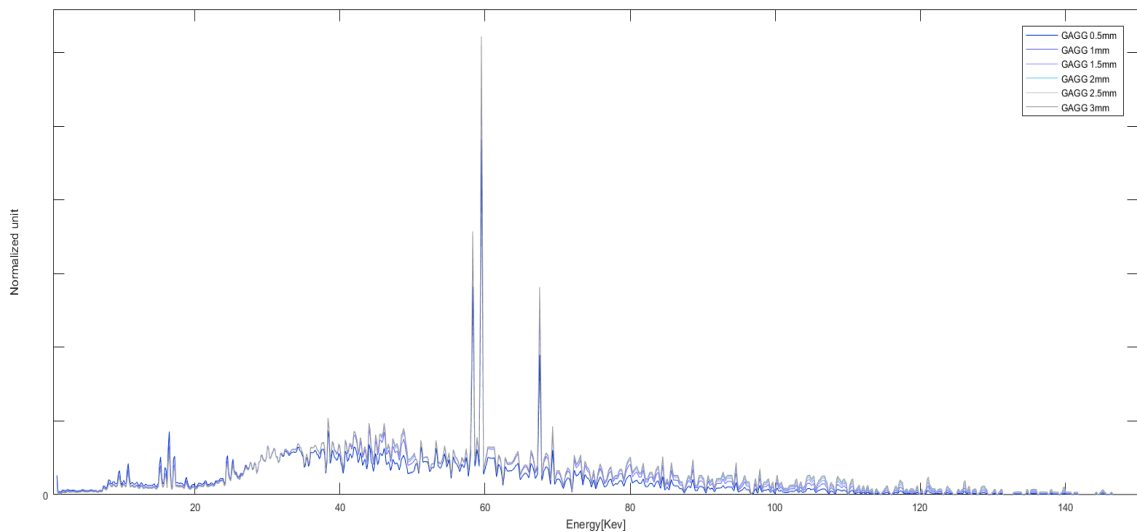


Figure A2.1: Simulated energy deposition spectrum for different thickness of GAGG(Ce) scintillator

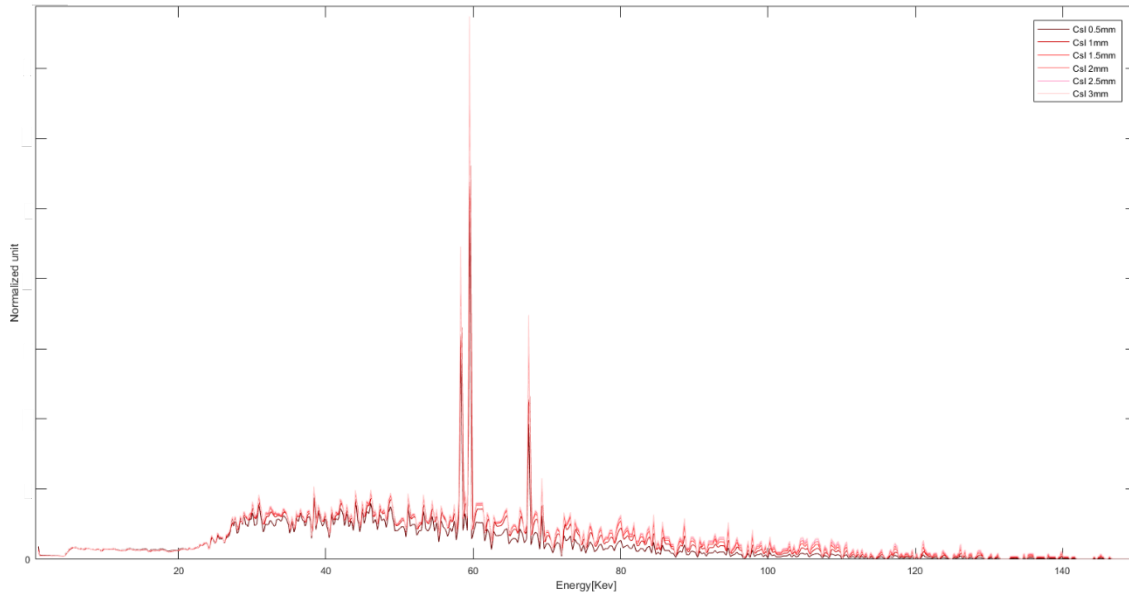


Figure A2.2: Simulated energy deposition spectrum for different thickness of CsI(Tl) scintillator

seems to be enough to stop all the photons belonging to the AION monoblock spectrum with a high probability.

Furthermore, another result should be inferred. There is a thickness where the scintillator CsI(Tl) is more effective than the GAGG(Ce). The value of this thickness looks like to be around 0.85mm. For thin scintillators, the interaction probability for high energy photons have diminished even further in comparison to the ones of low energy photons. The K-edge of CsI(Tl) has again a key role contributing to the enhance the efficacy of CsI(Tl) in respect of GAGG(Ce).

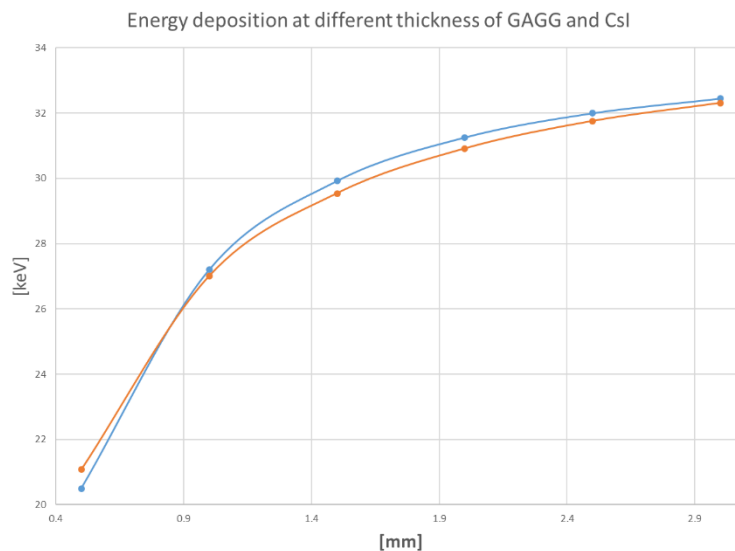


Figure A2.3: Deposited energy plotted against different value of thickness

Finally, we can fit the curve with an exponential function using MATLAB

fitting tool. The chosen fit-equation is the following:

$$F(x) = a - be^{-cx} \quad (A2.1)$$

where  $a$ ,  $b$ , and  $c$  are the characteristic parameter, while  $x$  is the thickness of the scintillator. The outcomes for the GAGG(Ce) and CsI(Tl) are reported in the following Figure A2.4.

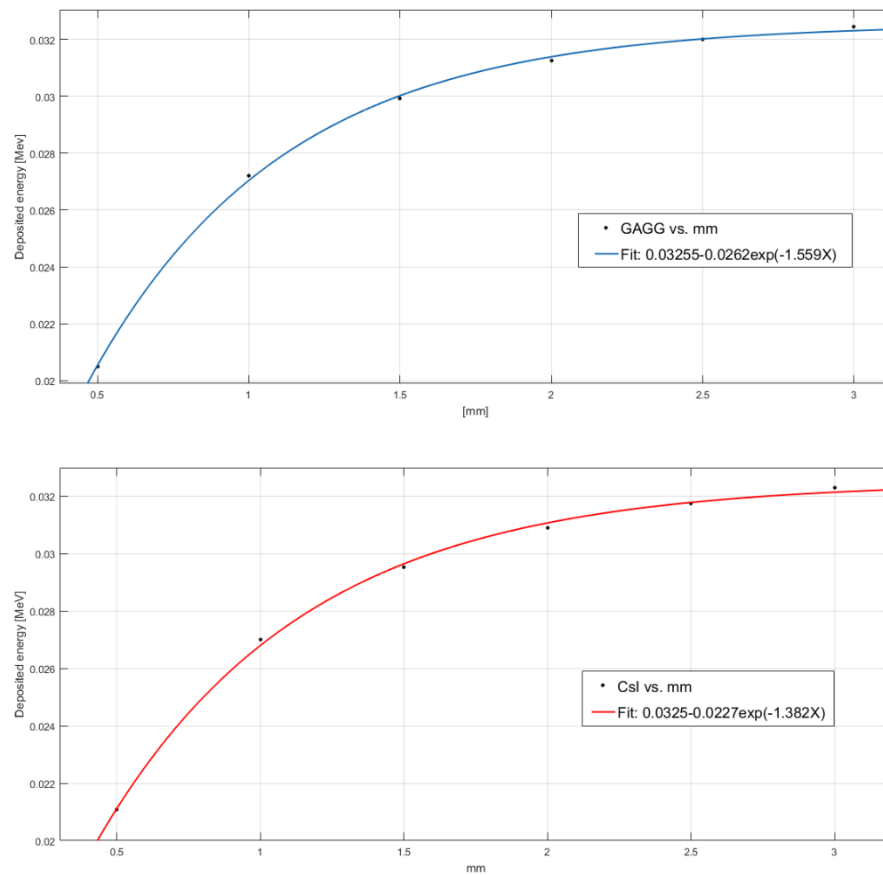


Figure A2.4: MATLAB fits



# Bibliography

- [1] K. Wells, D. A. Bradley. (2012), "*A review of X-ray explosives detection techniques for checked baggage*", Applied Radiation and Isotopes, 8, P.1729-1746
- [2] H. Vogel, D. Haller. (2007), "*Luggage and shipped goods*", Ireland, European Journal of Radiology, 2, P.242-253
- [3] Knoll. (2010), "*Radiation detection and measurement* "
- [4] Gilardoni x-ray Spa website, <https://www.gilardoni.it/>
- [5] Arturo Gilardoni. (1973), "*Raggi x in medicina*"
- [6] Takayuki YANAGIDA. (2018), "*Inorganic scintillating materials and scintillation detectors*", Japan, Proceedings of the Japan Academy, Series B, 2, P.75-97
- [7] Emilie Roncali, Mohammad Amin Mosleh-Shirazi, Aldo Badano. (2017), "*Modelling the transport of optical photons in scintillation detectors for diagnostic and radiotherapy imaging*", England, Physics in medicine and biology, 20, P.R207-R235
- [8] Syed Naeem Ahmed. (2014), "*Physics and Engineering of Radiation Detection*", San Diego, CA, USA
- [9] Perry Sprawls. "*The physical principles of medical imaging*"
- [10] C. Greskovich, S. Duclos. (1997), "*CERAMIC SCINTILLATORS*", Palo Alto, CA 94303-0139, Annual Review of Materials Science, 1, P.69-88
- [11] Jin Hyoung Bai, Joo Ho Whang. (2011), "*The Optimization of CsI(Tl)-PIN Photodiode for High-Energy Gamma-Ray Detection*", Progress in Nuclear Science and Technology, P.308-311
- [12] Thorsten R. C. Johnson. (2012), "*Dual-Energy CT: General Principles*", United States, AJR. American journal of roentgenology, 5 Suppl, P.S3-S8
- [13] Efrat Shefer, Ami Altman, Rolf Behling, et al. (2013), "*State of the Art of CT Detectors and Sources: A Literature Review*", New York, Curr Radiol Rep, 1, P.76-91

- [14] Ibrahim el-SH (2014), "*Characterization of ureteral stents by dual-energy computed tomography: Clinical implications*", World journal of radiology, 8, P.625-628
- [15] Joel Greenberg. (2018), "*X-Ray Diffraction Imaging*"
- [16] Takumi Hamaguchi, Ikuo Kanno. (2019), "*Effective atomic number estimation by energy-resolved X-ray computed tomography with a current-mode detector system*", Japanese Journal of Applied Physics, 7, P.71001
- [17] Martin Nikl, Akira Yoshikawa. (2015), "*Recent R&D Trends in Inorganic Single-Crystal Scintillator Materials for Radiation Detection*", Advanced Optical Materials, 4, P.463-481
- [18] Jarek Glodo, Yimin Wang, Ryan Shawgo, et al. (2017), "*New Developments in Scintillators for Security Applications*", Physics Procedia, P.285-290
- [19] Paul Lecoq, Alexander Gektin, Mikhail Korzhik. (2017), "*Inorganic Scintillators for Detector Systems*", Cham
- [20] Birks, D.W. Fry Fry, L. Costrell Costrell, et al. (1964), "*The Theory and Practice of Scintillation Counting*", GB
- [21] Marvin J. Weber. (2002), "*Inorganic scintillators: today and tomorrow*", Journal of Luminescence, 1, P.35-45
- [22] Peter Capper. (2005), "*Bulk Crystal Growth of Electronic, Optical and Optoelectronic Materials*", GB
- [23] V. V. Nagarkar, V. Gaysinskiy, E. E. Ovechkina, et al. (2007), "*Suppression of Afterglow in CsI(Tl) by Codoping With  $\text{La}^{3+}$ : Fabrication of Microcolumnar Films for High-Resolution High-Speed Imaging*", TNS, 4, P.1378-1382
- [24] G. Gratta, H. Newman, R. Y. Zhu. (1994), "*Crystal Calorimeters in Particle Physics*", Annual Review of Nuclear and Particle Science, 1, P.453-500
- [25] Stuart R. Miller, Charles Brecher, Matthew S. J. Marshall, Megan Wart, Vivek V. Nagarkar. (2019), "*How Excitation Conditions Alter the Afterglow Characteristics of CsI:Tl, Sm Microcolumnar Films*", TNS, 10, P.2229-2232
- [26] Paul Lecoq. (2016), "*Development of new scintillators for medical applications*"
- [27] A. Nassalski, M. Kapusta, T. Batsch, et al. (2007), "*Comparative Study of Scintillators for PET/CT Detectors*", New York, TNS, 1, P.3-10
- [28] Martin Nikl. (2006), "*Scintillation detectors for x-rays*", Measurement Science and Technology, 4, P.R37-R54

- 
- [29] S. L. Bugby, L. K. Jambi, J. E. Lees. (2016), "*A comparison of CsI:Tl and GOS in a scintillator-CCD detector for nuclear medicine imaging*", Journal of Instrumentation, 9, P.P09009
- [30] T. Jing, C. A. Goodman, J. Drewery, et al. (1996), "*Detection of charged particles and X-rays by scintillator layers coupled to amorphous silicon photodiode arrays*", Nuclear Inst. and Methods in Physics Research, A, 3, P.757-764
- [31] Shreetu Shrestha. (2018), "*Methylammonium Lead Iodide Perovskite for Direct X-ray Detection* "
- [32] Giuliano Mariani, Duccio Volterrani, Paola Anna Erba. (2010), "*Fondamenti di medicina nucleare*", IT
- [33] CERN, compact muon solenoid, <http://cms.web.cern.ch/>
- [34] C. M. Pepin, P. Berard, A. -L Perrot, et al. (2004), "*Properties of LYSO and recent LSO scintillators for phoswich PET detectors*", New York, TNS, 3, P.789-795
- [35] W. W. Moses, S. E. Derenzo, A. Fyodorov, et al. (1995), "*LuAlO<sub>3</sub>:Ce - a high density, high speed scintillator for gamma detection*", IEEE Transactions on Nuclear Science, 4, P.275
- [36] Kei Kamada, Takanori Endo, Kousuke Tsutumi, et al. (2011), "*Composition Engineering in Cerium-Doped (Lu,Gd)<sub>3</sub>(Ga,Al)<sub>5</sub>O<sub>12</sub> Single-Crystal Scintillators*", Crystal Growth & Design, 10, P.4484-4490
- [37] M. Kitaura, A. Sato, K. Kamada, A. Ohnishi, M. Sasaki. (2014), "*Phosphorescence of Ce-doped Gd<sub>3</sub>Al<sub>2</sub>Ga<sub>3</sub>O<sub>12</sub> crystals studied using luminescence spectroscopy*", Journal of Applied Physics, 8
- [38] Nerine Cherepy, Benjamin Sturm, Owen Drury, et al. (Jan 1, 2009), "*SrI<sub>2</sub> scintillator for gamma ray spectroscopy*", United States
- [39] Advatech-uk website, <https://www.advatech-uk.co.uk/>
- [40] Kinheng website, <http://www.kinheng-crystal.com/>
- [41] Berkeley Nucleonics Corporation (BNC) website, <https://www.berkeleynucleonics.com/>
- [42] Saint Gobain website, <https://www.crystals.saint-gobain.com/products/crystal-scintillation>
- [43] Matthew Lowdon, Peter G. Martin, M. W. J. Hubbard, et al. (2019), "*Evaluation of Scintillator Detection Materials for Application within*

- Airborne Environmental Radiation Monitoring*", Switzerland, Sensors (Basel, Switzerland), 18, P.3828
- [44] Takayuki Yanagida, Kei Kamada, Yutaka Fujimoto, Hideki Yagi, Takagimi Yanagitani. (2013), "*Comparative study of ceramic and single crystal Ce:GAGG scintillator*", Optical Materials, 12, P.2480-2485
- [45] Pawel Sibczynski, Andrzej Broslawski, Aneta Gojska, et al. (2017), "*Characterization of some modern scintillators recommended for use on large fusion facilities in  $\gamma$ -ray spectroscopy and tomographic measurements of  $\gamma$ -emission profiles*", Nukleonika, 3, P.223-228
- [46] MCNP website, <https://mcnp.lanl.gov/>
- [47] W. L. Thompson. (1979), "*MCNP, a general Monte Carlo code for neutron and photon transport: a summary*", United States
- [48] Madison T. Andrews, Cameron R. Bates, Maria I. Pinilla, Edward A. McKigney, Avneet Sood. (Oct 2017), "*Development of Validated Detector Models with MCNP® and DRiFT*", NSSMIC, P.1-3
- [49] J. K. Shultis. "*An mcnp primer - Kansas State University*"
- [50] T. E. Valentine. (2001), "*MCNP-DSP USERS MANUAL*", United States
- [51] D. Marinescu Ioan, Dimitrov Boris, Rowe W. Brian, Ohmori Hitoshi. (2013), "*Process Fluids for Abrasive Machining*", P.2-3
- [52] "*Amptek X-123 CdTe spectrometer brochure*"
- [53] "*User Guide and Operating Instructions - Amptek CdTe spectrometer*"
- [54] Alessandro Giampieri. (2015), "*Caratterizzazione della funzione risposta di un detector CdTe mediante simulazione Monte Carlo*"
- [55] MATLAB website, <https://it.mathworks.com/>